University of West Bohemia
Faculty of Applied Sciences

DEPOSITION OF FUNCTIONAL THIN-FILM MATERIALS BY ADVANCED SPUTTERING TECHNIQUES

Ing. Šárka Batková

A thesis submitted for the degree of Doctor of Philosophy

in the field of Plasma Physics and Physics of Thin Films

Supervisor: doc. Ing. Jiří Čapek, Ph.D.

Department of Physics

Plzeň 2021

Západočeská univerzita v Plzni
Fakulta aplikovaných věd

DEPOZICE FUNKČNÍCH TENKOVRSTVÝCH MATERIÁLŮ POMOCÍ POKROČILÝCH NAPRAŠOVACÍCH TECHNIK

Ing. Šárka Batková

Disertační práce k získání akademického titulu doktor
v oboru Fyzika plazmatu a tenkých vrstev

Školitel: doc. Ing. Jiří Čapek, Ph.D.
Katedra fyziky

Plzeň 2021

Preface

I declare that all results presented in this Ph.D. thesis are original and were obtained during my doctoral study at the Department of Physics of the Faculty of Applied Sciences at the University of West Bohemia. I wrote the thesis by myself using the duly cited literature. The thesis is submitted in a form of four scientific papers published in international journals.

Plzeň, 12. 11. 2021 …………………………

Ing. Šárka Batková

Acknowledgements

I would like to express deep gratitude to my supervisor, doc. Ing. Jiří Čapek, Ph.D., who guided me through my doctoral study, was always patient, motivational and provided me with excellent advice. I would also like to thank prof. Ing. Petr Zeman, Ph.D. for valuable discussion and assistance. My gratitude goes to Ing. Michaela Červená, Ph.D. for friendship, support and for endless annealing of our samples. Last but not least, I want to thank all staff and Ph.D. students for helping me when needed and for making me feel comfortable at the Department of Physics.

Abstract

Materials from the Ta–O–N system offer very promising properties in terms of hydrogen production via light-induced water splitting. This Ph.D. thesis deals with the preparation and systematic investigation of Ta–O–N films with very finely-tuned elemental composition, as well as an investigation of advanced magnetron-based deposition techniques capable of enhancement of the materials' performance in future research.

Section I is devoted to a general introduction and motivation for this work. In Section II, aims of this thesis are defined. Section III is the most extensive and important section and is devoted to results. This section is divided into four parts (Parts A – D) in the form of papers published in international journals.

A High power impulse magnetron sputtering of a Ta target in various Ar+O_2+N_2 gas mixtures was utilized to prepare amorphous Ta–O–N films with a finely controlled elemental composition in a wide range. We investigate the effect of film annealing at 900°C in vacuum on structure and properties of the films. We show that the finely tuned elemental composition in combination with the annealing enables the preparation of crystalline Ta–O–N films exhibiting a single TaON phase with a monoclinic lattice structure, refractive index of 2.65 and extinction coefficient of 2.0×10^2 (both at the wavelength of 550 nm), optical band gap width of 2.45 eV (suitable for visible light absorption up to 505 nm), low electrical resistivity of 0.4 Ω cm (indicating enhanced charge transport in the material as compared to the as-deposited counterpart), and appropriate position of the band gap with respect to the redox potentials for water splitting. These films are therefore promising candidates for application as visible-light-driven photocatalysts for water splitting.

B Further fine-tuning of the deposition atmosphere together with post-deposition annealing was used to prepare N-rich Ta–O–N films with a finely varied elemental composition. We show that this approach allows preparation of a Ta–O–N film with a dominant Ta_2N_2O phase of the bixbyite structure. As far as we know, this phase has been neither experimentally nor theoretically reported yet. The film exhibits semiconducting properties characterized by two electrical (indirect or selection-rule forbidden) band gaps of about 0.2 and 1.0 eV and one optical (direct and selection-rule allowed) band gap of 2.0 eV (suitable for visible-light absorption up to 620 nm). This observation is in good agreement with the carried out *ab initio* calculations and the experimental data obtained by soft and hard X-ray

photoelectron spectroscopy. Furthermore, the optical band gap is appropriately positioned with respect to the redox potentials for water splitting, which makes this material an interesting candidate for this application.

C We investigate the effect of a positive pulse voltage (30 – 400 V) in bipolar HiPIMS on the crystal structure, microstructure and resulting mechanical properties of the growing CrN films, and compare it to the effect of a standard DC bias voltage applied to the substrate holder in unipolar HiPIMS. We find that when the substrate holder is at a floating potential, its charging causes the loss of the plasma-substrate potential difference, necessary for ion acceleration, and no obvious evolution is thus observed with increasing positive pulse voltage. However, when the substrate holder is grounded, the effect of the positive pulse voltage is apparent and different from the effect of the DC bias substrate voltage. That is mainly due to differences in energies delivered into the growing film by bombarding ions. Films prepared using bipolar HiPIMS at a positive pulse voltage of 90 and 120 V exhibit the most interesting properties, namely high hardness (23.5 and 23.1 GPa, respectively) at a relatively low residual compressive stress (1.7 and 1.5 GPa, respectively). The results indicate that as long as the growing film is conductively connected with the ground, bipolar HiPIMS is a suitable method to tailor and improve the film properties.

D Gas-aggregation source (GAS) was used to prepare Cu nanoparticles. By changing the diameter of the exit orifice of the aggregation chamber, we were able to isolate and investigate the effect of the flow rate of the working gas at a constant pressure inside the chamber. We show that the conventional approach of changing pressure by adjusting the flow rate (at a constant orifice diameter) does not significantly influence the nanoparticle size. However, when the pressure is held constant, changing the flow rate has a notable effect. Based on a theoretical study, we suggest that the determining parameter which needs to be considered is the pressure to flow rate ratio. This ratio determines the residence time of the nanoparticles inside the aggregation chamber (and therefore the time available for them to grow) and is constant for a constant orifice diameter. Decreasing the orifice diameter, however, increases the pressure to flow rate ratio, which gives the nanoparticles longer time inside the aggregation chamber and allows them to grow larger. Apart from their size, the orifice diameter also influences the mass flux and its angular distribution.

In Section IV, conclusions of this thesis are given. In Section V, further publications of the candidate are listed.

Resumé česky

Materiály ze systému Ta–O–N nabízejí velice slibné vlastnosti pro produkci vodíku rozkladem vody aktivovaným světlem. Tato disertační práce se zabývá přípravou a systematickým výzkumem vrstev Ta–O–N s velmi jemně laděným prvkovým složením a výzkumem pokročilých magnetronových depozičních technik umožňujících budoucí zlepšení výkonu zkoumaných materiálů.

Sekce I se věnuje obecnému úvodu a motivaci pro tuto práci. V Sekci II jsou definovány cíle práce. Sekce III je nejrozsáhlejší a nejdůležitější a věnuje se výsledkům. Je rozdělena do čtyř částí (Část A – D) ve formě vědeckých článků publikovaných v mezinárodních časopisech.

A Vysokovýkonové pulzní magnetronové naprašování tantalového terče v různých směsích $Ar+O_2+N_2$ bylo použito pro přípravu amorfních vrstev Ta–O–N s velmi jemně laděným prvkovým složením v širokém rozsahu. Zkoumáme vliv žíhání při 900°C ve vakuu na strukturu a vlastnosti připravených vrstev. Ukazujeme, že kombinace jemně laděného složení a žíhání umožňuje přípravu krystalického materiálu Ta–O–N, který vykazuje pouze fázi TaON s monoklinickou strukturou, refraktivním indexem 2,65, s extinkčním koeficientem $2{,}0 \times 10^2$ (obě hodnoty pro vlnovou délku 550 nm), optickým zakázaným pásem s šířkou 2,45 eV (vhodným pro absorpci viditelného světla až 505 nm), nízkou elektrickou rezistivitou 0,4 Ω cm (značící zlepšený transport nosičů náboje materiálem v porovnání s nevyžíhaným vzorkem) a vhodnou pozicí zakázaného pásu s přihlédnutím k uplatnění v rozkladu vody. Tento materiál je tak velmi slibným kandidátem pro použití v rozkladu vody pomocí světla.

B Ještě jemnější ladění depoziční atmosféry spolu s žíháním připravených vzorků bylo použito k přípravě vrstev Ta–O–N bohatých na dusík s velmi jemně měnícím se prvkovým složením. Ukazujeme, že tento přístup dovoluje přípravu vrstev Ta–O–N s dominantní fází Ta_2N_2O se strukturou bixbyite. Pokud víme, tato fáze zatím nebyla experimentálně ani teoreticky popsána. Tento materiál vykazuje polovodičové vlastnosti definované dvěma elektrickými zakázanými pásy (nepřímým nebo se zakázanými přechody) s šířkou 0,2 a 1,0 eV a jedním optickým zakázaným pásem (přímým a s povolenými přechody) s šířkou 2,0 eV (vhodným pro absorpci viditelného světla až 620 nm). Toto pozorování je v dobré shodě s provedenými výpočty *ab initio* a experimentálními daty z rentgenové fotoelektronové spektroskopie. Optický zakázaný pás je navíc vhodně umístěn s přihlédnutím k uplatnění v

rozkladu vody. Tento materiál je tak zajímavým kandidátem pro použití v rozkladu vody pomocí světla.

C Zkoumáme vliv kladného napěťového pulzu (30 – 400 V) v bipolárním HiPIMS na krystalovou strukturu, mikrostrukturu a výsledné mechanické vlastnosti rostoucích vrstev CrN a porovnáváme ho s vlivem standardního DC předpětí přivedeného na držák substrátů v unipolárním HiPIMS. Zjišťujeme, že pokud je držák substrátů držen na plovoucím potenciálu, jeho nabíjení způsobuje ztrátu potenciálového rozdílu mezi plazmatem a substráty, který je potřebný pro urychlení iontů a žádný výrazný vývoj tak není se zvyšujícím se napětím pozorován. Nicméně pokud je držák substrátů uzemněn, vliv kladného napětí je zřejmý a jiný než vliv DC předpětí. To je způsobeno hlavně rozdílnými energiemi dodanými do vrstvy dopadajícími ionty. Vrstvy připravené pomocí bipolárního HiPIMS při kladném napětí 90 a 120 V vykazují nejzajímavější vlastnosti, obzvláště pak vysokou tvrdost (1,7 a 1,5 GPa). Tyto výsledky naznačují, že pokud jsou rostoucí vrstvy vodivě spojeny se zemí, bipolární HiPIMS je vhodnou metodou k ladění a zlepšování vlastností rostoucí vrstvy.

D Agregační zdroj byl použit pro přípravu měděných nanočástic. Změnou průměru výstupní štěrbiny agregační komory jsme byli schopni oddělit a zkoumat vliv průtoku pracovního plynu při jeho konstantním tlaku uvnitř agregační komory. Ukazujeme, že konvenční přístup, kdy je tlak plynu měněn pomocí jeho průtoku (při konstantním průměru štěrbiny), výrazně neovlivňuje velikost nanočástic. Nicméně pokud je tlak držen konstantní, změna průtoku pak má významný vliv. Na základě teoretické studie navrhujeme, že určujícím parametrem je poměr tlaku ku průtoku. Tento poměr určuje čas pobytu nanočástic v agregační komoře a tím pádem i čas k růstu a je konstantní pro konstantní průměr výstupní štěrbiny. Zmenšením poloměru štěrbiny se ale zvýší poměr tlaku ku průtoku, což poskytne nanočásticím více času v agregační komoře a ty pak můžou narůst do větších velikostí. Kromě jejich velikosti ovlivňuje průměr výstupní štěrbiny i hmotností tok a jeho úhlové rozdělení.

V Sekci IV jsou popsány závěry této práce. V Sekci V je uveden seznam dalších publikací kandidáta.

Contents

I Introduction ... 12
1. Light-induced water splitting ... 12
   1.1.Photoelectrochemical cells ... 13
   1.2.Photoactive material requirements ... 14
2. High-power impulse magnetron sputtering ... 15
   2.1. Bipolar HiPIMS ... 18
3. Nanoparticles ... 18
   3.1. Nanoparticle production ... 18
   3.2. Nanoparticle application ... 21

References ... 23

II Aims of the thesis ... 28

III Results ... 29

A Effect of annealing on structure and properties of Ta–O–N films prepared by high power impulse magnetron sputtering ... 30
1. Introduction ... 31
2. Experimental details ... 32
   2.1. Film preparation ... 32
   2.2. Film characterization ... 32
3. Results and discussion ... 34
   3.1. Elemental composition ... 34
   3.2. Structure of films ... 36
   3.3. Properties of films based on their electronic structure ... 36
   3.4. Promising candidates for water splitting ... 37
4. Summary and conclusions ... 37

Acknowledgements ... 38

References ... 38

B Bixbyite-Ta_2N_2O film prepared by HiPIMS and postdeposition annealing: Structure and properties ... 39
1. Introduction ... 40
2. Experimental and methodology ... 41
   2.1. Film preparation ... 41
   2.2. Film annealing ... 41

2.3. Film characterization and *ab initio* calculations 41
3. Results and discussion 42
3.1. Elemental composition of Ta–O–N films 42
3.2. Crystal structure of Ta–O–N films 42
3.3. Bixbyite-Ta_2N_2O film 43
4. Conclusions 47
Acknowledgements 48
Appendix: Effect of thermally excited electron-hole pairs on the lifetime of the photogenerated ones 48
References 49
C Effect of positive pulse voltage in bipolar reactive HiPIMS on crystal structure, microstructure and mechanical properties of CrN films 50
1. Introduction 51
2. Experimental details 52
3. Results and discussion 52
3.1. Discharge conditions 52
3.2. Elemental composition 53
3.3. Crystal structure and microstructure 53
3.4. Mechanical properties 55
3.5. Applicability of bipolar HiPIMS 56
4. Conclusions 56
CRediT authorship contribution statement 57
Declaration of competing interest 57
Acknowledgements 57
Appendix A. Supplementary data 57
References 57
D Effect of exit-orifice diameter on Cu nanoparticles produced by gas-aggregation source 58
1. Introduction 59
2. Experimental details 60
3. Experimental results 61
3.1. Experimental conditions 61
3.2. Size distribution of nanoparticles 61
3.3. Mass flux of nanoparticles 61

4. Discussion 62
4.1. Size distribution of nanoparticles 62
4.2. Mass flux of nanoparticles 64
4.3. Deviation in angular distribution of the mass flux 64
5. Conclusions 65
CRediT authorship contribution statement 65
Declaration of competing interest 65
Acknowledgements 65
Appendix A 65
A.1. Balance of incoming and passing-through Ar gas flow rate 65
A.2. Diffusion coefficient 65
A.3. Balance of incoming and outgoing Ar gas flow rate 66
References 65
IV Conclusions 68
V Further publications of the candidate 71
1. Papers in impacted international journals 71
2. Oral and poster contributions at international conferences 71

I Introduction

In today's pursuit of environmentally friendly methods of power generation, the focus is on clean and renewable sources of energy. For its availability and abundance, solar energy is among the top candidates. One way of converting the solar energy into a more convenient form, namely chemical energy, is through hydrogen. The produced hydrogen can then be stored, transported, and later used in hydrogen fuel cells to produce electricity.

Thin-film materials play a crucial role in almost all fields of modern technologies. Their continuous development is necessary for technological advancement for example in electronics or optics, as well as energy harvesting and production. The potential of thin-film materials in hydrogen production is substantial and therefore intensively investigated.

In this Ph.D. thesis, thin-film materials from the Ta–O–N system and their suitability for hydrogen production via light-induced water splitting are investigated (Parts A and B). Part C is devoted to an advanced thin-film preparation method, designed to effectively tune the structure of the material and consequently possibly influence the hydrogen-production process. Since the effectivity of this process can also be enhanced by addition of nanoparticles, Part D focuses on the possibilities of nanoparticle production and their size control.

This thesis has been carried out within the framework of the projects FV30177 (2018 – 2021): Research and development of novel pulsed plasma technologies for deposition of advanced thin-film materials, GA ČR 19–13174S (2019 – 2021): Advanced hydrogen-gas sensing nanomaterials with a tailored architecture, and MŠMT LO1506 (2015 – 2020): Sustainability support of the centre NTIS - New Technologies for the Information Society.

1. Light-induced water splitting

Hydrogen fuel represents an alternative to the finite and unsustainable fossil fuels. At the moment, however, the majority of hydrogen is also harvested from fossil fuels [1]. The potential solution lies in splitting of water molecules, which is free of unwanted emissions [2,3]. Furthermore, the only by-product of hydrogen combustion in hydrogen fuel cells is again water, making it a renewable source. One way of utilizing solar energy for this process is electrolysis of water using solar-generated electricity (photovoltaic electrolysis). The components for this process are commercially available and its effectivity reaches relatively high values compared to the photoelectrochemical cells described below [4,5]. However, making things as simple and

compact as possible is a never-ending goal. A photoelectrochemical system provides direct conversion of solar energy into hydrogen in a single photoelectrochemical cell. The concept was first introduced in 1972 by Fujishima and Honda [6].

1.1. Photoelectrochemical cells

A photoelectrochemical cell (see Fig. 1) consists of two conductively connected electrodes in an electrolyte. One of the electrodes is a semiconducting material (in case of an n-type semiconductor, the anode). When this material is irradiated with light with energy larger than its band gap, an electron-hole pair is created via photoexcitation. The photogenerated charge carriers then have to migrate to their respective surfaces, where they then participate in the water splitting redox reactions.

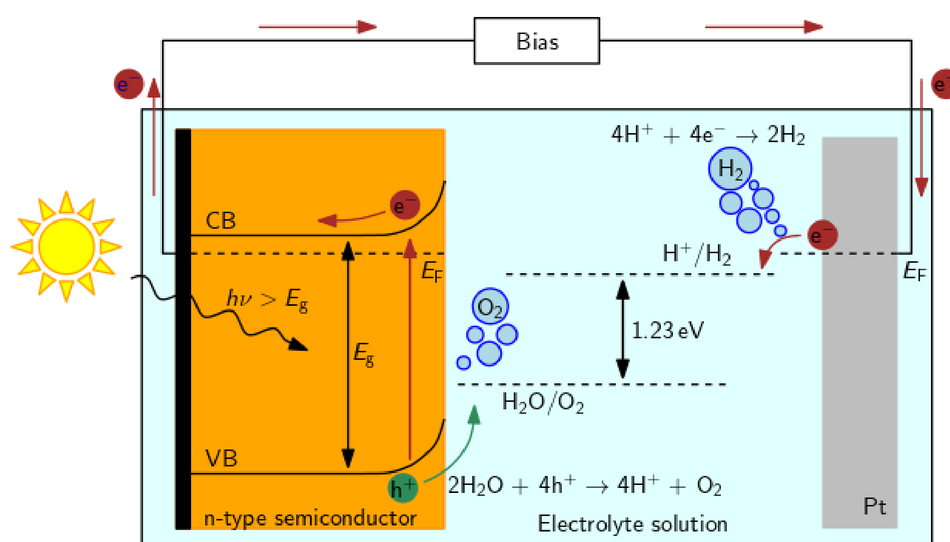

Fig. 1. Diagram of a photoelectrochemical cell with an n-type semiconductor.

In Fig. 1, an n-type semiconductor is depicted in place of the photoactive electrode. A potential difference (naturally formed or additionally applied) between this electrode and the counter electrode (most often platinum) drives the photogenerated electrons to the counter electrode, where they reduce hydrogen ions, and holes to the surface of the semiconductor, where they oxidize water molecules (for the respective chemical reactions see Fig. 1). In case of a p-type semiconductor, the movement of the charge carriers is reversed, which leads to hydrogen production at the semiconductor and oxygen production at the counter electrode.

1.2. Photoactive material requirements

In order to be functional and effective as a material for light-induced water splitting, the semiconductor must satisfy certain conditions. Apart from having to exhibit long-term chemical stability, its optical and structural properties are important as well. As only light with energy larger than the band gap gets absorbed, the band gap width dictates what part of the solar spectrum can be utilized. Since most light coming from the sun is in the visible region, it is desirable to have a band gap that corresponds to visible light absorption. Moreover, the band gap edges have to be properly positioned with respect to the water splitting redox potentials (see Fig. 1). Namely, the bottom of the conduction band has to be more negative than the reduction potential of H^+ to H_2 and similarly, the top of the valence band more positive than the oxidation potential of H_2O to O_2. In other words, both redox potentials need to lie within the band gap when considering the band energy diagram of the material.

Fig. 2 shows examples of the band gaps of various materials and their position with respect to the water splitting redox potentials, including some of the most often investigated ones. The most well-known TiO_2 is relatively easy to prepare and exhibits chemical stability, but the band gap is too wide and the material is active under UV irradiation only. Other promising binary compounds such as WO_3 [7] or Fe_2O_3 [8] have narrower band gap, but since the bottom of the conduction band is not more negative than the reduction potential of H^+, external bias voltage is necessary to drive the reactions. The band gap of Cu_2O is positioned correctly, but strong photocorrosion limits its performance [9]. These and other limitations lead to the investigation of more complex compounds, for example bi-metallic materials, such as $SrTiO_3$ [10] or $CuWO_4$ [11].

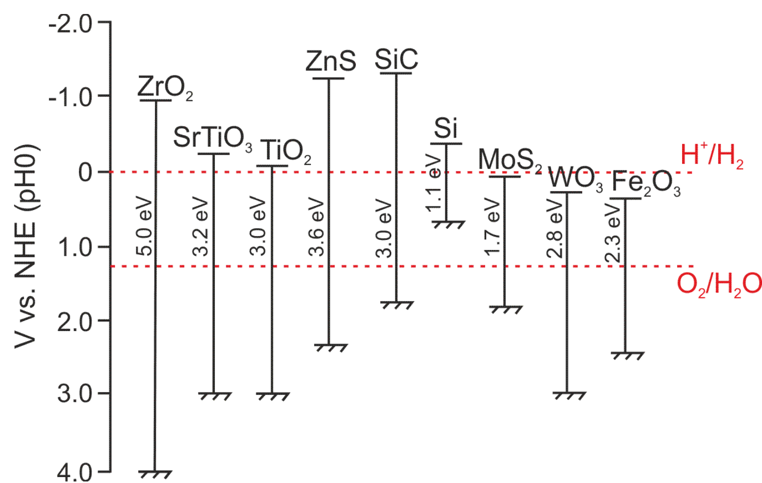

Fig. 2. Position of the band gap of various materials with respect to the water splitting redox potentials [12].

Another group of investigated materials are oxynitrides and nitrides, where the nitrogen 2p orbitals can form a valence band at potentials more negative than a band composed of oxygen 2p orbitals, resulting in a band gap narrower than that of its oxide counterpart [13]. Materials from the Ta–O–N system have been studied as promising candidates for water splitting. Both theoretical [14] and experimental [15–17] works report the value of the band gap width to be 2.5 eV, corresponding to absorption of visible light up to 500 nm. However, the preparation of materials with high water splitting performance is still a challenge, as all of the requirements on properties described above need to be met. In Parts A and B of this thesis, materials from the Ta–O–N system are prepared and systematically investigated and their suitability for photoelectrochemical water splitting is assessed.

After the photogenerated charge carriers get successfully created, they have to migrate through the material either to its surface, or the back electrode. The material must therefore provide sufficient mobility of the charge carriers. The mobility depends greatly on the structural properties of the material. As a preparation technique, magnetron sputtering offers a great control of the process parameters and consequently of the properties of the prepared thin-film material. Lately, more advanced techniques have been under development, to even further increase the degree of control over the structure and properties of the growing film. See the following chapters for more details.

When the charge carriers are created by photoexcitation, one of the biggest problems is a quick recombination that competes with charge separation and migration. It has been shown that a co-catalyst on the surface of the photoactive material can help in trapping and separating the generated charges and in reducing the recombination rate. Nanoparticles provide a very convenient way of adding the co-catalyst to the photoactive surface [18,19]. Moreover, it has been reported that nanoparticles on the surface can increase photoabsorption due to surface plasmon resonance [20].

2. High-power impulse magnetron sputtering

The basic principles of glow discharges have been known for almost 100 years and magnetron sputtering has become one of the most used techniques for thin film preparation. Simply put, a glow discharge is ignited in an inert gas (usually argon) between two electrodes, one of which is made of the desired source material (called the target). The ions of the working gas are accelerated towards the target which is at a negative potential, where they cause atoms and secondary electrons to leave the surface. The electrons play a crucial role in sustaining the

discharge by ionizing neutral argon atoms, while the atoms can travel to a substrate where they grow into a thin film. Because the secondary electron emission yield is usually quite low, it needs to be compensated by trapping the electrons and using them to their maximum potential. That is done by placing magnets behind the target, which results in the electrons being confined by the magnetic field. That is where the most intense ionization occurs and it results in a circular erosion zone on the target. We then talk about magnetron sputtering.

If the sputtered atoms forming the thin-film material are neutral, it is difficult to control them. However, if they are ionized, it is very simple to control their energy by applying an electric potential (usually called a bias voltage) to the substrates and thus effectively tune the structure of the growing film. With regard to this possibility, it is therefore desirable to have as high a degree of ionization of the sputtered atoms as possible. That can be achieved by increasing the target power density, as the ionization becomes more effective. In order to avoid target overheating, this power can be applied in short pulses with a very low duty cycle. When the power density in a pulse exceeds the average power density in a period by about two orders of magnitude, we talk about high-power impulse magnetron sputtering (abbreviated to HiPIMS). Though the quantification of the fraction of the ionized metal atoms can be problematic, as shown in Ref. [21], the reported ionization degree of the sputtered species in HiPIMS is usually around 50 – 70% [22–24] as compared to about 0.1% or even less in standard low-power DC magnetron sputtering [25].

With such high ionization degrees, the application of a bias voltage onto the substrates results in a significant ion bombardment of the film during its growth. The exact effect of the bombardment depends on the energy and the flux of the incoming ions. In a structure zone diagram (SZD), a correlation between the structure of the film and the growth conditions is depicted and described. The first SZD by Movchan and Demchishin included only the effect of increasing homologous temperature [26], later works then developed and modified the SZDs as the deposition techniques moved forward [27–32].

The terminology concerning the individual zones is unfortunately not always used consistently, but Zone 1 is generally described as porous and full of voids, resulting from almost non-existent surface diffusion. As the mobility of the adatoms increases and thus surface diffusion is enhanced in Zone T (a transition zone), competitive growth occurs, where grains of different crystallographic orientations start growing, but only the fastest growing ones prevail. This is governed by kinetic processes and results in V-shaped grains. In Zone 2, bulk diffusion sets in, resulting in grain boundary migration and large columnar grains. The material growth is

governed by thermodynamics. Some authors [26,27,28,32] then add an additional Zone 3, where recrystallization and lateral growth occur, which can result in even larger grains. Mahieu et al. [31] extended Zone 1 by a case where the temperature is low, but ion bombardment causes densification. Anders [32] then proposed a structure zone diagram that specifically includes the effect of ion bombardment with high ion fluxes, which are supplied in HiPIMS. To the temperature axis he added the potential energy of the arriving particles, the second axis he set to be the kinetic energy of the arriving particles and he added a third axis with the thickness of the film (see Fig. 3).

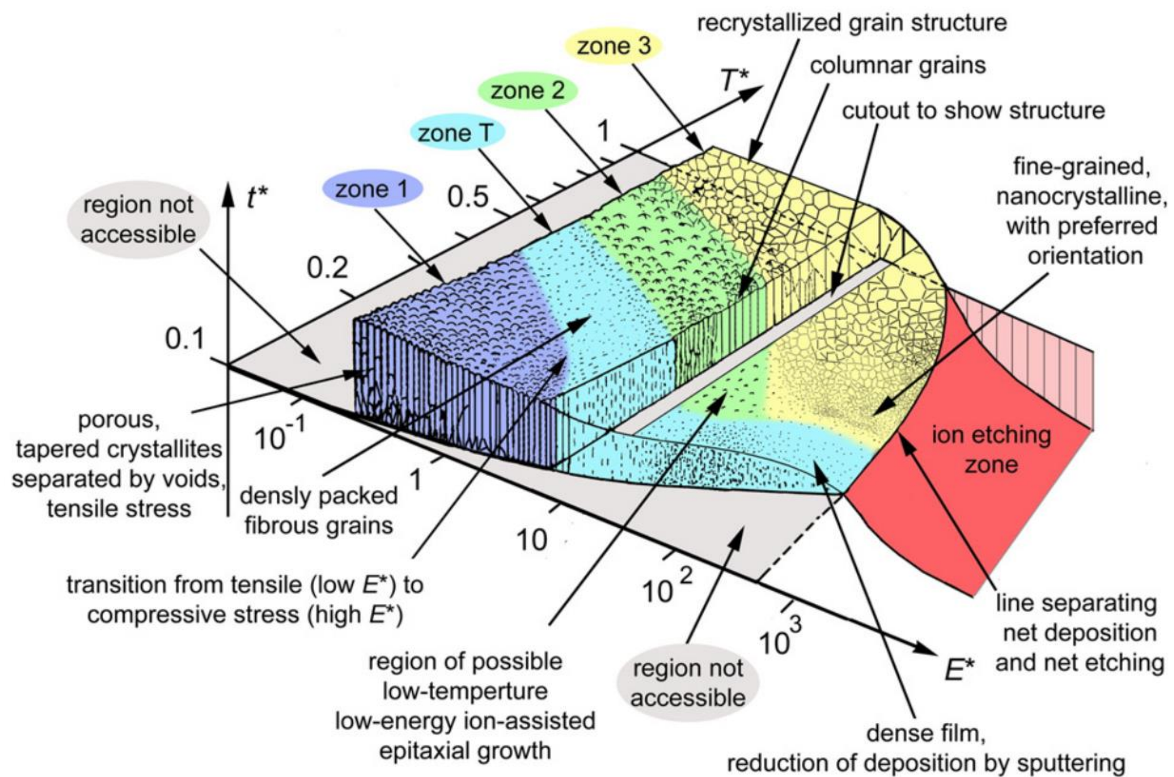

Fig. 3. Structure zone diagram proposed by Anders, including the effect of ion bombardment with high fluxes. T^* is the homologous temperature shifted by potential energy of arriving particles, E^* is the kinetic energy of arriving particles and t^* is film thickness [32].

The main effects of ion bombardment on the structure of the growing film can be summarized as: (1) densification of the growing film by knock-on effects, (2) increase in the degree of the adatoms' mobility, somewhat similar to increased deposition temperature, as well as (3) defect generation and resputtering if the ion energies are too high.

2.1. Bipolar HiPIMS

Applying bias voltage to the substrates results in a potential difference between the substrates and the plasma of the glow discharge. Another possibility of creating this difference is to increase the plasma potential, sometimes called “plasma biasing”. It is known from previous studies [33–35] that the plasma potential always stays within several volts of the potential of the most positive electrode. That is due to the electrons from the plasma being attracted to the electrode and leaving behind a positive cloud of ions. If the main negative voltage pulse on the target of the HiPIMS discharge is therefore followed by a positive voltage pulse, the potential of the afterglow plasma lifts up to values very similar to the potential on the target. The potential difference necessary to accelerate the ions towards the substrate is thus created (assuming the substrates are grounded).

Such an advanced deposition technique is expected to have a great potential in controlling and tuning of the structure of the growing film during its preparation, possibly eliminating the need for any thermal post-treatment. This might be particularly important for example in case of materials where the mobility of charge carriers plays a crucial role, e.g. photoactive materials described in Section 1 of the Introduction and investigated in Parts A and B of this Ph.D. thesis. Part C of this thesis therefore deals with the investigation of bipolar HiPIMS, its effects on structure and properties of the growing material and comparison of bipolar HiPIMS and standard unipolar HiPIMS with bias voltage applied to the substrates.

3. Nanoparticles

Nanoparticles, sometimes referred to as nanoclusters or clusters, are aggregates of atoms of sizes in the nanoscale. Their size gives them unique properties and applications, discussed in more detail below.

3.1. Nanoparticle production

There are numerous ways of nanoparticle production, based on different approaches. These approaches can be divided into two main categories: (i) the nanoparticles are produced from a larger piece that is broken down into smaller units; and (ii) the nanoparticles are synthesized from smaller building blocks. The first approach includes milling/grinding [36] or laser fragmentation [37] and is only rarely used, as it is destructive and offers only a limited control of the nanoparticle size and structure. The second approach can be further divided into various

chemical "wet" techniques, where the nanoparticles are built up from small molecules (for example the sol-gel process [38]) and physical "dry" techniques, i.e. methods based on condensation of single atoms from a gas phase. When this vapor aggregates in a high-pressure inert gas atmosphere, we talk of gas-aggregation sources (often abbreviated to GAS).

To even further categorize, the gas phase can be produced by different physical deposition techniques, including thermal evaporation, laser ablation, ion or electron beam sputtering, arc discharge or hollow cathode. In recent years, however, magnetron sputtering has been used more and more often [39–42], as it offers numerous advantages. These sources are called magnetron-based or sputtering gas-aggregation sources and they offer high versatility thanks to the possibility of using multiple sputtering targets of virtually any solid and/or of adding a reactive gas. Because the process takes place in vacuum and the targets have a high degree of purity, these sources provide a "clean" procedure and a very good control of the elemental composition. Apart from the elemental composition, they also provide good control of structure (for example core-shell or homogenous) and size (either through control of the growth process or through mass selection). Moreover, the nanoparticle formation takes place in a separate aggregation vacuum chamber, which allows for easy integration into more complex deposition systems. One such magnetron-based gas-aggregation source was used in this Ph.D. thesis.

In order for the nanoparticles to start growing, the diffusion of the vapor atoms needs to be limited, or in other words, the vapor needs to be cooled down. Usually, two techniques are used simultaneously. A very high pressure of an inert working gas (most often argon) inside the designated aggregation chamber insures the cooling down of the vapor atoms through frequent collisions. Moreover, the chamber walls are cooled either by water or liquid nitrogen, to further lower the temperature of the vapor.

The formation of nanoparticles in gas-aggregation sources is a two-step process. For the nanoparticles to start growing, there needs to be a nucleus in the form of a dimer: a two-atom seed. These dimers are created by a three-body collision, where the third atom needs to be present for reasons of energy and momentum conservation. It is usually assumed that the major process contributing to nucleation is [43–46]:

$$M + M + Ar \rightarrow M_2 + Ar. \tag{1}$$

In magnetron discharges there is a certain degree of ionization of both the growth material and the argon gas, which is expected to influence the nucleation rate. In Ref. [47] it is even argued

that apart from the formation of a metallic dimer (neutral or charged), another important scenario is the formation of an argon dimer:

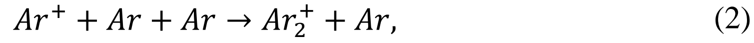

$$Ar^{+} + Ar + Ar \rightarrow Ar_2^{+} + Ar, \quad (2)$$

as the density of argon atoms is much higher than that of the sputtered metal atoms and makes this process much faster. Fig. 4 shows a mass spectra of small clusters using a cobalt target. It can be seen that the argon dimers are detected, as well as the metallic cobalt dimers. However, both Eq. (1) and Eq. (2) are assumed to happen in an ultra-high vacuum system with oxygen-free atmosphere. It should be kept in mind that any amount of residual or purposefully introduced oxygen can significantly change the nucleation kinetics, as the binding energy of a metal and an oxygen atom is sometimes much larger than that of two metal atoms [48,49].

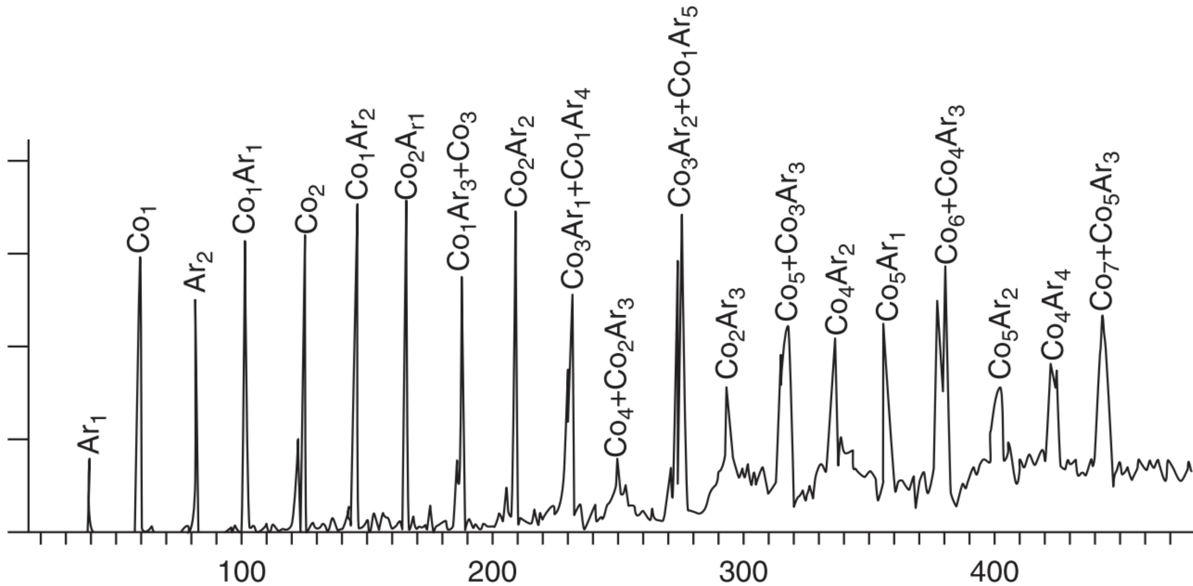

Fig. 4. Mass spectra of small clusters using a cobalt target. One can see argon as well as metallic dimers [47].

Whichever way they get created, the dimers then start growing into nanoparticles. They can grow through different processes. However, quite often (including our work), only one process contributing to growth is assumed and that is growth by single atom attachment. The energy released from the attachment heats up the small cluster and the probability of the atom evaporating again is quite high. In order for the cluster to grow into a thermodynamically stable nanoparticle, it therefore needs to cool down through collisions with the working gas between individual atom attachments [47]. The formed nanoparticles then leave the source together with the working gas through an exit orifice.

The final size distribution and number of nanoparticles depends on a number of variables, such as the density of the available vapor, the dwell time of the nanoparticles in the aggregation chamber or the temperature and composition of the working gas. These in turn depend on the process parameters of the nanoparticle source, such as diameter of the exit orifice, aggregation length or discharge power density. Part D of this Ph.D. thesis is focused on the influence of the exit orifice diameter on the size and mass flux of Cu nanoparticles produced by a gas-aggregation source.

3.2. Nanoparticle application

Thanks to their size resulting in unique physical and chemical properties, nanoparticles have found their application in various fields. In medicine, they are used for site-specific drug delivery [50] and have a great potential in cancer treatment [51]. In electronics, the printing of inks containing metal nanoparticles has been found to be a powerful tool for direct patterning of electrically conductive interconnection in electronic devices [52]. Nanocomposites created by embedding metal nanoparticles in a polymer matrix offer unique functional properties, such as tunable refraction index or antibacterialism [53].

In our laboratories, CuO nanoparticles were prepared in a gas-aggregation source and their potential in hydrogen gas sensing has been investigated [54]. The working principle of a conductometric gas sensor lies in the change of the sensor's conductivity as the detected gas reacts with its surface. In more detail, oxygen is presumed to be preadsorbed on the surface, creating a space charge region. As the detected gas (in our case hydrogen) comes into contact with the surface, it reacts with the preadsorbed oxygen and as a result, electrons are returned to the material, decreasing its resistivity. Very often, a noble metal is present to help dissociate the hydrogen molecules before reacting. In our work, CuO nanoparticles were deposited onto the surface of a WO_3 thin film and the sensorial response was investigated for different amounts of nanoparticles. It was found that the best sensorial response was measured for a sample with one to two monolayers of nanoparticles (see Fig. 5). The CuO nanoparticles form a *p-n* junction with the WO_3 film, which creates a larger depletion zone than that on pure WO_3 and the change in resistivity when hydrogen is present is then larger. A very good sensorial response was thus achieved without the need of noble metals.

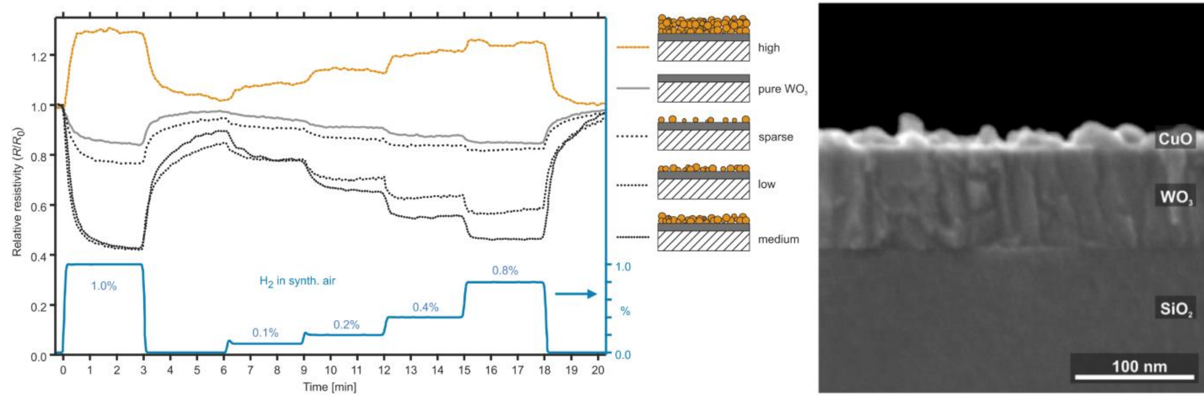

Fig. 5. Sensorial response of a hydrogen gas sensor made of a WO_3 thin film and different amounts of CuO nanoparticles [54].

Another application that is planned in our laboratories is to use nanoparticles in combination with the Ta–O–N films investigated in Parts A and B to enhance the water splitting process (as described in Section 1 of the Introduction).

It is well known that the properties of nanoparticles are size dependent [55,56]; size control is therefore very important in nanoparticle preparation and application. In Part D of this thesis, we investigate the possibility to control their size through process parameters in a magnetron-based gas aggregation source.

References

[1] K. Liu, C. Song, V. Subramani, ed., Hydrogen and Syngas Production and Purification Technologies, Wiley-VCH, 2009. https://doi.org/10.1002/9780470561256.

[2] X. Chen, S. Shen, L. Guo, S.S. Mao, Semiconductor-based photocatalytic hydrogen generation, Chem. Rev. 110 (2010) 6503–6570. https://doi.org/10.1021/cr1001645.

[3] M.Z. Iqbal, S. Siddique, Recent progress in efficiency of hydrogen evolution process based photoelectrochemical cell, Int. J. Hydrogen Energy. 43 (2018) 21502–21523. https://doi.org/10.1016/J.IJHYDENE.2018.09.157.

[4] J. Jia, L.C. Seitz, J.D. Benck, Y. Huo, Y. Chen, J.W.D. Ng, T. Bilir, J.S. Harris, T.F. Jaramillo, Solar water splitting by photovoltaic-electrolysis with a solar-to-hydrogen efficiency over 30%, Nat. Commun. 7 (2016) 1–6. https://doi.org/10.1038/ncomms13237.

[5] A. Grimm, W.A. de Jong, G.J. Kramer, Renewable hydrogen production: A techno-economic comparison of photoelectrochemical cells and photovoltaic-electrolysis, Int. J. Hydrogen Energy. 45 (2020) 22545–22555. https://doi.org/10.1016/J.IJHYDENE.2020.06.092.

[6] A. Fujishima, K. Honda, Electrochemical Photolysis of Water at a Semiconductor Electrode, Nature. 238 (1972) 37–38. https://doi.org/10.1038/238037a0.

[7] Y. Shabdan, A. Markhabayeva, N. Bakranov, N. Nuraje, Photoactive tungsten-oxide nanomaterials for water-splitting, Nanomaterials. 10 (2020) 1–37. https://doi.org/10.3390/nano10091871.

[8] S. Kment, P. Schmuki, Z. Hubicka, L. Machala, R. Kirchgeorg, N. Liu, Photoanodes with Fully Controllable Texture : The Enhanced Water Splitting Efficiency of Thin Hematite Films Exhibiting Solely (110) Crystal Orientation, ACS Nano 9 (2015) 7113–7123. https://doi.org/10.1021/acsnano.5b01740.

[9] I. V. Bagal, N.R. Chodankar, M.A. Hassan, A. Waseem, M.A. Johar, D.H. Kim, S.W. Ryu, Cu_2O as an emerging photocathode for solar water splitting - A status review, Int. J. Hydrogen Energy. 44 (2019) 21351–21378. https://doi.org/10.1016/J.IJHYDENE.2019.06.184.

[10] S. Patial, V. Hasija, P. Raizada, P. Singh, A.A.P. Khan Singh, A.M. Asiri, Tunable photocatalytic activity of $SrTiO_3$ for water splitting: Strategies and future scenario, J. Environ. Chem. Eng. 8 (2020) 103791. https://doi.org/10.1016/J.JECE.2020.103791.

[11] Y. Gao, T.W. Hamann, Elucidation of $CuWO_4$ Surface States during Photoelectrochemical Water Oxidation, J. Phys. Chem. Lett. 8 (2017) 2700–2704. https://doi.org/10.1021/acs.jpclett.7b00664.

[12] A. Kudo, Y. Miseki, Heterogeneous photocatalyst materials for water splitting, Chem. Soc. Rev. 38 (2009) 253–278. https://doi.org/10.1039/B800489G.

[13] T. Hisatomi, J. Kubota, K. Domen, Recent advances in semiconductors for photocatalytic and photoelectrochemical water splitting, Chem. Soc. Rev. 43 (2014) 7520–7535. https://doi.org/10.1039/c3cs60378d.

[14] A.H. Reshak, Ab initio study of TaON, an active photocatalyst under visible light irradiation, Phys. Chem. Chem. Phys. 16 (2014) 10558–10565. https://doi.org/10.1039/c4cp00285g.

[15] W.J. Chun, A. Ishikawa, H. Fujisawa, T. Takata, J.N. Kondo, M. Hara, M. Kawai, Y. Matsumoto, K. Domen, Conduction and valence band positions of Ta_2O_5, TaON, and Ta_3N_5 by UPS and electrochemical methods, J. Phys. Chem. B. 107 (2003) 1798–1803. https://doi.org/10.1021/jp027593f.

[16] M. Hara, G. Hitoki, T. Takata, J.N. Kondo, H. Kobayashi, K. Domen, TaON and Ta_3N_5 as new visible light driven photocatalysts, Catal. Today 78 (2003) 555–560. https://doi.org/10.1016/S0920-5861(02)00354-1.

[17] J. Rezek, J. Vlček, J. Houška, R. Čerstvý, High-rate reactive high-power impulse magnetron sputtering of Ta-O-N films with tunable composition and properties, Thin Solid Films. 566 (2014) 70–77. https://doi.org/10.1016/j.tsf.2014.07.033.

[18] C. Wang, J. Tang, X. Zhang, L. Qian, H. Yang, WO_3 nanoflakes decorated with CuO clusters for enhanced photoelectrochemical water splitting, Prog. Nat. Sci. Mater. Int. 28 (2018) 200–204. https://doi.org/10.1016/j.pnsc.2018.03.004.

[19] K. Khan, X. Tao, Y. Zhao, B. Zeng, M. Shi, N. Ta, J. Li, X. Jin, R. Li, C. Li, Spatial separation of dual-cocatalysts on one-dimensional semiconductors for photocatalytic hydrogen production, J. Mater. Chem. A. 7 (2019) 15607–15614. https://doi.org/10.1039/c9ta03090e.

[20] A. Tanaka, K. Teramura, S. Hosokawa, H. Kominami, T. Tanaka, Visible light-induced water splitting in an aqueous suspension of a plasmonic Au/TiO_2 photocatalyst with metal co-catalysts, Chem. Sci. 8 (2017) 2574–2580. https://doi.org/10.1039/C6SC05135A.

[21] A. Butler, N. Brenning, M. Raadu, J.T. Gudmundsson, T. Minea, D. Lundin, On three different ways to quantify the degree of ionization in sputtering magnetrons, Plasma Sources Sci. Technol. 27 (2018) 105005. https://doi.org/10.1088/1361-6595/aae05b.

[22] C. Huo, M.A. Raadu, D. Lundin, J.T. Gudmundsson, A. Anders, N. Brenning, Gas rarefaction and the time evolution of long high-power impulse magnetron sputtering pulses, Plasma Sources Sci. Technol. 21 (2012) 045004. https://doi.org/10.1088/0963-0252/21/4/045004.

[23] T. Kubart, M. Čada, D. Lundin, Z. Hubička, Investigation of ionized metal flux fraction in HiPIMS discharges with Ti and Ni targets, Surf. Coatings Technol. 238 (2014) 152–157. https://doi.org/10.1016/j.surfcoat.2013.10.064.

[24] D. Lundin, M. Čada, Z. Hubička, Ionization of sputtered Ti , Al , and C coupled with plasma characterization in HiPIMS, Plasma Sources Sci. Technol. 24 (2015) 035018. https://doi.org/10.1088/0963-0252/24/3/035018.

[25] I. Petrov, A. Myers, J.E. Greene, J.R. Abelson, Mass and energy resolved detection of ions and neutral sputtered species incident at the substrate during reactive magnetron sputtering of Ti in mixed Ar+N_2 mixtures , J. Vac. Sci. Technol. A 12 (1994) 2846–2854. https://doi.org/10.1116/1.578955.

[26] B.A. Movchan, A.V. Demchishin, STRUCTURE AND PROPERTIES OF THICK CONDENSATES OF NICKEL, TITANIUM, TUNGSTEN, ALUMINUM OXIDES, AND ZIRCONIUM DIOXIDE IN VACUUM., Phys. Met. Met. 28 (1969) 653–660.

[27] J.A. Thorton, High Rate Thick Film Growth, Ann. Rev. Mater. Sci. 7 (1977) 239–260. https://doi.org/10.1146/annurev.ms.07.080177.001323.

[28] R. Messier, A.P. Giri, R.A. Roy, Revised structure zone model for thin film physical structure, J. Vac. Sci. Technol. A 2 (1984) 500–503. https://doi.org/10.1116/1.572604.

[29] H.T.G. Hentzell, D.A. Smith, C. Grovernor, The development of grain structure during growth of metallic thin films, Acta Metall. 32 (1984) 773–781. https://doi.org/10.1016/0001-6160(84)90150-0.

[30] P.B. Barna, M. Adamik, Fundamental structure forming phenomena of polycrystalline films and the structure zone models, Thin Solid Films. 317 (1998) 27–33. https://doi.org/10.1016/S0040-6090(97)00503-8.

[31] S. Mahieu, P. Ghekiere, D. Depla, R. De Gryse, Biaxial alignment in sputter deposited thin films, Thin Solid Films. 515 (2006) 1229–1249. https://doi.org/10.1016/j.tsf.2006.06.027.

[32] A. Anders, A structure zone diagram including plasma-based deposition and ion etching, Thin Solid Films. 518 (2010) 4087–4090. https://doi.org/10.1016/j.tsf.2009.10.145.

[33] D. Vender, R.W. Boswell, Numerical Modeling of Low-Pressure RF Plasmas, IEEE Trans. Plasma Sci. 18 (1990) 725–732. https://doi.org/10.1109/27.57527.

[34] S.K. Karkari, A. Vetushka, J.W. Bradley, Measurement of the plasma potential adjacent to the substrate in a midfrequency bipolar pulsed magnetron, J. Vac. Sci. Technol. A 21 (2003) L28–L32. https://doi.org/10.1116/1.1622673.

[35] A.D. Pajdarová, T. Kozák, Z. Hubička, M. Čada, P. Mareš, J. Čapek, Plasma parameters in positive voltage pulses of bipolar HiPIMS discharge determined by Langmuir probe with a sub-microsecond time resolution, Plasma Sources Sci. Technol. 29 (2020) 085016. https://doi.org/10.1088/1361-6595/aba773.

[36] S.A. Bello, J.O. Agunsoye, S.B. Hassan, Synthesis of coconut shell nanoparticles via a top down approach: Assessment of milling duration on the particle sizes and morphologies of coconut shell nanoparticles, Mater. Lett. 159 (2015) 514–519. https://doi.org/10.1016/J.MATLET.2015.07.063.

[37] Y. Zhou, C.K. Dong, L.L. Han, J. Yang, X.W. Du, Top-Down Preparation of Active Cobalt Oxide Catalyst, ACS Catal. 6 (2016) 6699–6703. https://doi.org/10.1021/acscatal.6b02416.

[38] M. Parashar, V.K. Shukla, R. Singh, Metal oxides nanoparticles via sol–gel method: a review on synthesis, characterization and applications, J. Mater. Sci. Mater. Electron. 31 (2020) 3729–3749. https://doi.org/10.1007/s10854-020-02994-8.

[39] S. Gauter, F. Haase, P. Solař, O. Kylián, P. Kúš, A. Choukourov, H. Biederman, H. Kersten, Calorimetric investigations in a gas aggregation source, J. Appl. Phys. 124 (2018) 073301. https://doi.org/10.1063/1.5037413.

[40] R. Rudd, A. Obrusník, P. Zikán, C. Hall, P. Murphy, D. Evans, E. Charrault, Plasma gas aggregation cluster source: Influence of gas inlet configuration and total surface area on the heterogeneous aggregation of silicon clusters, Surf. Coatings Technol. 364 (2019) 1–6. https://doi.org/10.1016/j.surfcoat.2019.02.074.

[41] J. Kratochvíl, A. Kuzminova, P. Solař, J. Hanuš, O. Kylián, H. Biederman, Wetting and drying on gradient-nanostructured C:F surfaces synthesized using a gas aggregation source of nanoparticles combined with magnetron sputtering of polytetrafluoroethylene, Vacuum. 166 (2019) 50–56. https://doi.org/10.1016/J.VACUUM.2019.04.050.

[42] C. Liu, L. Zhang, S. Zhang, F. Liu, G. Wang, M. Han, Influence of discharge power on the size of the Pd cluster generated with a magnetron plasma gas aggregation cluster source, Vacuum. 179 (2020) 109486. https://doi.org/10.1016/j.vacuum.2020.109486.

[43] S. Pratontep, S.J. Carroll, C. Xirouchaki, M. Streun, R.E. Palmer, Size-selected cluster beam source based on radio frequency magnetron plasma sputtering and gas condensation, Rev. Sci. Instrum. 76 (2005) 045103. https://doi.org/10.1063/1.1869332.

[44] B.M. Smirnov, I. Shyjumon, R. Hippler, Flow of nanosize cluster-containing plasma in a magnetron discharge, Phys. Rev. E - Stat. Nonlinear, Soft Matter Phys. 75 (2007) 1–9. https://doi.org/10.1103/PhysRevE.75.066402.

[45] M. Drábik, A. Choukourov, A. Artemenko, J. Kousal, O. Polonskyi, P. Solař, O. Kylián, J. Matoušek, J. Pešička, I. Matolínová, D. Slavínská, H. Biederman, Morphology of Titanium Nanocluster Films Prepared by Gas Aggregation Cluster Source, Plasma Process. Polym. 8 (2011) 640–650. https://doi.org/10.1002/ppap.201000126.

[46] A.I. Ayesh, H.A. Ahmed, F. Awwad, S.I. Abu-Eishah, S.T. Mahmood, Mechanisms of Ti nanocluster formation by inert gas condensation, J. Mater. Res. 28 (2013) 2622–2628. https://doi.org/10.1557/jmr.2013.246.

[47] Y. Huttel, ed., Gas-Phase Synthesis of Nanoparticles, Wiley-VCH, 2017. https://doi.org/10.1002/9783527698417.

[48] T. Peter, O. Polonskyi, B. Gojdka, A. Mohammad Ahadi, T. Strunskus, V. Zaporojtchenko, H. Biederman, F. Faupel, Influence of reactive gas admixture on transition metal cluster nucleation in a gas aggregation cluster source, J. Appl. Phys. 112 (2012) 1–7. https://doi.org/10.1063/1.4768528.

[49] R. Gunnarsson, N. Brenning, L. Ojamae, E. Kalered, M.A. Raadu, U. Helmersson, Nucleation of titanium nanoparticles in an oxygen-starved environment. II: Theory, J. Phys. D. Appl. Phys. 51 (2018) 455202. https://doi.org/10.1088/1361-6463/aae113.

[50] A.P. Nikalje, Nanotechnology and its Applications in Medicine, Med. Chem. (Los. Angeles). 5 (2015) 81–89. https://doi.org/10.4172/2161-0444.1000247.

[51] P.K. Jain, I.H. ElSayed, M.A. El-Sayed, Au nanoparticles target cancer, Nano Today. 2 (2007) 18–29. https://doi.org/10.1016/S1748-0132(07)70016-6.

[52] A. Kosmala, R. Wright, Q. Zhang, P. Kirby, Synthesis of silver nano particles and fabrication of aqueous Ag inks for inkjet printing, Mater. Chem. Phys. 129 (2011) 1075–1080. https://doi.org/10.1016/j.matchemphys.2011.05.064.

[53] F. Faupel, V. Zaporojtchenko, T. Strunskus, M. Elbahri, Metal-polymer nanocomposites for functional applications, Adv. Eng. Mater. 12 (2010) 1177–1190. https://doi.org/10.1002/adem.201000231.

[54] S. Haviar, J. Čapek, Š. Batková, N. Kumar, F. Dvořák, T. Duchoň, M. Fialová, P. Zeman, Hydrogen gas sensing properties of WO_3 sputter-deposited thin films enhanced by on-top deposited CuO nanoclusters, Int. J. Hydrogen Energy. 43 (2018) 22756–22764. https://doi.org/10.1016/j.ijhydene.2018.10.127.

[55] S. Xiong, W. Qi, B. Huang, M. Wang, Size-, shape- and composition-dependent alloying ability of bimetallic nanoparticles, ChemPhysChem. 12 (2011) 1317–1324. https://doi.org/10.1002/cphc.201100001.

[56] D. Guo, G. Xie, J. Luo, Mechanical properties of nanoparticles: Basics and applications, J. Phys. D. Appl. Phys. 47 (2014) 013001. https://doi.org/10.1088/0022-3727/47/1/013001.

II Aims of the thesis

This Ph.D. thesis is primarily focused on the investigation of Ta–O–N films with respect to the light-induced water splitting application, prepared by reactive high-power impulse magnetron sputtering. In addition, advanced magnetron-based deposition techniques were investigated in order to enhance the water splitting performance in future research.

The main aims of this Ph.D. thesis are summarized as follows:

1. To systematically investigate films from the Ta–O–N system by finely varying the O to N ratio, with focus on their structure and on the band gap and its position with respect to the water splitting redox potentials.

2. To investigate an advanced deposition technique of bipolar high-power impulse magnetron sputtering. To assess the effect that the applied positive pulse voltage has on the structure and properties of the growing film and to compare it to the more standard approach of application of a bias voltage to the substrates.

3. To investigate the possibilities of a magnetron-based gas aggregation source of nanoparticles in terms of nanoparticle size control. To focus on the interconnectedness of the argon pressure and flow rate and their effect on the nanoparticles size, mass flux and its angular distribution.

III Results

The results are presented here in the form of four scientific papers (Parts A – D) published in impacted international journals. These papers encapsulate the most important results obtained during my Ph.D. study at the Department of Physics, Faculty of Applied Sciences, University of West Bohemia since September 2016.

I deposited all samples in all Parts. In addition, in Part A, I measured the elemental composition of the prepared Ta–O–N films and their electrical resistivity. I actively participated in interpretation of the results and drawing of conclusions. In part B, I measured the elemental composition of the prepared Ta–O–N films and made both cross-sectional and top-view SEM images. I contributed to the concept of the paper and actively participated in interpretation of the results. In part C, I measured the characteristics of the bipolar HiPIMS discharge and participated in their interpretation. I made both cross-sectional and top-view SEM images of all CrN samples, measured their basic properties (thickness and residual stress) and elemental composition. I calculated the estimated energy delivered into the growing films and I actively participated in interpretation of the results. In part D, I measured the deposition characteristics, I made SEM images of all nanoparticle samples and from them I evaluated the nanoparticle size distributions. I measured the nanoparticle mass flux and its angular distribution. I actively participated in interpretation of the results and drawing of conclusions.

I wrote the first version of papers in Parts C and D and later incorporated my supervisors' remarks. I actively participated in completing of the final version of papers in Parts A and B.

A

Effect of annealing on structure and properties of Ta–O–N films prepared by high power impulse magnetron sputtering

J. Čapek, Š. Batková, S. Haviar, J. Houška, R. Čerstvý, P. Zeman

Ceramics International 45 (2019) 9454–9461

Ceramics International 45 (2019) 9454–9461

Contents lists available at ScienceDirect

Ceramics International

journal homepage: www.elsevier.com/locate/ceramint

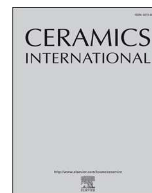

Effect of annealing on structure and properties of Ta–O–N films prepared by high power impulse magnetron sputtering

Jiří Čapek, Šárka Batková, Stanislav Haviar, Jiří Houška, Radomír Čerstvý, Petr Zeman

Department of Physics and NTIS – European Centre of Excellence, University of West Bohemia, Plzeň, Czech Republic

ARTICLE INFO

Keywords:
A. Films
B. Microstructure-final
C. Optical properties
Tantalum oxynitride

ABSTRACT

High power impulse magnetron sputtering of a Ta target in various Ar + O_2 + N_2 gas mixtures was utilized to prepare amorphous tantalum oxynitride (Ta–O–N) films with a finely controlled elemental composition in a wide range. We investigate the effect of film annealing at 900°C in vacuum on structure and properties of the films. We show that the finely tuned elemental composition in combination with the annealing enables the preparation of crystalline Ta–O–N films exhibiting a single TaON phase with a monoclinic lattice structure, refractive index of 2.65 and extinction coefficient of 2.0×10^2 (both at the wavelength of 550 nm), optical band gap width of 2.45 eV (suitable for visible light absorption up to 505 nm), low electrical resistivity of 0.4 Ω cm (indicating enhanced charge transport in the material as compared to the as-deposited counterpart), and appropriate alignment of the band gap with respect to the redox potentials for water splitting. These films are therefore promising candidates for application as visible-light-driven photocatalysts for water splitting.

1. Introduction

Transition-metal oxynitrides are a class of novel multifunctional materials whose properties can be tuned in a wide range by controlling the concentration ratio of N and O atoms in the material [1].

Tantalum oxynitride (Ta–O–N) family of materials has been intensively studied as a promising candidate for application as a visible-light-driven photocatalyst for water splitting [2–5]. However, preparation of these materials in a form of a thin film exhibiting an enhanced water splitting performance is still a challenge for material scientists. The reason is that the material properties needs to meet a number of specific requirements, most importantly [6–8] (i) a proper width of the optical band gap for visible light absorption, (ii) a suitable alignment of the optical band gap with respect to the redox potentials for water splitting and (iii) a suppressed recombination of the generated electron-hole pairs. Particularly the last one is still a major issue nowadays.

Magnetron sputtering is a popular technique in today's search for new materials due to the possibility to prepare a very wide range of high-quality compound and alloy thin films (see Refs. [9–15] reporting on TaON films). However, a precise control of the composition of oxynitride films is often hindered by a much higher affinity of the sputtered metal to oxygen than to nitrogen. This may result in a negligible or, on the contrary, an abrupt change in the elemental composition of the films as the nitrogen fraction in the total reactive gas flow is varying [16,17].

High power impulse magnetron sputtering (HiPIMS) is an advanced magnetron sputtering technique utilizing high discharge target power density (typically several hundred of watts per square centimeter) that is delivered to the target in short pulses [18–21]. The high discharge power during the pulse leads to a generation of a high-density plasma providing several benefits such as high ionization probability of the sputtered target atoms, high dissociation probability of the reactive gas molecules into atoms and high ionization probability of these atoms. These features bring new possibilities how to enhance and tailor film properties, including those of oxynitride films [22,23].

Recently, it has been demonstrated in our laboratories that HiPIMS is a suitable technique for high-rate deposition of Ta–O–N films with a promising band gap width for visible light absorption [24]. However, the band gap alignment of these films has not been investigated. In addition, all the films exhibited X-ray amorphous structure supporting the recombination of the generated electron-hole pairs.

Therefore, in this work we investigate the effect of annealing on the structure and properties of Ta–O–N films especially band gap width and alignment. The films were prepared in a new custom-built deposition system (see Fig. 1) allowing us long-term systematic research on this topic including a future modification of the films by metallic/compound nanoclusters.

E-mail address: jcapek@kfy.zcu.cz (J. Čapek).

https://doi.org/10.1016/j.ceramint.2018.09.019
Received 26 July 2018; Received in revised form 17 August 2018; Accepted 2 September 2018
Available online 07 September 2018
0272-8842/ © 2018 Elsevier Ltd and Techna Group S.r.l. All rights reserved.

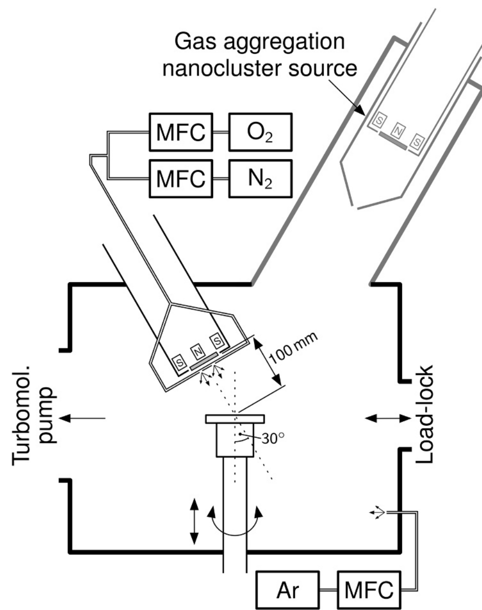

Fig. 1. Schematic diagram of the experimental setup. The gas aggregation nanocluster source was not used in this work, but its utilization is planned for a future modification of the Ta–O–N films.

2. Experimental details

2.1. Film preparation

The Ta–O–N films were deposited in a custom-built high-vacuum sputter system (VAKUUM PRAHA Ltd.) illustrated in Fig. 1. The cylindrical vacuum chamber (500 mm in diameter and 414 mm in height) was pumped by a turbomolecular pump (1250 l/s for N_2, HiPace 1200, Pfeiffer Vacuum) backed up with a scroll pump (35 m^3/h for N_2, XDS35i, Edwards). The base pressure before each deposition was lower than 5×10^{-5} Pa. The depositions were carried out using an unbalanced magnetron equipped with a circular, indirectly water-cooled Ta target (99.95 % purity, 50 mm in diameter, 3.2 mm in thickness).

First, Ar was introduced into the chamber at a flow rate of 50 sccm using a standard gas inlet (see Fig. 1). The pumping speed of the turbomolecular pump was adjusted using a throttle valve to attain an Ar partial pressure of 1 Pa. Subsequently, a mixture of N_2 and O_2 was admitted (via individual mass flow controllers) at corresponding flow rates, ϕ_{N2} and ϕ_{O2}, into the chamber using a corundum tube (inner and outer diameter of 1.0 and 1.6 mm, respectively) positioned parallel to the target surface intersecting the target axis at a distance of 7 mm from the target surface. The tube was equipped with two holes (0.9 mm in diameter) positioned symmetrically 15 mm from the target axis and oriented toward the substrate. Values of ϕ_{N2} and ϕ_{O2} were regulated using mass-flow controllers (MFCs) controlled by a PID unit (647C, MKS Instruments) in order to keep the total pressure during the reactive deposition constant at 1.095 Pa for all depositions, while the preset nitrogen fraction in the total reactive gas flow, $f_{N2} = \phi_{N2}/(\phi_{O2} + \phi_{N2})$, was set to a constant value from the whole range (0–100 %) for a given deposition.

The magnetron (HVM Plasma Ltd.) was driven by a high power pulsed direct current power supply (HMP 2/1, Hüttinger Elektronik). The negative-voltage pulse duration, t_{ON}, and the pulse repetition frequency, f_r, were kept constant at 50 μs and 170 Hz, respectively. The corresponding duty cycle, t_{ON}/T, was 0.85 %, where the pulse period $T = 1/f_r$.

The waveforms of the target voltage, $U_T(t)$, and discharge target current, $I_d(t)$, were recorded by a digital oscilloscope (PicoScope 6403C, Pico Technology) using voltage (TT-HV 150, Testec) and current (CT-E0.5-B, Bergoz) probes. The average discharge target power density in a pulse was evaluated as

$$P_{da} = \frac{1}{t_{ON}A_T}\int_0^{t_{ON}} U_T(t)I_d(t)\mathrm{d}t, \tag{1}$$

where A_T stands for the total target area ($\approx$ 20 cm^2 in our case). The average discharge target power density in a period, $\overline{P_d}$, was evaluated accordingly as

$$\overline{P_d} = \frac{1}{TA_T}\int_0^{T} U_T(t)I_d(t)\mathrm{d}t. \tag{2}$$

In this work, P_{da} and $\overline{P_d}$ values were kept constant at 1000 W/cm^2 and 10 W/cm^2, respectively.

The films were deposited onto polished and ultrasonically pre-cleaned Si(100) substrates or Si(100) substrates covered with thermally grown SiO_2 (for electrical resistivity measurements), held at a floating potential without any external heating. The substrates were positioned at a distance of 100 mm from the target (see Fig. 1) and were rotated at a speed of 40 rpm. The deposition time was 50 min. The resulting film thickness was measured by profilometry (DEKTAK 8 Stylus Profiler, Veeco) at the film edge formed by an application of a removable thin silicon mask on the substrate during the deposition. The resulting values of the deposition rate gradually increased from 8.5 nm/min at f_{N_2} = 0 % up to the maximum value of 13.0 nm/min at f_{N_2} = 75 % and then gradually decreased down to 4.6 nm/min at f_{N_2} = 100 %.

The prepared films were annealed for 5 min at temperatures up to 900°C in a stainless-steel vacuum furnace (AS-One 100 RTP, Annealsys); heating and cooling were carried out both at a rate of 30°C/min. The pressure in the furnace prior to each annealing process was 1×10^{-3} Pa.

2.2. Film characterization

2.2.1. Elemental composition and structure of films

The elemental composition was determined by wavelength dispersive spectroscopy (MagnaRay, Thermo Scientific) performed in a scanning electron microscope (SU-70, Hitachi) using a primary electron energy of 10 kV.

X-ray diffraction (XRD) measurements were carried out at room temperature using a diffractometer (Xpert PRO, PANalytical) in the Bragg-Brentano configuration with CuKα (40 kV, 40 mA) radiation. To avoid a strong reflection from the Si(100) substrate, a slightly asymmetrical diffraction geometry with an ω-offset of 1.5° was used.

The grain size of the annealed films was estimated from scanning electron micrographs (top views) of the films acquired by a scanning electron microscope (SU-70, Hitachi) operated in a secondary electron mode with a primary electron energy of 5 kV. Good contrast of individual grains and observable grain boundaries enabled determination of statistics of equivalent diameters of the projected areas of the grains. In the text bellow we discuss a mean grain size diameter gathered from these statistics.

2.2.2. Optical properties of films

The refractive index, *n*, and extinction coefficient, *k*, were determined by variable angle spectroscopic ellipsometry (VASE) using the J.A. Woollam Co. Inc. instrument. The measurements were performed using angles of incidence of 65°, 70° and 75° in reflection. The optical data were fitted for wavelength, λ, in the range 250–2000 nm using the WVASE software (below we also discuss *n* and *k* at a specific λ = 550 nm, n_{550} and k_{550}). The optical model consisted of a Si substrate, a Ta–O–N layer and a surface roughness layer.

The optical band gap (except the zero band gap of N-rich compositions) was evaluated by describing the dispersion of optical constants of Ta–O–N by a single dispersion formula which includes the band gap amongst its parameters: the CodyLorentz formula (oscillator) [25] which for the imaginary part of the relative permittivity, ε_2, reads

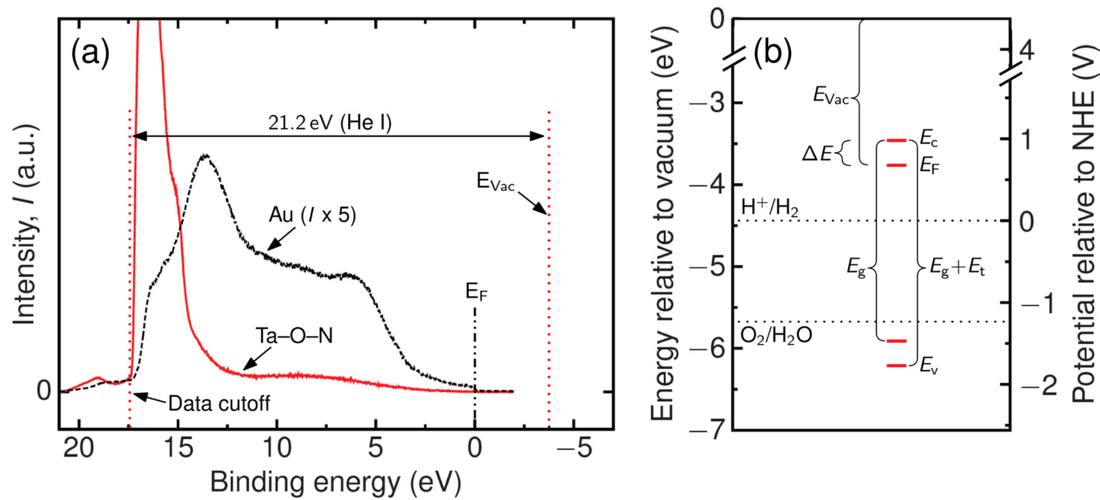

Fig. 2. Example of UPS spectra for the Ta–O–N film and the circular gold area (deposited on the film) (a), and of the band gap alignment determined based on a combination of the UPS and spectroscopic ellipsometry data (b). The presented data are for the annealed film prepared at f_{N_2} = 90 % exhibiting the single TaON phase with the monoclinic lattice structure.

$$\varepsilon_2 = L(E)G(E) \quad \text{for} \quad E \geq E_g + E_t \tag{3}$$

and

$$\varepsilon_2 = L(E_g + E_t)G(E_g + E_t)\frac{(E_g + E_t)}{E}\exp\left(\frac{E - E_g - E_t}{E_u}\right) \quad \text{for} \quad E < E_g + E_t, \tag{4}$$

where

$$L(E) = \frac{AB\mathrm{E}_n E}{(E^2 - E_n^2)^2 + B^2E^2} \text{ (Lorentz oscillator)} \tag{5}$$

and

$$G(E) = \frac{(E - E_g)^2}{(E - E_g)^2 + E_p^2} \quad \text{(Cody form of the variable band edge function).} \tag{6}$$

Here, E is the photon energy, A is the oscillator amplitude, B is the oscillator broadening, E_n is the energy at which the Lorentz oscillator is centered (also referred to as the peak transition energy), E_p is the transition energy between the onset behavior (at $E_g + E_t < E < E_g + E_p$) and the Lorentz oscillator behavior (at $E > E_g + E_p$; note that $G(E) \approx 1$ at $E \gg E_g + E_p$), E_g is the ("narrowly defined" – see E_t below) optical band gap, $E_g + E_t$ is the transition between band-to-band transitions and the exponential Urbach absorption tail (that is, a more "widely defined" optical band gap) and E_u is the energy representing the shape of the Urbach absorption tail (which exists when the structural disorder and defects and the consequent presence of highly localized states in the material (particularly close to the band gap edges) lead to $E_t > 0$).

The presented dispersions of optical constants themselves were obtained from high-precision optical models where the particular Ta–O–N material was described by a variety of oscillators:

- Cody-Lorentz: f_{N_2} in the range 0–80 % for the as-deposited films and 50–80 % for the annealed films,
- Cody-Lorentz + two UV-centered Lorentz oscillators: f_{N_2} in the range 0–37.5 % for the annealed films,
- Cody-Lorentz + one IR-centered Lorentz oscillator: f_{N_2} in the range 85–95 % for the as-deposited films and 85–90 % for the annealed films, and
- combination of 4–5 Lorentz oscillators (including one centered around zero energy, i.e. Drude oscillator representing free charge carriers): f_{N_2} in the range 97.5–100 % for the as-deposited films and 90–100 % for the annealed films.

These optical models constitute reasonable trade-offs between the fit quality and the number of oscillators. In parallel, there is a straightforward physical motivation behind the oscillator selection: the Cody-Lorentz oscillator is one of the state of the art choices for materials with a band gap, the Lorentz oscillators centered in UV capture the effect of large grains formation during the annealing of the films and the resulting light scattering on the grains (discussed in Section 3.3.2), and the Lorentz oscillators centered in IR (at zero energy - which converts the Lorentz oscillator to the Drude oscillator - or close to it) capture the effect of free charge carriers (discussed in Sec. 3.3.4).

2.2.3. *Electrical resistivity and band gap alignment*

Electrical resistivity of the films was measured by a standard four-point technique with a 1.047-mm spacing between tips.

Band gap alignment of the films was determined by ultraviolet photoemission spectroscopy (UPS) following the methodology described in detail in Ref. [26]. UPS spectra were taken with He I (21.2 eV) UV light and recorded with a constant pass energy of 1.5 eV. The film was biased to − 10 V during each measurement in order to measure the secondary electron cutoff. The measuring spot was cleaned prior to the measurement for 30 min by Ar ions using ion energy of 1 keV and ion current density of 300 nA/cm^2.

As demonstrated in Fig. 2, the obtained UPS spectrum of the film was first referenced to the Fermi edge, E_F, of a circular gold area with a diameter of 2 mm, which was ex-situ sputter-deposited onto the film. Upon the determination of the cutoff of the UPS spectrum of the film, the corresponding energy position of the vacuum level, E_{Vac}, was obtained by taking into account the energy of the used UV photons (21.2 eV). Based on works of Matsumoto [27] and Chun et al. [26], one can expect that the bottom level of the conduction band of a Ta–O–N film is not more positive than 0.3 eV with respect to E_F. In this work we thus assume a fixed difference $\Delta E = E_F - E_c = -0.3$ eV. Note that this difference is the worst possible situation for the band gap alignment with respect to the water splitting potentials. Due to a large error in the determination of the E_v value from the UPS spectra, we present E_v calculated as $E_v = E_c - (E_g + E_t)$, where E_g and E_t values were obtained during the spectroscopic ellipsometry measurements (described above in Section 2.2.2).

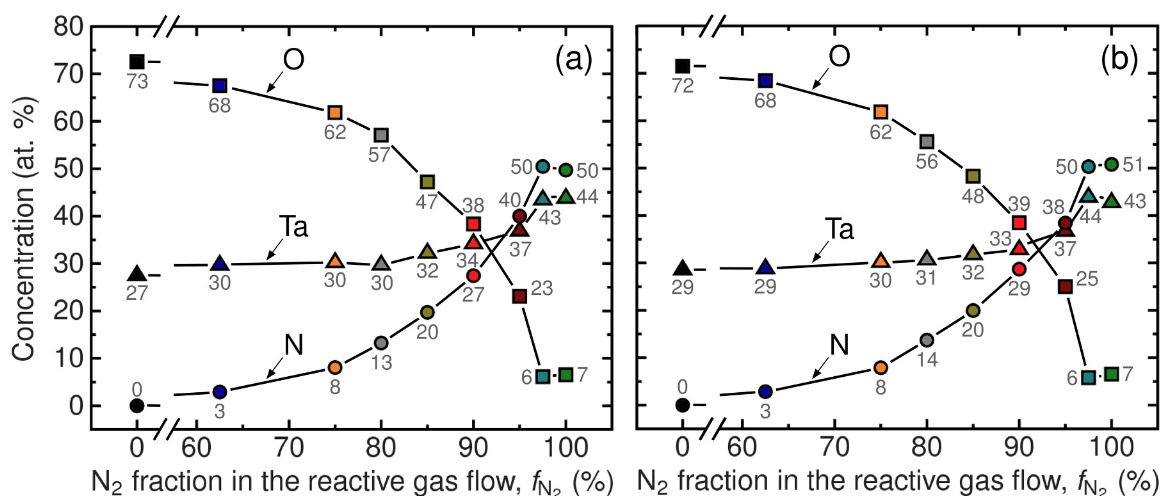

Fig. 3. Elemental composition of Ta–O–N films before (a) and after (b) annealing at 900°C in a vacuum furnace. The films were prepared at various nitrogen fractions in the total reactive gas flow, f_{N_2}. The indicated values are rounded to integers.

3. Results and discussion

In this part, we first systematically present and discuss the effect of annealing of the Ta–O–N films on elemental composition (Fig. 3), structure (Fig. 4), dispersion curves of refractive index, n (top panels in Fig. 5) and extinction coefficient, k (bottom panels in Fig. 5), optical band gap width, E_g (Fig. 6) and electrical resistivity, ρ (Fig. 7) of the Ta–O–N films. On the basis of these results we discuss the possible Ta–O–N candidates for water-splitting application. We also discuss how the band gap of the most promising candidate is aligned with respect to redox potentials for water splitting (Fig. 8).

3.1. Elemental composition

Fig. 3 shows that the elemental composition (in at %) of the as-deposited Ta–O–N films was systematically varied in a wide range from $Ta_{27}O_{73}N_0$ to $Ta_{44}O_7N_{50}$ by controlling the nitrogen fraction in the total reactive gas flow, f_{N2}. The elemental composition of the film prepared at f_{N2} = 0 % ($Ta_{27}O_{73}N_0$) corresponds to a stoichiometric Ta_2O_5. Although the increase in f_{N2} from 0 to 62.5 % leads to only a small rise in

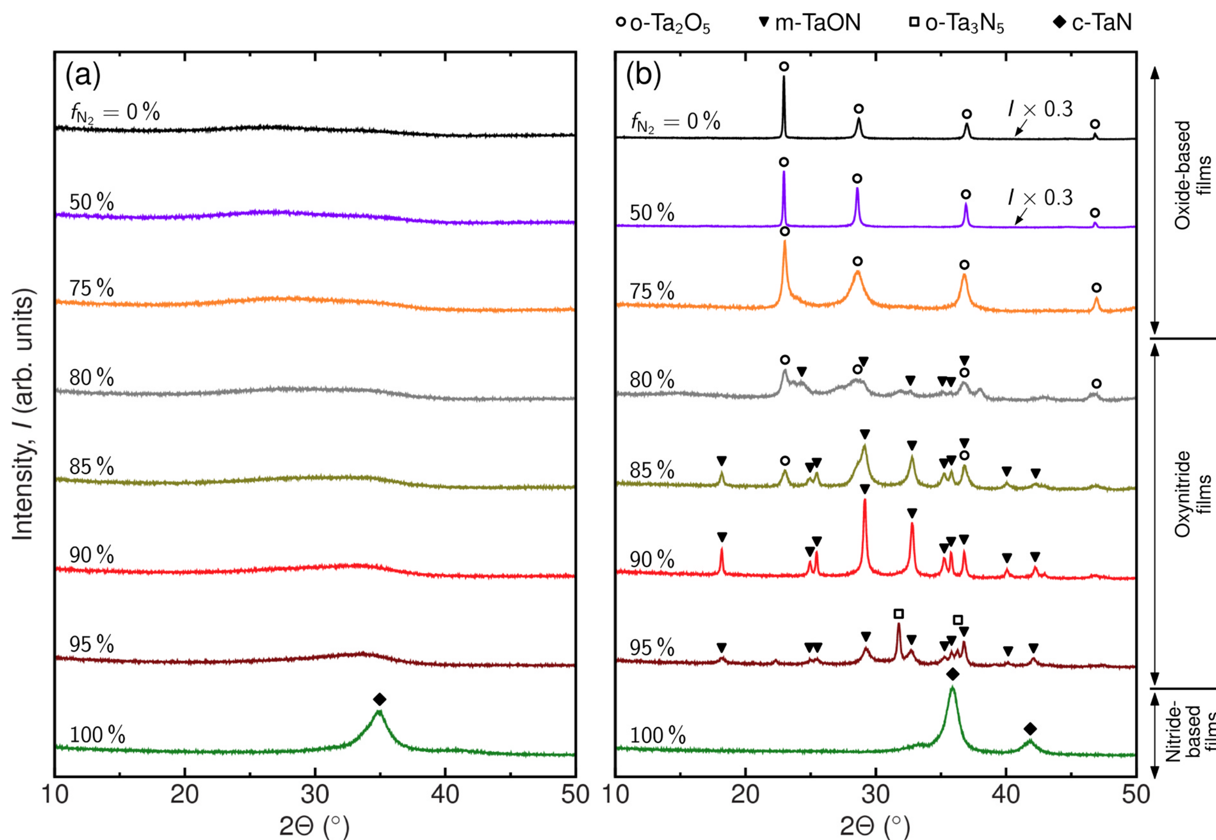

Fig. 4. XRD patterns taken from Ta–O–N films before (a) and after (b) annealing at 900°C in a vacuum furnace. The films were prepared at various nitrogen fractions in the total reactive gas flow, f_{N_2}. XRD patterns were recorded at room temperature. The identified phases of orthorhombic Ta_2O_5, monoclinic TaON, orthorhombic Ta_3N_5 and cubic TaN are indicated by circles, triangles, squares and diamonds, respectively.

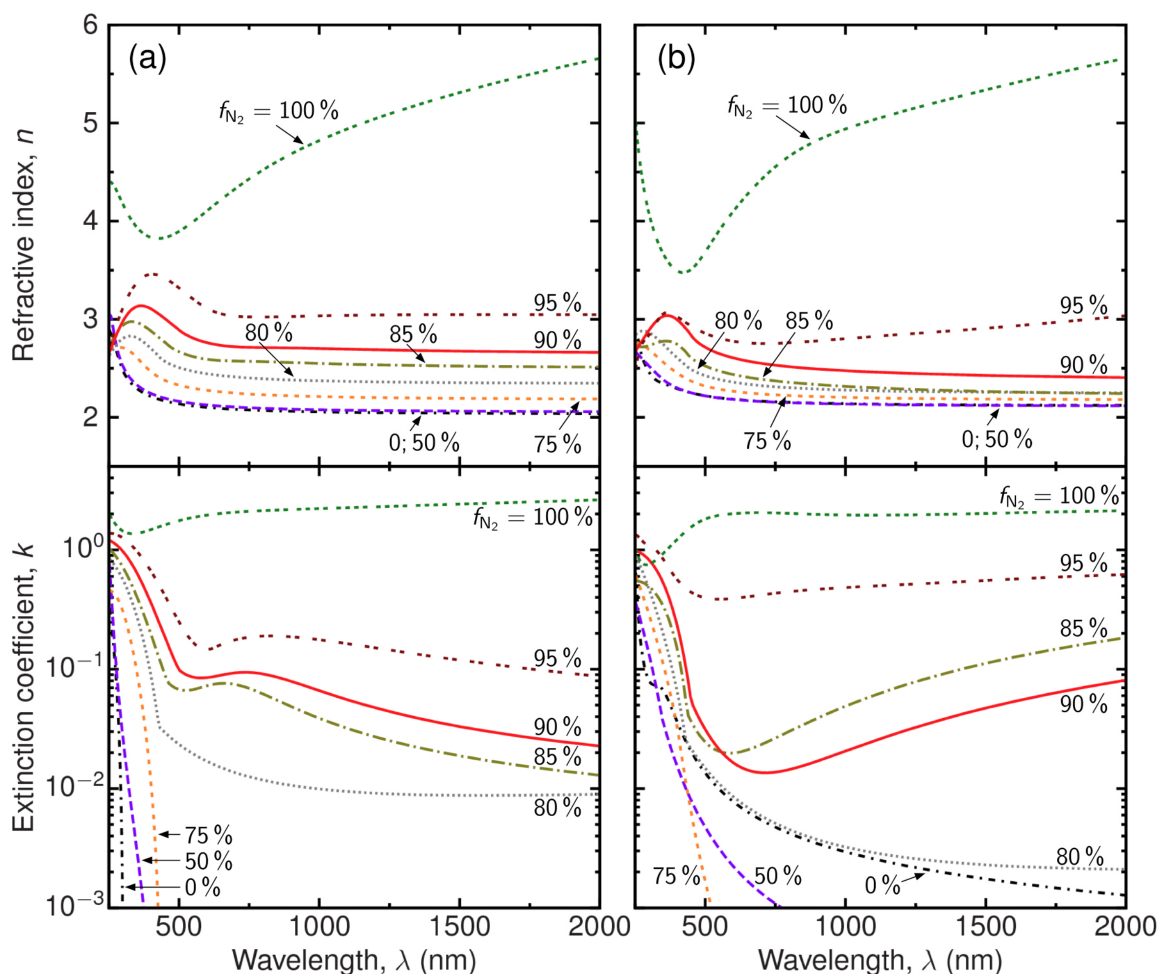

Fig. 5. Dispersion curves of refractive index, *n*, (top panels) and extinction coefficient, *k*, (bottom panels) for TaON films before (a) and after (b) annealing at 900°C in a vacuum furnace. The films were prepared at various nitrogen fractions in the total reactive gas flow, f_{N_2}.

the N content in the films (from 0 to 3 at %), the further increase in f_{N2} from 62.5 to 100 % results in a significant rising incorporation of N atoms (from 3 to 50 at %) into the films at a decreasing content of O atoms (from 68 to 7 at %). The non-zero content of oxygen at f_{N2} = 100 % is a consequence of the release of the adsorbed and subplanted oxygen from the chamber walls during the deposition. The rise in the Ta content (from 27 to 44 at. %) with the increasing f_{N2} value can be mainly attributed to different Ta contents in the corresponding stoichiometric binary phases (Ta_2O_5 versus TaN).

The annealing of the prepared films practically did not affect their elemental composition as can be seen by comparing Figs. 3a and 3b (the small variation in the values is within the error of the analysis used).

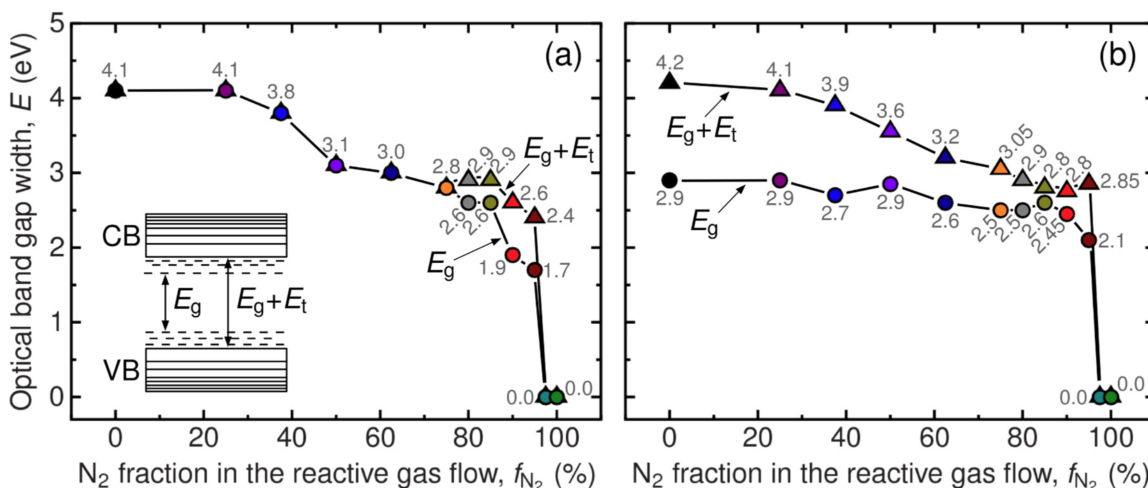

Fig. 6. Optical band gap widths, E_g and $E_g + E_t$, of Ta–O–N films before (a) and after (b) annealing at 900°C in a vacuum furnace. The films were prepared at various nitrogen fractions in the total reactive gas flow, f_{N_2}.

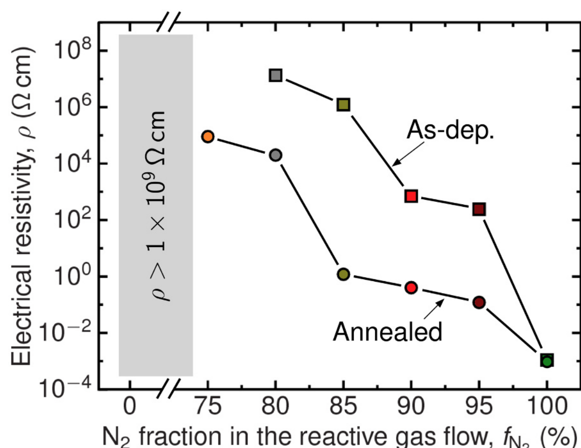

Fig. 7. Electrical resistivity, ρ, of Ta–O–N films before and after annealing at 900 °C in a vacuum furnace. The films were prepared at various nitrogen fractions in the total reactive gas flow, f_{N_2}.

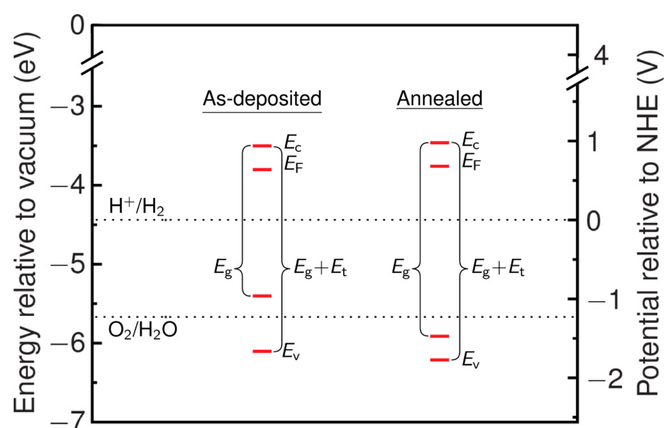

Fig. 8. Band gap alignment of the Ta–O–N film prepared at f_{N_2} = 90 % before (as-deposited state) and after annealing at 900°C in a vacuum furnace. The redox potentials for hydrogen (H^+/H_2) and oxygen (O_2/H_2O) production are indicated (dotted lines).

This is very beneficial for the present study because of the possibility to investigate properties of not only amorphous, but also crystalline Ta–O–N films in wide ranges of practically identical elemental compositions.

3.2. Structure of films

The XRD patterns presented in Fig. 4a indicate X-ray amorphous structure of all the as-deposited Ta–O–N films except for the film prepared at f_{N2} = 100 %, which exhibits a single nanocrystalline cubic TaN (c–TaN) structure (PDF Card No. 00-049-1283). A similar set of XRD patterns was also obtained after their annealing at temperatures up to 800°C (results not presented here), which indicates that the X-ray amorphous structure of the films prepared in a wide range of elemental compositions (i.e., at f_{N2} in the range 0 – 95 %) is thermally stable up to such a high temperature.

The annealing of the films at 900°C leads to their crystallization as indicated by the corresponding XRD patterns in Fig. 4b. The films prepared at f_{N2} in the range 0 – 75 % exhibit a single orthorhombic Ta_2O_5 (o–Ta_2O_5) phase (PDF Card No. 00-025-0922). A further incorporation of N atoms into the films corresponding to the rise in f_{N2} from 75 to 90 % leads to a gradual replacement of the o–Ta_2O_5 phase by a monoclinic TaON (m–TaON) phase (PDF Card No. 01-083-4964). Here, we highlight for the further discussion below that the annealing of the Ta–O–N film prepared at f_{N2} = 90 % leads to a crystallization of a single m–TaON phase. A further increase in the f_{N2} value up to 95 % leads to a formation of an orthorhombic Ta_3N_5 (o–Ta_3N_5) phase (PDF Card No. 04-007-1969) along with the m–TaON phase. At f_{N2} = 100 %, a single c–TaN phase is observed.

For the rest of this work the investigated as-deposited and annealed films are categorized based on their structure after the annealing into three material groups: (i) Oxide-based films ($f_{N2} \leq 75$ %), (ii) Oxynitride films (75 % < $f_{N2} \leq 95$ %) and (iii) Nitride-based films (f_{N2} > 95 %) as also indicated in Fig. 4.

3.3. Properties of films based on their electronic structure

Generally, n, k, E and ρ of the as-deposited films change gradually and monotonically (in a wide range of λ in the case of n and k) as functions of f_{N2} value (see the top and bottom panels in Fig. 5a, Figs. 6a and 7, respectively), which is a consequence of the gradual and fine change of the elemental composition (discussed in Section 3.1). This brings an advantage of tuning the material properties for a particular application.

The individual characteristics of the as-deposited and annealed films are further discussed in detail in the following paragraphs related to the three material groups. Note that discussed changes in the characteristics of the annealed films are with respect to their as-deposited counterparts.

3.3.1. As-deposited oxide-based films ($f_{N2} \leq 75$ %)

The optical properties of the as-deposited oxide-based films are characterized by a variable E_g at $E_t = 0$ (indicating sharp edges of the bands).

The high refractive index n_{550} = 2.11 confirms (by agreement with e.g. n_{550} = 2.13 in Ref. [28]) that the film deposited at f_{N_2} = 0 % is well densified. This material is further described by a wide E_g of 4.1 eV allowing absorption of only UV light up to 300 nm. The wide band gap also leads to a very high value of ρ (higher than 1×10^9 Ω cm – which is the limit of our electrical resistivity measurement).

The films prepared at f_{N_2} of 50 and 75 % exhibit similar dispersion curves of n and k as in the previous case. However the gradual incorporation of N atoms into the Ta_2O_5 lattice results in an increase in n value (n_{550} = 2.3 for f_{N_2} = 75 %) and a shift of the absorption edge to a longer λ corresponding to a decrease in E_g (E_g = 2.8 eV for f_{N_2} = 75 %). Let us point out that E_g = 2.8 eV already corresponds to UV–VIS light absorption up to 440 nm. The corresponding ρ value is still beyond the limit of our four-point probe.

3.3.2. Annealed oxide-based films

The annealing of the oxide-based films leads to only a small increase or even no changes in n values (n_{550} = 2.29 for f_{N_2} = 75 % after the annealing). However, a considerable shift of the dispersion curves of k to higher values is observed. This decrease in the transparency of the films is represented by the increased E_t value (see Fig. 6b) in the Cody-Lorentz formula. This behavior can be correlated with large grains of the annealed oxide-based films prepared at low f_{N_2}. The grain size is on the same order (~ μm) as λ of the light used during the ellipsometry measurements and therefore light scattering takes place on the grains. Since the grain size of the films decreases with increasing content of N atoms in the material (from about 2.5 μm for f_{N_2} = 0 % down to about 0.2 μm for f_{N_2} = 75 %), the scattering effect successively diminishes with increasing f_{N_2} value in the range 0 – 75 %.

The annealing of the film prepared at f_{N_2} = 75 % further leads to a substantial (at least four orders of magnitude) decrease in ρ from a value higher than 1×10^9 Ω cm (limit of our four-point probe) down to 9.0×10^4 Ω cm. This drop can be mainly attributed to the reduced E_g value of 2.5 eV and also an enhanced mobility of the generated charges in the crystalline material.

3.3.3. As-deposited oxynitride films ($75\,\% < f_{N2} \leq 95\,\%$)

The as-deposited film prepared at $f_{N_2} = 80\,\%$ is characterized by $n_{550} = 2.47$ and the dispersion curve of k above 8×10^{-3} for all values of λ investigated. The resulting E_g and E_t values are 2.6 eV and 0.3 eV, respectively. While $E_g + E_t$ is larger than for the $f_{N_2} = 75\,\%$ case, the lower E_g leads to an enhanced absorption of light in the material and also to a lower ρ of $1.3 \times 10^7\ \Omega$ cm. The non-zero E_t value represents extra energy levels inside the band gap (as illustrated in the inset in Fig. 6a and described in detail in Section 2.2.2).

The film prepared at $f_{N_2} = 85\,\%$ exhibits $n_{550} = 2.62$. While the band gap $E_g + E_t$ of this film is the same as for $f_{N_2} = 80\,\%$, k values are higher for all values of λ investigated and ρ decreases down to $1.2 \times 10^6\ \Omega$ cm. This probably indicates higher density of the extra energy levels in the band gap.

An even stronger incorporation of N atoms into the films prepared at f_{N_2} of 90 and 95 % leads to a further rise in n ($n_{550} = 2.80$ and $n_{550} = 3.20$ for $f_{N_2} = 90\,\%$ and $f_{N_2} = 95\,\%$, respectively), which has also been reported in Ref. [14] and k ($k_{550} = 0.09$ and $k_{550} = 0.17$ for $f_{N_2} = 90\,\%$ and $f_{N_2} = 95\,\%$, respectively). In addition, E_g substantially decreases (1.9 eV and 1.7 eV for $f_{N_2} = 90\,\%$ and $f_{N_2} = 95\,\%$, respectively), but at an E_t value of 0.7 eV in both cases. Such low E_g values allows absorption of UV–VIS light up to 650 nm for $f_{N_2} = 90\,\%$ or even up to 730 nm for $f_{N_2} = 95\,\%$. However, the relatively high E_t value increases the uncertainty of the narrow band gap alignment with respect to the redox potentials as discussed in the following Section 3.4. For completeness, let us also mention here that the decrease in the band gap width also leads to a considerable drop in ρ ($7.0 \times 10^2\ \Omega$ cm for $f_{N_2} = 90\,\%$ and $2.4 \times 10^2\ \Omega$ cm for $f_{N_2} = 95\,\%$).

3.3.4. Annealed oxynitride films

The annealing of the film prepared at $f_{N_2} = 80\,\%$ does not significantly affect the dispersion curve of n ($n_{550} = 2.38$), but leads to a decrease in k for all values of λ investigated. Since the E_g value is decreased by 0.1 eV down to 2.5 eV at $E_t = 0.4$ eV, the decrease in k indicates a lower density of the energy levels in the E_t part of the band gap. However, the situation might be even more complex since the material is inhomogeneous due to the forming a mixture of Ta_2O_5 and TaON phases (see Fig. 4b). The slight decrease in E_g along with the crystallization of the material leads to a decrease in ρ down to $2.0 \times 10^4\ \Omega$ cm.

The annealing of the films prepared at f_{N_2} of 85 and 90 % leads to dispersion curves characterized by a steeper decrease in n for $\lambda > 500$ nm and by a more pronounced decrease in k in the VIS range followed by an increase in k in the NIR range. The change in k can be attributed to an increase in the concentration of the free charge carriers. The film prepared at $f_{N_2} = 85\,\%$ exhibits an unchanged E_g value, but E_t decreases down to 0.2 eV. Note that this E_t is the minimum value from among all the crystalline films investigated. This value indicates relatively sharp edges of the band gap despite the fact that the material consists of a mixture of TaON and Ta_2O_5 phases. Band gap of the crystalline film prepared at $f_{N_2} = 90\,\%$ is characterized by an increased $E_g = 2.45$ eV and decreased $E_t = 0.3$ eV. Note that these changes are crucial for the appropriate band gap alignment of this material with respect to the redox potentials as discussed in the following Section 3.4. The crystallization of these films leads to a decrease in ρ down to $1.2\ \Omega$ cm and $0.4\ \Omega$ cm for $f_{N_2} = 85\,\%$ and $f_{N_2} = 90\,\%$, respectively.

The annealing of the film prepared at $f_{N_2} = 95\,\%$ leads to dispersion curves characterized by a steeper rise in n for $\lambda > 650$ nm and significantly higher k values for $\lambda > 500$ nm. This behavior can be explained by a further rise in the concentration of free charge carriers. Optical band gap of this film is also characterized by an increased $E_g = 2.1$ eV, but at a relatively high $E_t = 0.75$ eV. The crystallization of this film also leads to a decrease in ρ down to $1.2 \times 10^{-1}\ \Omega$ cm.

3.3.5. Nitride-based films ($f_{N2} > 95\,\%$)

The nitride-based crystalline films exhibit non-measurable E_g, very high k values and $\rho = 1.1 \times 10^{-3}\ \Omega$ cm, all indicating metallic behavior. Note that for the as-deposited films the decrease in the slope of $\rho(f_{N_2})$ is much larger between $f_{N_2} = 95$ and 100 % than at $f_{N_2} \leq 95\,\%$ (see Fig. 7). This is consistent with the fact that in the former case the film structure changes along with the composition (c-TaN forms at $f_{N_2} = 100\,\%$, see Fig. 4a) and the mobility of free charge carriers increases accordingly. The annealing of the films does not significantly affect any of the discussed properties since the annealed films exhibit similar nanocrystalline structure as the as-deposited counterparts.

3.4. Promising candidates for water splitting

Highly crystalline materials are required for the water-splitting application to ensure an efficient charge transport leading to a reduced recombination (longer mean free paths) of the generated electron–hole pairs in the material as compared to their amorphous counterparts. In this work, the reduced recombination is indicated by the substantial drop in the electrical resistivity of the films after the annealing (see Fig. 7).

The crystalline non-metal films with low band gap values (prepared at f_{N_2} in the range $75 - 95\,\%$) are further favoured from the point of view of a maximum utilization of sunlight for generation of electron–hole pairs. Taking into account only the narrowly defined E_g values, these materials absorb UV–VIS light up to 505 nm for $f_{N_2} = 90\,\%$ or even up to 590 nm for $f_{N_2} = 95\,\%$.

The crystalline single-phase films prepared at f_{N_2} of 75 and 90 % provide two additional advantages. First, grain boundaries of the single-phase materials are more suitable for charge transport as compared to the two-phase films. This is due to the appearance of contact potentials and tunneling barriers from band bending at the two-phase grain boundaries as the two phases have different band structures. This feature is important for an optimization of the light absorption in a film with a required thickness larger than a grain size of the material. Second, the material characteristics discussed in Section 3.3 represent the real properties of these single-phase materials and not a combination of the properties of multiple-constituent phases as it is for the films prepared at f_{N_2} of 80, 85 and 95 %. This may be crucial for the performance of the material in the water-splitting application and also for a detailed understanding of the water-splitting process.

The extra energy levels in the band gap (described by the E_t value) may hinder the alignment of the narrow band gaps with respect to water-splitting redox potentials. Such a situation is shown in Fig. 8 for the as-deposited film prepared at $f_{N_2} = 90\,\%$ when the bottom level of the band gap is undesirably above the potential for oxygen production. Unfortunately, we cannot state more precisely (based on the analysis used) how exactly the extra energy levels are distributed at the two band gap edges. In Fig. 8, we therefore present the worst possible situation when all the extra levels are positioned at the bottom edge of the band gap. Taking into account this issue, the crystalline single-phase material with a minimum E_t value is furthermore preferable for the water-splitting application. This is the case of the annealed film prepared at $f_{N_2} = 90\,\%$ exhibiting E_t value of only 0.3 eV at $E_g = 2.45$ eV. As one can see in Fig. 8, the alignment of the band gap of this film is suitable for the water-splitting reactions no matter where the extra energy levels are.

Based on this discussion, the crystalline single-phase TaON material with the monoclinic lattice structure (prepared at $f_{N_2} = 90\,\%$ and annealed) exhibits the most promising properties with respect to the water splitting process among all the Ta–O–N materials investigated and will be a subject of a future study.

4. Summary and conclusions

In this paper, we investigated the effect of annealing at 900°C in vacuum on properties of tantalum oxynitride (Ta–O–N) films prepared by high power impulse magnetron sputtering (HiPIMS). Special

attention was paid to the possibility to prepare Ta–O–N films with properties suitable for water-splitting application under visible light irradiation.

The Ta–O–N films were prepared with a finely controlled elemental composition in a wide range (from $Ta_{27}O_{73}N_0$ to $Ta_{44}O_7N_{50}$) by controlling a single deposition parameter of nitrogen fraction in the reactive gas flow rate, f_{N_2}. The properties (refractive index, n, extinction coefficient, k, optical band gap width, E_g, and electrical resistivity, ρ) of the as-deposited films also changed as functions of f_{N_2}. However, all the as-deposited films exhibited amorphous structure, which is undesirable for the water-splitting application.

The annealing process did not affected the elemental composition of the films, but led to their crystallization. The structure of the films gradually changed from an orthorhombic Ta_2O_5 phase via a monoclinic TaON phase to a cubic TaN phase as a function of f_{N_2}.

The important result of the present work is the demonstration that the used approach (HiPIMS deposition of Ta–O–N films in combination with the annealing of the films) can be utilized for a preparation of the crystalline Ta–O–N film exhibiting a single TaON phase with a monoclinic structure. This film exhibits $E_g = 2.45$ eV (suitable for visible-light absorption up to 505 nm), low ρ of 0.4 Ω cm (indicating enhanced charge transport in the material as compared to the as-deposited counterpart) and appropriate alignment of the band gap with respect to the redox potentials for water splitting.

In our future work, we will focus on a further optimization of the deposition conditions (e.g., substrate temperature and substrate bias potential) in order to induce the growth of the crystalline TaON phase already during the film deposition at a reasonably low substrate temperature.

Acknowledgments

This work was supported by the project LO1506 of the Czech Ministry of Education, Youth and Sports under the program NPU I. The authors wish to thank Dr. Tomáš Duchoň for the carried out UPS analyses of the films and Dr. Šimon Kos for valuable discussion of the results.

References

[1] F. Vaz, N. Martin, M. Fenker (Eds.), Metallic Oxynitride Thin Films by Reactive Sputtering and Related Deposition Methods: Process Properties and Applications, Bentham Science Publishers, 2013, , https://doi.org/10.2174/97816080515641130101.
[2] M. Hara, G. Hitoki, T. Takata, J.N. Kondo, H. Kobayashi, K. Domen, TaON and ta3n5 as new visible light driven photocatalysts, Catal. Today 78 (1–4) (2003) 555–560, https://doi.org/10.1016/s0920-5861(02)00354-1.
[3] R. Abe, Recent progress on photocatalytic and photoelectrochemical water splitting under visible light irradiation, J. Photochem. Photobiol. C: Photochem. Rev. 11 (4) (2010) 179–209, https://doi.org/10.1016/j.jphotochemrev.2011.02.003.
[4] C. Zhen, R. Chen, L. Wang, G. Liu, H.-M. Cheng, Tantalum (oxy)nitride based photoanodes for solar-driven water oxidation, J. Mater. Chem. A 4 (8) (2016) 2783–2800, https://doi.org/10.1039/c5ta07057k.
[5] J. Seo, H. Nishiyama, T. Yamada, K. Domen, Visible-light-responsive photoanodes for highly active, stable water oxidation, Angew. Chem. Int. Ed. 57 (28) (2018) 8396–8415, https://doi.org/10.1002/anie.201710873.
[6] T. Bak, J. Nowotny, M. Rekas, C. Sorrell, Photo-electrochemical hydrogen generation from water using solar energy. Materials-related aspects, Int. J. Hydrog. Energy 27 (10) (2002) 991–1022, https://doi.org/10.1016/s0360-3199(02)00022-8.
[7] A. Kudo, Y. Miseki, Heterogeneous photocatalyst materials for water splitting, Chem. Soc. Rev. 38 (1) (2009) 253–278, https://doi.org/10.1039/b800489g.
[8] T. Jafari, E. Moharreri, A. Amin, R. Miao, W. Song, S. Suib, Photocatalytic water splitting-the untamed dream: a review of recent advances, Molecules 21 (12) (2016) 900, https://doi.org/10.3390/molecules21070900.
[9] O. Banakh, P.-A. Steinmann, L. Dumitrescu-Buforn, Optical and mechanical properties of tantalum oxynitride thin films deposited by reactive magnetron sputtering, Thin Solid Films 513 (1–2) (2006) 136–141, https://doi.org/10.1016/j.tsf.2006.01.060.
[10] H.L. Dréo, O. Banakh, H. Keppner, P.-A. Steinmann, D. Briand, N. de Rooij, Optical, electrical and mechanical properties of the tantalum oxynitride thin films deposited by pulsing reactive gas sputtering, Thin Solid Films 515 (3) (2006) 952–956, https://doi.org/10.1016/j.tsf.2006.07.054.
[11] D. Cristea, D. Constantin, A. Crisan, C. Abreu, J. Gomes, N. Barradas, E. Alves, C. Moura, F. Vaz, L. Cunha, Properties of tantalum oxynitride thin films produced by magnetron sputtering: the influence of processing parameters, Vacuum 98 (2013) 63–69, https://doi.org/10.1016/j.vacuum.2013.03.017.
[12] M. Ratova, G. West, P. Kelly, Visible light activated photocatalytic TaON coatings deposited via pulsed-DC magnetron sputtering, Vacuum 109 (2014) 135–138, https://doi.org/10.1016/j.vacuum.2014.07.018.
[13] A. Bousquet, F. Zoubian, J. Cellier, T. Sauvage, E. Tomasella, Control the composition of tantalum oxynitride films by sputtering a tantalum target in ar/o2/n2radiofrequency magnetron plasmas, Plasma Process. Polym. 10 (11) (2013) 990–998, https://doi.org/10.1002/ppap.201300036.
[14] A. Bousquet, F. Zoubian, J. Cellier, C. Taviot-Gueho, T. Sauvage, E. Tomasella, Structural and ellipsometric study on tailored optical properties of tantalum oxynitride films deposited by reactive sputtering, J. Phys. D: Appl. Phys. 47 (47) (2014) 475201, https://doi.org/10.1088/0022-3727/47/47/475201.
[15] C. Taviot-Guého, J. Cellier, A. Bousquet, E. Tomasella, Multiphase structure of tantalum oxynitride TaOxNy thin films deposited by reactive magnetron sputtering, J. Phys. Chem. C 119 (41) (2015) 23559–23571, https://doi.org/10.1021/acs.jpcc.5b07373.
[16] S. Venkataraj, H. Kittur, R. Drese, M. Wuttig, Multi-technique characterization of tantalum oxynitride films prepared by reactive direct current magnetron sputtering, Thin Solid Films 514 (1–2) (2006) 1–9, https://doi.org/10.1016/j.tsf.2005.08.320.
[17] C. Chung, T. Chen, N. Chang, Effect of reactive gases flow ratios on the microstructure and electrical resistivity of Ta-N-O thin films by reactive co-sputtering, Thin Solid Films 519 (15) (2011) 5099–5102, https://doi.org/10.1016/j.tsf.2011.01.151.
[18] K. Sarakinos, J. Alami, S. Konstantinidis, High power pulsed magnetron sputtering: a review on scientific and engineering state of the art, Surf. Coat. Technol. 204 (11) (2010) 1661–1684, https://doi.org/10.1016/j.surfcoat.2009.11.013.
[19] A. Anders, Discharge physics of high power impulse magnetron sputtering, Surf. Coat. Technol. 205 (2011) S1–S9, https://doi.org/10.1016/j.surfcoat.2011.03.081.
[20] D. Lundin, K. Sarakinos, An introduction to thin film processing using high-power impulse magnetron sputtering, J. Mater. Res. 27 (05) (2012) 780–792, https://doi.org/10.1557/jmr.2012.8.
[21] J.T. Gudmundsson, N. Brenning, D. Lundin, U. Helmersson, High power impulse magnetron sputtering discharge, J. Vac. Sci. Technol. A: Vac. Surf. Films 30 (3) (2012) 030801, https://doi.org/10.1116/1.3691832.
[22] J. Vlček, J. Rezek, J. Houška, T. Kozák, J. Kohout, Benefits of the controlled reactive high-power impulse magnetron sputtering of stoichiometric ZrO2 films, Vacuum 114 (2015) 131–141, https://doi.org/10.1016/j.vacuum.2014.12.004.
[23] A. Belosludtsev, J. Houška, J. Vlček, S. Haviar, R. Čerstvý, J. Rezek, M. Kettner, Structure and properties of Hf-O-N films prepared by high-rate reactive HiPIMS with smoothly controlled composition, Ceram. Int. 43 (7) (2017) 5661–5667, https://doi.org/10.1016/j.ceramint.2017.01.102.
[24] J. Rezek, J. Vlček, J. Houška, R. Čerstvý, High-rate reactive high-power impulse magnetron sputtering of Ta-O-N films with tunable composition and properties, Thin Solid Films 566 (2014) 70–77, https://doi.org/10.1016/j.tsf.2014.07.033.
[25] A.S. Ferlauto, G.M. Ferreira, J.M. Pearce, C.R. Wronski, R.W. Collins, X. Deng, G. Ganguly, Analytical model for the optical functions of amorphous semiconductors from the near-infrared to ultraviolet: applications in thin film photovoltaics, J. Appl. Phys. 92 (5) (2002) 2424–2436, https://doi.org/10.1063/1.1497462.
[26] W.-J. Chun, A. Ishikawa, H. Fujisawa, T. Takata, J.N. Kondo, M. Hara, M. Kawai, Y. Matsumoto, K. Domen, Conduction and valence band positions of Ta2O5 TaON and Ta3N5by UPS and electrochemical methods, J. Phys. Chem. B 107 (8) (2003) 1798–1803, https://doi.org/10.1021/jp027593f.
[27] Y. Matsumoto, Energy positions of oxide semiconductors and photocatalysis with iron complex oxides, J. Solid State Chem. 126 (2) (1996) 227–234, https://doi.org/10.1006/jssc.1996.0333.
[28] E. Çetinörgü, B. Baloukas, O. Zabeida, J.E. Klemberg-Sapieha, L. Martinu, Mechanical and thermoelastic characteristics of optical thin films deposited by dual ion beam sputtering, Appl. Opt. 48 (23) (2009) 4536, https://doi.org/10.1364/ao.48.004536.

B

Bixbyite-Ta_2N_2O film prepared by HiPIMS and postdeposition annealing: Structure and properties

J. Čapek, Š. Batková, M. Matas, Š. Kos, T. Kozák, S. Haviar, J. Houška, J. Schusser, J. Minár, F. Dvořák, P. Zeman

Journal of Vacuum Science & Technology A 38 (2020) 033409

JVST A
Journal of Vacuum Science & Technology A

ARTICLE

avs.scitation.org/journal/jva

Bixbyite-Ta_2N_2O film prepared by HiPIMS and postdeposition annealing: Structure and properties

Cite as: J. Vac. Sci. Technol. A **38**, 033409 (2020); doi: 10.1116/6.0000066
Submitted: 1 February 2020 · Accepted: 3 April 2020 ·
Published Online: 20 April 2020

View Online

Export Citation

CrossMark

J. Čapek,[1,a)] Š. Batková,[1] M. Matas,[1] Š. Kos,[1] T. Kozák,[1] S. Haviar,[1] J. Houška,[1] J. Schusser,[2,3] J. Minár,[2] F. Dvořák,[4] and P. Zeman[1]

AFFILIATIONS

[1]Department of Physics and NTIS–European Centre of Excellence, University of West Bohemia, Univerzitní 8, 301 00 Plzeň, Czech Republic
[2]New Technologies–Research Centre, University of West Bohemia, Univerzitní 8, 301 00 Plzeň, Czech Republic
[3]Département de Physique, Université de Cergy-Pontoise, 5 mail Gay-Lussac, 95031 Cergy-Pontoise, France
[4]Center of Materials and Nanotechnologies, University of Pardubice, Studentská 95, 532 10 Pardubice, Czech Republic

Note: This paper is part of the 2020 Special Topic Collection Festschrift Honoring Dr. Steve Rossnagel.
[a)]**Electronic mail:** jcapek@kfy.zcu.cz

ABSTRACT

High-power impulse magnetron sputtering of a Ta target in precisely controlled $Ar+O_2+N_2$ gas mixtures was used to prepare amorphous N-rich tantalum oxynitride (Ta–O–N) films with a finely varied elemental composition. Postdeposition annealing of the films at 900 °C for 5 min in vacuum led to their crystallization without any significant change in the elemental composition. The authors show that this approach allows preparation of a Ta–O–N film with a dominant Ta_2N_2O phase of the bixbyite structure. As far as the authors know, this phase has been neither experimentally nor theoretically reported yet. The film exhibits semiconducting properties characterized by two electrical (indirect or selection-rule forbidden) bandgaps of about 0.2 and 1.0 eV and one optical (direct and selection-rule allowed) bandgap of 2.0 eV (suitable for visible-light absorption up to 620 nm). This observation is in good agreement with the carried out *ab initio* calculations and the experimental data obtained by soft and hard X-ray photoelectron spectroscopy. Furthermore, the optical bandgap is appropriately positioned with respect to the redox potentials for water splitting, which makes this material an interesting candidate for this application.

Published under license by AVS. https://doi.org/10.1116/6.0000066

I. INTRODUCTION

Binary films from the Ta–N system have interesting properties including high hardness,[1,2] wear[3] and corrosion[4] resistance, or photocatalytic activity.[5,6] The Ta–N system is quite complex mainly due to the occurrence of various metastable phases.[7–9] Among them, there is also a rare one that was first prepared using a CVD technique by Ganin *et al.*[10] The authors characterized this phase as a Ta_2N_3 compound with a bixbyite structure of the $Ia\bar{3}$ space group (let us denote this phase as b-Ta_2N_3 from now on). This phase was also later prepared by Salamon *et al.*[11] using magnetron sputtering followed by postdeposition annealing at 450 °C in vacuum. The authors found that the b-Ta_2N_3 films were electrically conductive. This observation was also supported by their *ab initio* calculations showing that the Fermi level is positioned in the conduction band. The calculations further predicted an optical bandgap of about 2 eV. Upon annealing above 850 °C in vacuum, the films transformed into the NaCl-type δ-TaN phase.

Adding oxygen into the Ta–N system provides a possibility to prepare Ta–O–N films that have been intensively studied in the last few years due to their promising mechanical,[12,13] electrical,[14–16] optical,[17–19] antibacterial,[20] and especially photocatalytic properties.[21–23] By far, the most studied phase in the Ta–O–N system is the monoclinic β-TaON.[24] Some of the less known phases include the monoclinic γ-TaON,[25] the tetragonal δ-TaON,[26] and the hexagonal α-TaON.[27] The hexagonal one has, however, been refuted on the basis of quantum-chemical calculations.[28]

High-power impulse magnetron sputtering (HiPIMS) is a modern physical vapor deposition technique utilizing a very high

discharge power density that is delivered to the target in short pulses (50–200 μs) at a relatively low pulse repetition frequency (50–1000 Hz) in order to avoid target overheating.[29,30] The main benefit of this technique is an enhanced dissociation and/or ionization of gas and target species. Recently, it has been demonstrated in our laboratories that controlled HiPIMS is a suitable technique for preparation of various oxynitride films with a continuously varying concentration ratio of N and O atoms and thus their properties.[31–33]

The present work follows up on our previous study[33] focusing on Ta–O–N films (prepared by HiPIMS) with continuously varying composition from tantalum oxide (Ta_2O_5) to tantalum nitride (TaN) and particularly on the annealed film with the monoclinic β-TaON phase. In the present work, our main focus is on preparation of N-rich Ta–O–N films, i.e., with a prevalent nitrogen content, by the same deposition technique. After postdeposition annealing, we identify a crystalline Ta_2N_2O phase with the bixbyite structure in a particular film (let us denote this phase as b-Ta_2N_2O from now on). As far as we know, this phase has been neither experimentally nor theoretically reported yet. Therefore, we pay great attention to optical and electrical properties of the film with the dominant b-Ta_2N_2O phase and its electronic structure in view of potential applications for water splitting.

II. EXPERIMENTAL AND METHODOLOGY

A. Film preparation

The Ta–O–N films were deposited using the same deposition system as described in Ref. 33. The base pressure before each deposition was lower than 5×10^{-5} Pa. Ar was introduced into the chamber at a flow rate of 50 sccm. The pumping speed of the turbomolecular pump was adjusted using a throttle valve to attain an Ar partial pressure of 1.000 Pa. Subsequently, a mixture of N_2 and O_2 was admitted [via individual mass-flow controllers (MFCs)] at corresponding flow rates, ϕ_{N2} and ϕ_{O2}, into the chamber. Values of ϕ_{N2} and ϕ_{O2} were regulated using MFCs controlled by a PID unit (647C, MKS Instruments) in order to keep the total pressure during the reactive deposition constant at 1.095 Pa for all depositions, while the preset nitrogen fraction in the total reactive gas flow, $f_{N2} = \phi_{N2}/(\phi_{O2} + \phi_{N2})$, was set to a constant value from a narrow range 95%–100% for a given deposition.

The magnetron (HVM Plasma Ltd.) was driven by a high-power pulsed direct-current power supply (HMP 2/1, Hüttinger Elektronik). The negative-voltage pulse duration, t_{ON}, and the pulse repetition frequency, f_r, were kept constant at 50 μs and 170 Hz, respectively. The corresponding duty cycle, t_{ON}/T, was 0.85%, where the pulse period $T = 1/f_r$.

The waveforms of the target voltage, $U_T(t)$, and discharge target current, $I_d(t)$, were recorded by a digital oscilloscope (PicoScope 6403C, Pico Technology) using voltage (TT-HV 150, Testec) and current (CT-E0.5-B, Bergoz) probes. The average discharge target power density in a pulse was evaluated as

$$P_{da} = \frac{1}{t_{ON} A_T} \int_0^{t_{ON}} U_T(t)\, I_d(t)\, dt, \qquad (1)$$

where A_T stands for the total target area ($\approx$20 cm^2 in our case). The average discharge target power density in a period, $\overline{P_d}$, was evaluated accordingly as

$$\overline{P_d} = \frac{1}{T A_T} \int_0^{T} U_T(t)\, I_d(t)\, dt. \qquad (2)$$

In this work, P_{da} and $\overline{P_d}$ values were kept constant at 1000 W/cm^2 and 10 W/cm^2, respectively.

The films were deposited onto polished and ultrasonically precleaned Si(100) or fused-silica (for measurements of electrical properties) substrates. The deposition time was 50 min. The film thickness was measured by profilometry (DEKTAK 8 Stylus Profiler, Veeco) at the film edge created by using a removable thin silicon mask on the substrate during the deposition. The deposition rate was 7.5 nm/min at $f_{N_2} = 95\%$ and gradually decreased down to 4.6 nm/min at $f_{N_2} = 100\%$.

B. Film annealing

The as-deposited films were annealed at temperatures of 800, 900, 1000, or 1100 °C for 5 or 10 min in a stainless-steel vacuum furnace of a rapid thermal processor (AS-One 100 RTP, Annealsys); heating and cooling were carried out at the same rate of 30 °C/min. The base pressure in the furnace prior to each annealing process was 1×10^{-3} Pa.

C. Film characterization and *ab initio* calculations

1. Elemental composition, microstructure, and crystal structure

The elemental composition was determined by wavelength dispersive spectroscopy (MagnaRay, Thermo Scientific) performed in a scanning electron microscope (SU-70, Hitachi) using a primary electron energy of 10 kV. The same instrument was used to obtain cross-sectional and top-view images of the films.

X-ray diffraction (XRD) measurements were carried out at room temperature using a diffractometer (Xpert PRO, PANalytical) in the Bragg–Brentano configuration with CuKα (40 kV, 40 mA) radiation. To avoid a strong reflection from the Si(100) substrate, a slightly asymmetrical diffraction geometry with an ω-offset of 1.5° was used.

2. Optical properties

The refractive index, n, and extinction coefficient, k, were determined by a variable angle spectroscopic ellipsometry instrument (J.A. Woollam Co., Inc.). The measurements were performed using angles of incidence of 65°, 70°, and 75° in reflection. The optical data were fitted for wavelength, λ, in the range of 300–2000 nm using the WVASE software. The optical model consisted of a Si substrate, a Ta–O–N layer, and a surface roughness layer. The Ta–O–N layer was represented by a sum of the Cody–Lorentz oscillator (described, e.g., in our previous work[33]) and the Drude oscillator.

3. Electrical properties

The electrical resistivity and the Hall coefficient of the films prepared on 8×8 mm^2 fused-silica substrates were measured in

Published under license by AVS.

the Van der Pauw configuration using a Hall measurement system (MMR Technologies). The measurements were carried out at a controlled temperature of the sample in the range of 90–725 K under vacuum (to prevent oxidation of the films). Gold contacts were sputter-deposited onto the corners of the square sample prior to the measurement to avoid nonohmic contacts between the film and the spring-loaded probe tips.

4. Electronic structure

The electronic structure of the investigated materials was calculated using a density-functional theory as implemented in the plane-wave self-consistent field (PWscf) code[34,35] of the Quantum ESPRESSO software package and also using the density-functional theory taking into account fully relativistic Green functions as implemented in the spin polarized relativistic Korringa–Kohn–Rostoker (SPR-KKR) code[36,37] of the Munich SPR-KKR band structure software package.

In the case of the PWscf calculations, atom cores and inner electron shells were represented by Vanderbilt-type pseudopotentials,[38] and the Kohn–Sham equations for the valence electrons were expanded in a basis of plane waves with wavefunctions and density energy cutoffs of 30 Ry and 240 Ry, respectively. The exchange and correlation term was treated using the Perdew–Burke–Ernzerhof functional.[39] The cubic periodic simulation cell of the b-Ta_2N_3 had a lattice constant, $a = 9.8205$ Å (selected based on Ref. 10) and consisted of 32 Ta and 48 N atoms in the bixbyite structure.[40] The cubic periodic simulation cell of the b-Ta_2N_2O had an experimentally (by XRD) determined $a = 9.7744$ Å and consisted of 32 Ta, 32 N, and 16 O atoms with O atoms regularly occupying one third of the anion positions, chosen as the lowest-energy set of three tested ones. For both materials, also, slightly higher and lower lattice constants were tested to confirm that the chosen ones correspond to energetic minima. The Brillouin zone was sampled with a $4 \times 4 \times 4$ Monkhorst–Pack k-point grid. After a full geometrical relaxation, the electronic density of states (EDOS), both total and projected onto individual orbitals, was calculated.

In the case of the SPR-KKR calculations, the oxygen atoms were considered as randomly distributed at the nitrogen positions in the lattice of the b-Ta_2N_2O by utilizing coherent potential, atomic sphere, and local density approximations. The cubic simulated cell of the b-Ta_2N_2O had the same value of a as in the case of PWscf calculations and consisted of 16 Ta atoms, 24 atomic positions of which 67% are occupied by nitrogen atoms and 33% by oxygen atoms, and 24 vacuum atoms.

X-ray photoelectron spectroscopy (XPS) was carried out at the I09 Diamond light source beamline equipped with a high-energy electron analyzer. The measurements were done using soft and hard X rays with a photon energy of 800 eV (an experimental resolution of 200 meV) and 3000 eV (an experimental resolution of 300 meV), respectively. The obtained spectra were normalized on the same number of counts, and the Fermi level was aligned to 0 of the energy scale at the Fermi edge at room temperature.

5. Bandgap position

The bandgap position of the selected film was determined by ultraviolet photoemission spectroscopy (UPS) performed in a UHV apparatus (ESCA 2SR, Scienta-Omicron) following the methodology described in detail in Ref. 41. UPS spectra were taken with He I (21.2 eV) UV light and recorded with a constant pass energy of 2.0 eV. The film was biased to −10 V during each measurement in order to measure the secondary electron cutoff. The film was cleaned for 15 min prior to the measurement using an ion beam of Ar clusters consisting of 1000 atoms. The energy of clusters and the sputtering current were set to 10 keV and 9 nA, respectively.

The obtained UPS spectrum of the film was first referenced to the Fermi edge, E_F, of a circular gold area with a diameter of 2 mm, which was *ex situ* sputter-deposited onto the film. Upon the determination of the cutoff of the UPS spectrum of the film, the corresponding energy position of the vacuum level, E_{vac}, was obtained by taking into account the energy of the used UV photons (21.2 eV).

III. RESULTS AND DISCUSSION

In this section, we first present the elemental composition of the prepared Ta–O–N films (Fig. 1) and the structure of the films after their annealing at 900 °C in vacuum (Fig. 2). Based on these results, we further focus our investigation on the properties of the film with the dominant b-Ta_2N_2O phase. We study the morphology of the film (Fig. 3), the temperature stability of the crystal structure (Fig. 4), optical (Fig. 5) and electrical (Fig. 6) properties of the film, and the electronic structure of the film determined by *ab initio* calculations (Fig. 7) and XPS (Fig. 8). Finally, we elaborate on a possible application of the film for photocatalytic water splitting, which also includes discussion of the bandgap position of the film with respect to the corresponding redox potentials (Fig. 9).

A. Elemental composition of Ta–O–N films

The used deposition technique allowed us to very finely control the elemental composition of the as-deposited Ta–O–N films [see Fig. 1(a)]. The nitrogen fraction in the total reactive gas flow, f_{N_2}, was precisely varied (with a minimum step of only 0.5 %) in the range of 95.0%–100.0%. Its increasing value leads to a gradual (nearly linear) substitution of O atoms by N atoms at a concurrent slight increase in the content of Ta atoms in the films. This corresponds to a gradual change in the elemental composition of the films from $Ta_{37}O_{23}N_{40}$ to $Ta_{44}O_7N_{50}$ with a typical variation step for the individual elements in the range of 1–3 at. %. Let us mention that the content of oxygen of 7 at. % at $f_{N_2} = 100\%$ is a consequence of a release of oxygen from the chamber walls during the deposition due to preceding depositions in an oxygen containing atmosphere.

The annealing of the prepared films at 900 °C for 5 min in a vacuum furnace (a base pressure of 1×10^{-3} Pa) practically did not affect their elemental composition as can be seen by comparing Figs. 1(a) and 1(b). The small variation in the values is within the error of the analysis used.

B. Crystal structure of Ta–O–N films

All the as-deposited Ta–O–N films were X-ray amorphous except for the film prepared at $f_{N_2} = 100.0\%$, which possessed a single nanocrystalline cubic TaN structure. The amorphous structure of the films was retained up to a temperature of 800 °C upon

Published under license by AVS.

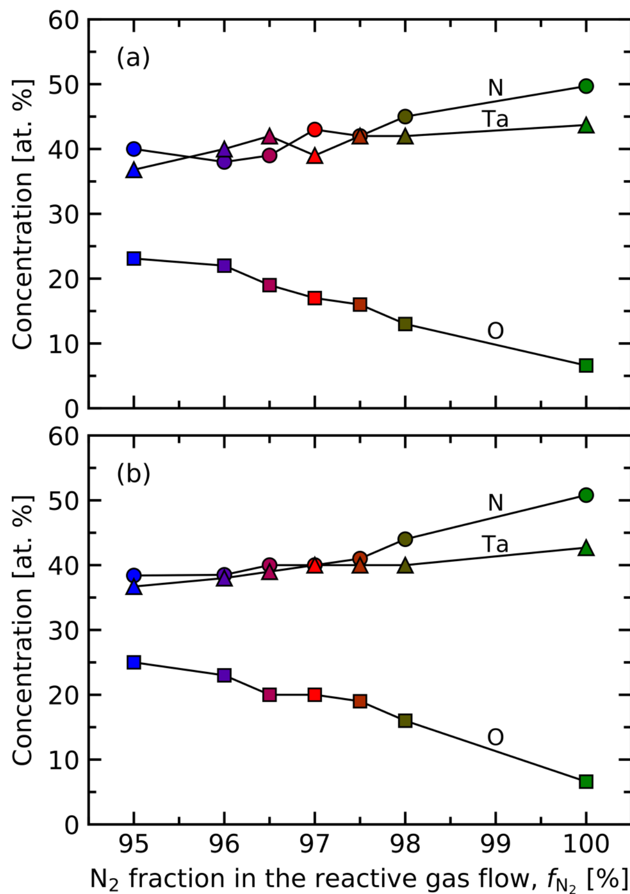

FIG. 1. Elemental composition of the Ta–O–N films after deposition (a) and after their annealing at 900 °C for 5 min in a vacuum furnace (b). The as-deposited films were prepared at various nitrogen fractions in the total reactive gas flow, f_{N_2}.

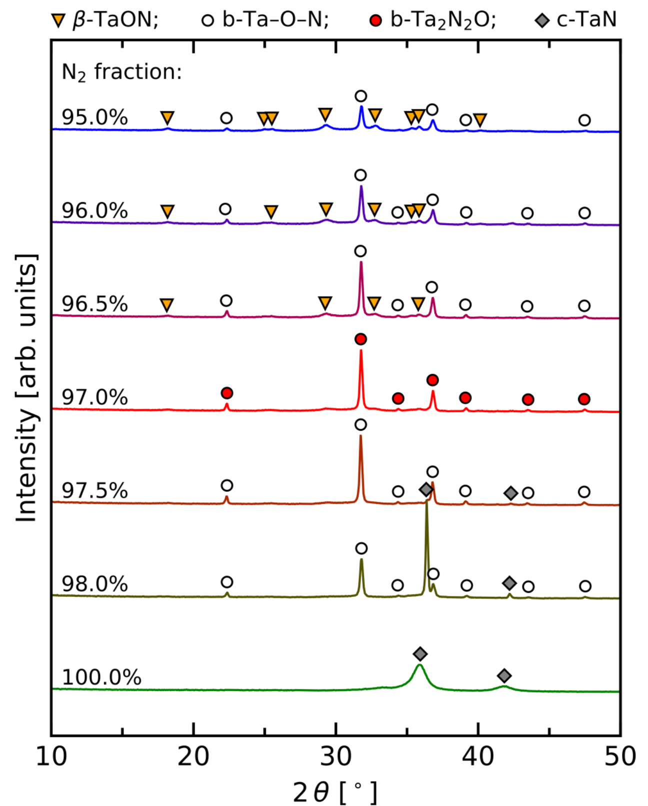

FIG. 2. XRD patterns taken from the Ta–O–N films deposited at various nitrogen fractions in the total reactive gas flow, f_{N_2}, and subsequently annealed at 900 °C in a vacuum furnace. The patterns were recorded at room temperature. The identified phases of monoclinic β-TaON, cubic bixbyite-Ta–O–N (b-Ta–O–N), cubic bixbyite-Ta_2N_2O (b-Ta_2N_2O), and cubic TaN (c-TaN) are indicated by triangles, empty circles, full circles, and diamonds, respectively.

their annealing in vacuum. Note that the corresponding XRD data showing the temperature evolution of the structures are not presented here except for the film prepared at $f_{N_2} = 97.0\%$ (Fig. 4). This film will be discussed in more detail below.

XRD patterns presented in Fig. 2 show that all the Ta–O–N films are crystalline after their annealing at 900 °C in vacuum. The films prepared at f_{N_2} in the range of 95.0%–96.5% exhibit a mixture of two phases, monoclinic β-TaON (PDF Card No. 01-083-4964) and bixbyite-Ta–O–N (b-Ta–O–N). The b-Ta–O–N phase was identified based on the work of Ganin *et al.*[10] Here, we intentionally do not specify the elemental composition in the notation of the b-Ta–O–N phase since the elemental composition discussed in Sec. III A corresponds to a mixture of two phases. This is, however, not the case for the film prepared at $f_{N_2} = 97.0\%$ because the annealing of this film leads to crystallization of a dominant bixbyite phase (with a lattice constant, $a = 9.7744$ Å). Therefore, in this case, we denote the phase as b-Ta_2N_2O based on the elemental composition of the film (i.e., 40% Ta, 40% N, and 20% O, as seen in Fig. 1). Annealing of the film prepared at $f_{N_2} = 98.0\%$ leads to crystallization of the cubic TaN phase (c-TaN, PDF Card No. 04-007-1969) along with the b-Ta–O–N phase. For $f_{N_2} = 100\%$, the film retains its single nanocrystalline cubic TaN structure without any pronounced changes after the annealing.

C. Bixbyite-Ta_2N_2O film

1. Microstructure

Despite the very high annealing temperature, the images presented in Fig. 3 indicate a crack-free surface with barely observable grains and a densified volume of the b-Ta_2N_2O film.

2. Temperature stability of the crystal structure

Figure 4(a) shows XRD patterns of four samples (from one batch) of the film prepared at $f_{N_2} = 97.0\%$ and each annealed at a different temperature in the range of 800–1100 °C for 5 min in vacuum. It is obvious that the film is amorphous up to 800 °C and crystallizes into the dominant b-Ta_2N_2O phase between 800 and

Published under license by AVS.

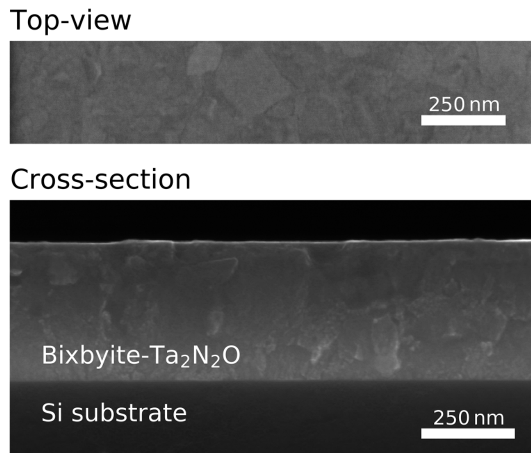

FIG. 3. Top-view and cross-sectional images of the bixbyite-Ta_2N_2O (b-Ta_2N_2O) film.

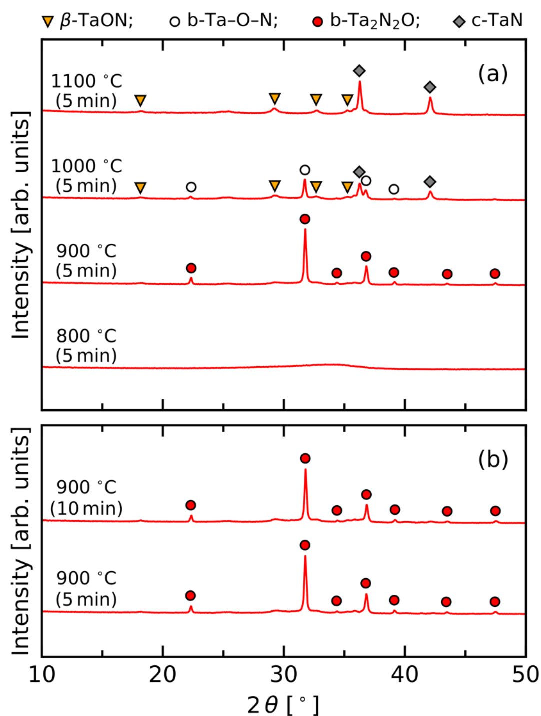

FIG. 4. XRD patterns taken from the Ta–O–N films prepared at a nitrogen fraction in the total reactive gas flow, $f_{N_2} = 97\%$, and subsequently annealed in a vacuum furnace: four samples from one batch annealed at various temperatures (800, 900, 1000, and 1100 °C) for 5 min in vacuum (a) and one sample annealed during two successive annealing cycles at 900 °C for 5 and 10 min in vacuum (b). The patterns were recorded at room temperature. The identified phases of monoclinic β-TaON, cubic bixbyite-Ta–O–N (b-Ta–O–N), cubic bixbyite-Ta_2N_2O (b-Ta_2N_2O), and cubic TaN (c-TaN) are indicated by triangles, empty circles, full circles, and diamonds, respectively.

900 °C. A further rise in the temperature up to 1000 °C destabilizes the bixbyite structure and leads to its gradual decomposition into c-TaN and β-TaON phases with increasing temperature. The dominant phase in the film after annealing to 1100 °C is c-TaN.

Figure 4(b) shows XRD patterns of one sample of the film prepared at $f_{N_2} = 97.0\%$ annealed during two successive annealing cycles at 900 °C for 5 and 10 min in vacuum. Since both patterns are practically identical, we suppose that the b-Ta_2N_2O film is fully crystalline (i.e., without any residual amorphous phase in the film) already upon 5 min of the annealing.

3. Optical properties

The b-Ta_2N_2O film was semitransparent with an optical bandgap width, E_g, of 2.0 eV, as measured by spectroscopic ellipsometry. The corresponding dispersion curves of n and k (Fig. 5) are consistent with the aforementioned optical gap: there is a strong interband absorption (as seen from the dispersion of k) and nonmonotonically changing n at $\lambda < 620$ nm and monotonically decreasing n at $\lambda > 620$ nm. Furthermore, increasing k in the long-wavelength range is a fingerprint of an absorption by free charge carriers as further discussed below.

4. Electrical properties

From the Arrhenius plot of the electrical conductivity, σ, measured using the Hall measurement system, for the b-Ta_2N_2O film (Fig. 6), one can see that the film exhibits semiconducting behavior because σ increases with increasing temperature (controlled in the range of 90–725 K).

In general, $\sigma = ne\mu$, where n is the density of charge carriers, e is the elementary charge, and μ is the mobility of charge carriers. The temperature dependence of n for an intrinsic semiconductor with a bandgap of E_g is given by

$$n \propto T^{3/2} e^{-E_g/2kT}, \tag{3}$$

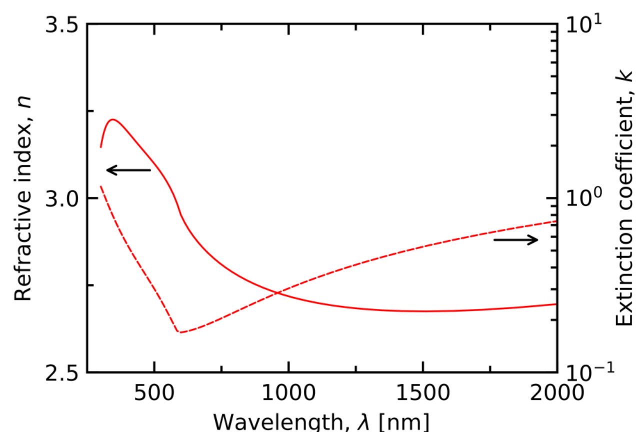

FIG. 5. Dispersion curves of refractive index, n, and extinction coefficient, k, for the bixbyite-Ta_2N_2O (b-Ta_2N_2O) film.

Published under license by AVS.

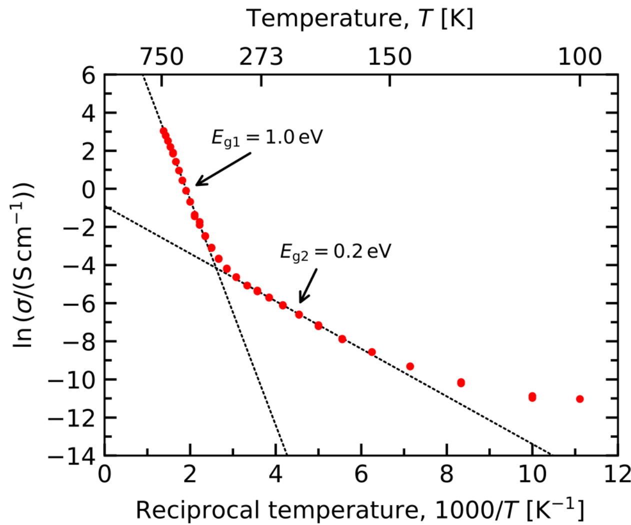

FIG. 6. Arrhenius plot for the measured conductivity of the bixbyite-Ta_2N_2O (b-Ta_2N_2O) film.

where k is the Boltzmann constant. At high temperatures, $\mu \propto T^{-3/2}$ due to dominant carrier scattering by acoustic phonons. One can then write

$$\sigma(T) \propto T^{3/2} e^{-E_g/2kT}\, T^{-3/2} = e^{-E_g/2kT}, \tag{4}$$

which implies that the E_g value can be determined directly from the linear region of the Arrhenius plot. At lower temperatures, the determination of E_g may be more difficult since the charge scattering by ionized impurities [described by a different $\mu(T)$ function] may become an important or an even dominant scattering mechanism. In such a case, $n(T)$ and $\mu(T)$ need to be measured together with $\sigma(T)$ as discussed in more detail in Ref. 42.

Unfortunately, the measured Hall coefficient for the b-Ta_2N_2O film exhibited large fluctuations over consecutive measurements. Hence, $n(T)$ and $\mu(T)$ could not be reliably evaluated separately. In this work, we thus assume that the relation $\mu \propto T^{-3/2}$ is valid for T in the range of 180–725 K, where the Arrhenius plot is characterized by two linear regions allowing us to determine E_g values from linear fits of the plot. Based on this, we can say that the b-Ta_2N_2O film is characterized by at least two electrical bandgaps of about 0.2 and 1.0 eV. Note that the temperature during the Hall probe measurements was not sufficiently high to observe the aforementioned optical bandgap of 2.0 eV.

The large difference of the electrical and optical bandgaps indicates that the former may be indirect ones or may have optical transitions forbidden by selection rules as discussed in Sec. III C 5, while the latter may be a direct one and allowed by the selection rules. The indirect or optically forbidden gap is narrow enough for thermal excitations across it, giving rise to a considerable concentration of free carriers (see the dispersion of k).

5. Bixbyite-Ta_2N_2O vs bixbyite-Ta_2N_3 films

Magnetron sputtered nitride films typically exhibit some low level of contamination by O atoms (a few at. %) owing to the fact that O_2 molecules are contained in the residual gas in the chamber and also desorb from the chamber walls during the deposition. As discussed in Sec. III A, the latter effect led to a certain oxygen concentration also in our films prepared in a pure nitrogen atmosphere. A similar effect was also responsible for a low contamination level (≈2 at. %) of oxygen in the amorphous as-deposited tantalum nitride films prepared by Salamon *et al.*[11] Annealing of these films in vacuum resulted not only in crystallization of the b-Ta_2N_3 phase (at 425 °C) but also in an increase of oxygen concentration in the films up to 6 at. % (at 750 °C).

Comparing the above-presented properties of the b-Ta_2N_2O film with those presented in Ref. 11 for the b-Ta_2N_3 film, we can identify two important roles of the enhanced concentration of oxygen (20 at. %) in our film. First, the crystallization temperature is increased from 425 °C for the b-Ta_2N_3 film to a much higher value of above 800 °C for the b-Ta_2N_2O film. This effect indicates a slower diffusion of atoms in the b-Ta_2N_2O film at a given temperature, which can be most probably attributed to an increased atomic density. This explanation is supported by a lower value of $a = 9.7744$ Å of the b-Ta_2N_2O film (see Sec. III B) as compared to $a = 9.8205$ Å of the b-Ta_2N_3 film.[10] Second, the electrical properties change from conducting for the b-Ta_2N_3 film to semiconducting for the b-Ta_2N_2O film. To further understand this effect, the electronic structure of both materials was calculated (Fig. 7), and the electronic structure of the b-Ta_2N_2O film was also experimentally measured (Fig. 8).

The electronic structure of the b-Ta_2N_3 and b-Ta_2N_2O materials was first calculated using a PWscf code. In agreement with Ref. 11, the calculated EDOS for the b-Ta_2N_3 material [Fig. 7(a)] indicates that the material exhibits a metallic character due to a nonzero population at the Fermi level, E_F. For energies below E_F, there is a region from about −2.1 to −0.3 eV where only a small number of electronic states or even no states at all (from −1.9 to −1.4 eV) are present. Due to the high nitrogen electronegativity, the occupied states below this range have most of their weight on N(p) orbitals [hybridized with Ta(d) orbitals], while the lowest unoccupied states above E_F have their weight mostly on Ta(d) orbitals. Let us highlight that optical transitions between the Ta(d) states below and above E_F (having the same parity) are forbidden by electric-dipole selection rules. Therefore, the most probable optical excitations are expected between the N(p) states at around −2.2 eV and the Ta(d) states just above E_F. Despite the metallic character of the material, a certain optical bandgap of about 2.2 eV can thus also be identified from the electronic structure.

In the case of the b-Ta_2N_2O material, the electronic structure for three different atomic configurations (with periodically substituted O for N atoms in the b-Ta_2N_3 lattice with $a = 9.7744$ Å) was investigated. The one leading to the lowest energy is considered in this work [Fig. 7(b)]. Total EDOS for the valence band exhibits a pronounced local minimum at E_F, indicating a semiconducting character of the material. The density of unoccupied Ta(d) states above E_F is significantly lower compared to the b-Ta_2N_3 material, which is compensated by new occupied states whose weight is

Published under license by AVS.

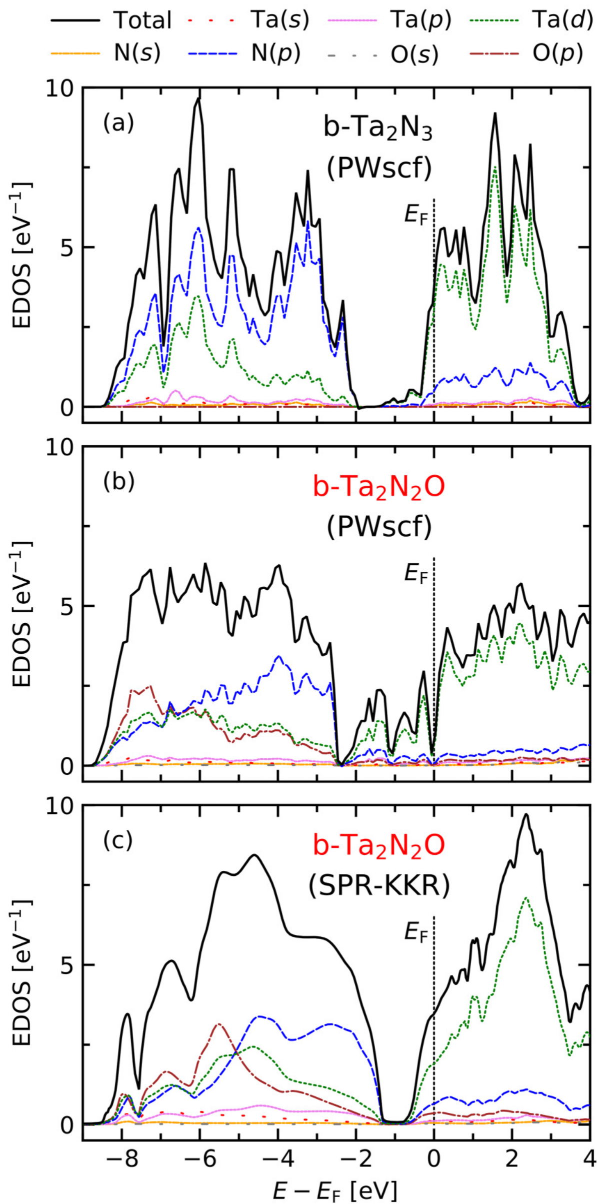

FIG. 7. EDOS for the bixbyite-Ta_2N_3 (b-Ta_2N_3) (a) and the bixbyite-Ta_2N_2O (b-Ta_2N_2O) (b) materials both calculated using the PWscf code and for the bixbyite-Ta_2N_2O (b-Ta_2N_2O) material calculated using the SPR-KKR code (c). The total EDOS (solid black line) is projected onto individual valence orbitals (dashed and dotted lines). The Fermi level is at zero energy.

mostly on Ta(d) orbitals inside the former bandgap. These states are probably responsible for the two bandgaps of about 0.2 and 1.0 eV determined from the Arrhenius plot in Sec. III C 4. In this case, the temperature-driven transitions between these emerged Ta(d) states and unoccupied Ta(d) states are allowed. However,

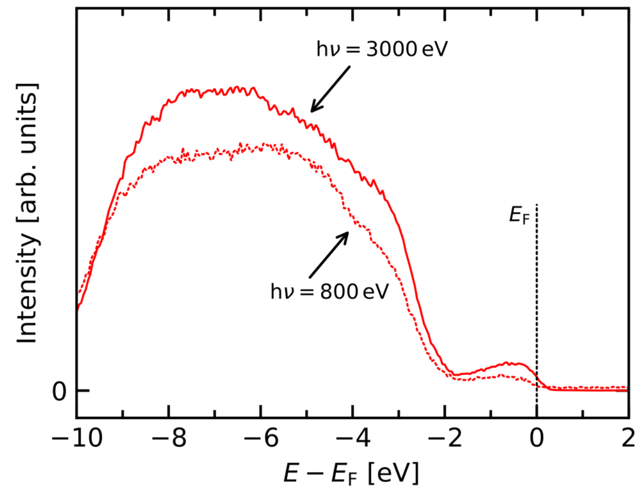

FIG. 8. XPS spectra for the bixbyite-Ta_2N_2O (b-Ta_2N_2O) film. Soft and hard X rays with photon energies of 800 and 3000 eV, respectively, were used.

optical transitions between these states are also forbidden similarly as in the case of b-Ta_2N_3. In the case of b-Ta_2N_2O, one can thus expect an optical bandgap of about 2.5 eV. This prediction is consistent with an optical bandgap width of 2.0 eV measured by spectroscopic ellipsometry (discussed in Sec. III C 3).

In order to also consider a random substitution of O for N atoms in the b-Ta_2N_3 lattice (which is not possible with the PWscf code), calculations of the electronic structure taking into account fully relativistic Green functions as implemented in the SPR-KKR code were also carried out. The calculated EDOS [Fig. 7(c)] shows that the SPR-KKR calculation leads to a similar electronic structure as in the case of the PWscf, but with only a shoulder instead of a minimum at E_F. Let us mention that a similar electronic structure would also be obtained with the PWscf code in a case where the electronic structures obtained for the three investigated atomic configurations were averaged instead of choosing the one with the minimum energy.

The measured semiconducting electrical properties of the b-Ta_2N_2O film (discussed in Sec. III C 4) indicate that there should be a pronounced local minimum in the total EDOS at an E_F level typical for semiconductors. In addition, the annealing, as a slow equilibrium process, probably helps O atoms to be periodically distributed in the material at energetically favorable positions rather than to be at random positions. For these two reasons, we believe that the electronic structure calculated using the PWscf code better describes the real electronic properties of the b-Ta_2N_2O material.

In Fig. 8, we present patterns showing an experimentally measured electronic structure of the b-Ta_2N_2O film below E_F obtained using soft and hard XPS with photon energies of 800 and 3000 eV, respectively. The higher photon energy substantially increases (about five times) the bulk sensitivity of the measurement due to a higher inelastic mean free path of the photoemitted electrons in the material. Both patterns are very similar and are characterized by a distinct peak corresponding to the valence band for energies from

Published under license by AVS.

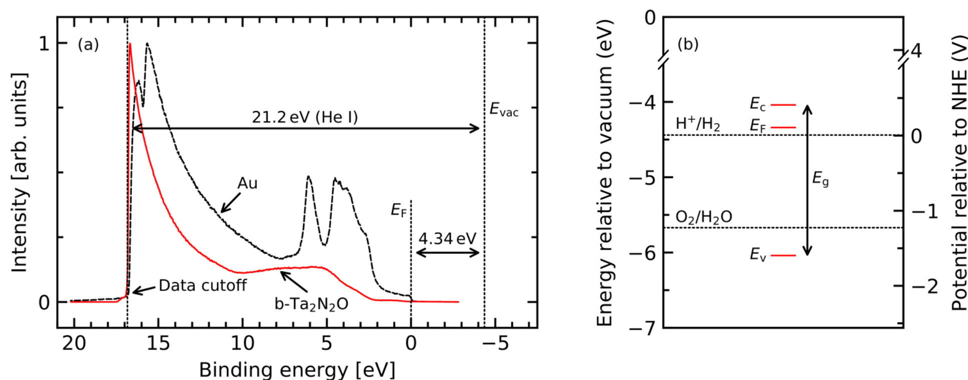

FIG. 9. Normalized UPS spectra for the bixbyite-Ta_2N_2O (b-Ta_2N_2O) film and for the gold area sputter-deposited onto the film (a) and the bandgap position for the bixbyite-Ta_2N_2O (b-Ta_2N_2O) film determined based on a combination of the UPS and spectroscopic ellipsometry results (b).

-2 to -10 eV. In addition, the energy levels below E_F (i.e., from 0 to -2 eV) predicted by the *ab initio* calculations are here observed as well.

6. Potential applications for water splitting

Materials for a successful one-step overall photocatalytic decomposition of H_2O into H_2 and O_2 under visible light must satisfy several principal requirements.[23] Among these are (i) a suitable bandgap width for visible-light absorption, (ii) an appropriate bandgap position with respect to redox potentials for water splitting, (iii) a sufficient lifetime of the photogenerated electron–hole pairs (governed by their recombination) in the material allowing charge transfer to the surface of the material where the water-splitting reactions occur, and (iv) a suppressed photocorrosion of the material.

As discussed in Sec. III C 3, the b-Ta_2N_2O film is characterized by an optical bandgap width of 2.0 eV. This facilitates visible-light absorption for wavelengths up to 620 nm and thus efficient utilization of a large fraction of the overall sunlight intensity for production of electron–hole pairs in the material.

In order to determine the position of the optical bandgap, the distance between E_F of the b-Ta_2N_2O film and the vacuum level was first determined using UPS as -4.34 eV; see Fig. 9(a). An experimental determination of the position of the bottom level of the conduction band, E_c, is difficult. In this work, we, therefore, assume (based on the works of Matsumoto[43] and Chun *et al.*[41]) that E_c of the film is not more positive than 0.3 eV with respect to E_F, which is also in a good agreement with our *ab initio* calculations discussed in Sec. III C 5. In Fig. 9(b), we, therefore, take into account the maximum possible difference, $E_c - E_F = 0.3$ eV. Furthermore, due to a large error in the determination of the top level of the valence band, E_v, from the UPS spectra, we present E_v calculated as $E_v = E_c - E_g$, where E_g was determined by the spectroscopic ellipsometry measurements (discussed in Sec. III C 3).

As one can see from Fig. 9(b), the bottom level of the conduction band and the top level of the valence band (both corresponding to the optical bandgap) are above and below the redox potentials for H^+ and O_2 production, respectively. This indicates that the b-Ta_2N_2O film exhibits a very promising position of the optical bandgap with respect to the water-splitting application. Let us here highlight that such a combination of the narrow bandgap and its position is quite unique among the candidates for the water-splitting application.[44,45]

The number, Δn, and the lifetime, τ_r, of the photoexcited charge carriers are important characteristics for all photocatalytic materials. In the case of the b-Ta_2N_2O film, τ_r requires special attention because it may be influenced by thermally excited charge carriers. As discussed in more detail in the Appendix, low- and high-injection regimes can be distinguished when considering the effect of thermally excited pairs. The regimes are separated by the condition

$$\sqrt{\frac{E}{B_r}} \approx \frac{n_0}{2}, \tag{5}$$

where E is the photoexcitation rate, B_r is the recombination rate constant, and n_0 is the equilibrium density of the thermally excited electrons. In the low-injection regime, i.e., for $\sqrt{E/B_r} \ll n_0/2$, Δn increases linearly with E and hence with the power of the exciting light, whereas τ_r is independent of this power. Both Δn and τ_r are inversely proportional to n_0. In the high-injection regime, i.e., for $\sqrt{E/B_r} \gg n_0/2$, the growth of Δn slows down from linear to the square root of the exciting-light power, and τ_r starts decaying as the inverse square root of this power. The values of Δn and τ_r are, however, independent of n_0, which makes this regime more favorable with respect to the water-splitting application.

An investigation of the photocorrosion of the b-Ta_2N_2O film is beyond the scope of this paper, but it is definitely an important topic for a further work since generally oxynitride materials may be thermodynamically unstable in an aqueous solution and thus oxidized by the holes under illumination.[46]

IV. CONCLUSIONS

In this work, we investigated properties of crystalline N-rich Ta–O–N films with a finely varied elemental composition. The films were prepared by utilizing high-power impulse magnetron sputtering of a Ta target in precisely controlled $Ar+O_2+N_2$ gas mixtures followed by postdeposition annealing at 900 °C for 5 min in vacuum.

Published under license by AVS.

We showed that the deposition at an optimum gas mixture composition led to preparation of the Ta_2N_2O film exhibiting the dominant bixbyite structure. As far as we know, this phase has been neither experimentally nor theoretically reported yet. The film was semitransparent with an optical bandgap width of 2.0 eV as measured by spectroscopic ellipsometry. Measurements of the electrical conductivity as a function of temperature further showed a semiconducting dependence characterized by two electrical bandgaps of about 0.2 and 1.0 eV. The carried out *ab initio* calculations indicated that these two bandgaps are associated with a negligible probability of excitations due to a photon absorption.

We also discussed the potential of this material for water splitting. Its optical bandgap of 2.0 eV is suitable for utilization of a large fraction of the visible light (up to 620 nm) for generation of electron–hole pairs required for the process. Furthermore, the bandgap position is quite unique with respect to the redox potentials for H^+ and O_2 production. In addition, the possible effect of thermally excited charge carriers (due to the narrow electrical bandgaps) on the recombination of the photogenerated charge carriers was thoroughly discussed. However, further experiments such as photocatalytic activities and photocorrosion tests need to be carried out to make the discussion conclusive.

ACKNOWLEDGMENTS

The main part of this work was supported by the Czech Science Foundation under Project No. 19-13174S. The calculations of the electron density of states using the SPR-KKR package and hard X-ray photoelectron spectroscopy analyses (carried out by J. Schusser and J. Minár) were supported within the CEDAMNF project financed by the Ministry of Education, Youth, and Sports of Czech Republic (Project No. CZ.02.1.01/0.0/0.0/15.003/0000358). Computational resources were provided by the National Grid Infrastructure MetaCentrum (Czech Republic) through Project CESNET (No. LM2015042). The ultraviolet photoelectron spectroscopy analyses (carried out by F. Dvořák) were supported from the European Regional Development Fund-Project "Modernization and upgrade of the CEMNAT" (No. CZ.02.1.01/0.0/0.0/16_013/0001829). The authors further wish to thank M. Kotrlová for the annealing of the films and R. Čerstvý for carrying out the XRD analysis of the films.

APPENDIX: EFFECT OF THERMALLY EXCITED ELECTRON–HOLE PAIRS ON THE LIFETIME OF THE PHOTOGENERATED ONES

Denoting the equilibrium density of the thermally excited electrons and holes as n_0 and p_0, respectively, and the excess density of electrons and holes due to photoexcitations as Δn and Δp, respectively, the net recombination rate is

$$B_r \Delta p(n_0 + \Delta n), \tag{A1}$$

where B_r is the recombination rate constant with the dimension of inverse time times inverse density, and we have neglected the recombination of electrons with the thermally excited holes because the thermally excited holes have predominantly the same d-symmetry as the thermally excited electrons, and thus, their radiative recombination is dipole-forbidden. Using the neutrality condition $\Delta n = \Delta p$, the equation for the time evolution of Δn is

$$\frac{d\Delta n}{dt} = -B_r \Delta n(n_0 + \Delta n) + E, \tag{A2}$$

where E is the photoexcitation rate with the dimension of inverse time times density. In the steady state,

$$\frac{d\Delta n}{dt} = 0; \tag{A3}$$

therefore, the equation for the time evolution becomes a quadratic equation for the steady-state value of Δn whose positive root is

$$\Delta n = \sqrt{\frac{E}{B_r} + \left(\frac{n_0}{2}\right)^2} - \frac{n_0}{2}. \tag{A4}$$

This formula shows that Δn has two regimes[47] separated by

$$\sqrt{\frac{E}{B_r}} \approx \frac{n_0}{2} \tag{A5}$$

consistently with the dimensional analysis, showing that E/B_r has the dimension of density squared. In the low-injection regime,

$$\sqrt{\frac{E}{B_r}} \ll \frac{n_0}{2}, \tag{A6}$$

we expand the square root to the first order in $E/(n_0^2 B_r)$,

$$\Delta n = \frac{n_0}{2}\left(\sqrt{1 + \frac{4E}{n_0^2 B_r}} - 1\right) \approx \frac{E}{n_0 B_r}, \tag{A7}$$

whereas in the high-injection regime,

$$\sqrt{\frac{E}{B_r}} \gg \frac{n_0}{2}, \tag{A8}$$

we neglect n_0^2 compared to E/B_r and get

$$\Delta n \approx \sqrt{\frac{E}{B_r}}. \tag{A9}$$

The radiative lifetime τ_r is given by[47]

$$\tau_r = \frac{\Delta n}{-\frac{d\Delta n}{dt}\big|_{E=0}} = \frac{1}{B_r(n_0 + \Delta n)} \tag{A10}$$

and is

$$\tau_r \approx \frac{1}{B_r n_0} \tag{A11}$$

Published under license by AVS.

in the low-injection regime and

$$\tau_r \approx \frac{1}{B_r\sqrt{\frac{E}{B_r}}} = \frac{1}{\sqrt{EB_r}} \tag{A12}$$

in the high-injection regime consistently with the dimensional analysis, showing that EB_r has a dimension of inverse time squared.

REFERENCES

[1] A. Zaman and E. Meletis, Coatings **7**, 209 (2017).
[2] C. Koller, H. Marihart, H. Bolvardi, S. Kolozsvári, and P. Mayrhofer, Surf. Coat. Technol. **347**, 304 (2018).
[3] S. Kim and B. Cha, Thin Solid Films **475**, 202 (2005).
[4] M. Alishahi, F. Mahboubi, S. M. Mousavi Khoie, M. Aparicio, E. Lopez-Elvira, J. Méndez, and R. Gago, RSC Adv. **6**, 89061 (2016).
[5] Y. He, R. Chen, W. Fa, B. Zhang, and D. Wang, J. Chem. Phys. **151**, 130902 (2019).
[6] S. Khan, M. J. M. Zapata, M. B. Pereira, R. V. Gonçalves, L. Strizik, J. Dupont, M. J. L. Santos, and S. R. Teixeira, Phys. Chem. Chem. Phys. **17**, 23952 (2015).
[7] N. Terao, Jpn. J. Appl. Phys. **10**, 248 (1971).
[8] C.-S. Shin, Y.-W. Kim, D. Gall, J. Greene, and I. Petrov, Thin Solid Films **402**, 172 (2002).
[9] C. Stampfl and A. J. Freeman, Phys. Rev. B **71**, 024111 (2005).
[10] A. Y. Ganin, L. Kienle, and G. V. Vajenine, Eur. J. Inorg. Chem. **2004**, 3233 (2004).
[11] K. Salamon, M. Očko, N. Radić, I. Bogdanović Radović, V. Despoja, and S. Bernstorff, J. Alloys Compd. **682**, 98 (2016).
[12] H. Le Dréo, O. Banakh, H. Keppner, P.-A. Steinmann, D. Briand, and N. de Rooij, Thin Solid Films **515**, 952 (2006).
[13] D. Cristea, A. Crisan, D. Munteanu, M. Apreutesei, M. Costa, and L. Cunha, Surf. Coat. Technol. **258**, 587 (2014).
[14] C. Chung, T. Chen, and N. Chang, Thin Solid Films **519**, 5099 (2011).
[15] M.-C. Chen *et al.*, Thin Solid Films **528**, 224 (2013).
[16] D. Cristea *et al.*, Appl. Surf. Sci. **354**, 298 (2015).
[17] F. Zoubian, E. Tomasella, A. Bousquet, T. Sauvage, and C. Eypert, Adv. Mater. Res. **324**, 73 (2011).
[18] A. Bousquet, F. Zoubian, J. Cellier, C. Taviot-Gueho, T. Sauvage, and E. Tomasella, J. Phys. D: Appl. Phys. **47**, 475201 (2014).
[19] K. Salamon, M. Mičetić, J. Sancho-Parramon, I. Bogdanović Radović, Z. Siketić, I. Šarić, M. Petravić, and S. Bernstorff, J. Phys. D: Appl. Phys. **52**, 305304 (2019).
[20] D. Cristea, L. Cunha, C. Gabor, I. Ghiuta, C. Croitoru, A. Marin, L. Velicu, A. Besleaga, and B. Vasile, Nanomaterials **9**, 476 (2019).
[21] P. Zhang, J. Zhang, and J. Gong, Chem. Soc. Rev. **43**, 4395 (2014).
[22] T. Takata, C. Pan, and K. Domen, ChemElectroChem **3**, 31 (2016).
[23] Z. Wang, C. Li, and K. Domen, Chem. Soc. Rev. **48**, 2109 (2019).
[24] G. Brauer and J. R. Weidlein, Angew. Chem. Int. Ed. Engl. **4**, 875 (1965).
[25] H. Schilling, A. Stork, E. Irran, H. Wolff, T. Bredow, R. Dronskowski, and M. Lerch, Angew. Chem. Int. Ed. **46**, 2931 (2007).
[26] T. Lüdtke, A. Schmidt, C. Göbel, A. Fischer, N. Becker, C. Reimann, T. Bredow, R. Dronskowski, and M. Lerch, Inorg. Chem. **53**, 11691 (2014).
[27] Y. A. Buslaev, M. A. Glushova, M. M. Ershova, and E. M. Shustorovich, Neorg. Mater. **2**, 2120 (1966).
[28] M.-W. Lumey and R. Dronskowski, Z. Anorg. Allg. Chem. **629**, 2173 (2003).
[29] C.-L. Chang and Y.-W. Chen, Surf. Coat. Technol. **205**, S1 (2010).
[30] D. Lundin and K. Sarakinos, J. Mater. Res. **27**, 780 (2012).
[31] J. Rezek, J. Vlček, J. Houška, and R. Čerstvý, Thin Solid Films **566**, 70 (2014).
[32] A. Belosludtsev, J. Houška, J. Vlček, S. Haviar, R. Čerstvý, J. Rezek, and M. Kettner, Ceram. Int. **43**, 5661 (2017).
[33] J. Čapek, Š. Batková, S. Haviar, J. Houška, R. Čerstvý, and P. Zeman, Ceram. Int. **45**, 9454 (2019).
[34] P. Giannozzi *et al.*, J. Phys.: Condens. Matter **21**, 395502 (2009).
[35] P. Giannozzi *et al.*, J. Phys.: Condens. Matter **29**, 465901 (2017).
[36] H. Ebert, D. Ködderitzsch, and J. Minár, Rep. Prog. Phys. **74**, 096501 (2011).
[37] J. Braun, J. Minár, and H. Ebert, Phys. Rep. **740**, 1 (2018).
[38] K. Laasonen, R. Car, C. Lee, and D. Vanderbilt, Phys. Rev. B **43**, 6796 (1991).
[39] J. P. Perdew, K. Burke, and M. Ernzerhof, Phys. Rev. Lett. **77**, 3865 (1996).
[40] L. Pauling and M. D. Shappell, Z. Kristallogr. Cryst. Mater. **75**, 128 (1930).
[41] W.-J. Chun, A. Ishikawa, H. Fujisawa, T. Takata, J. N. Kondo, M. Hara, M. Kawai, Y. Matsumoto, and K. Domen, J. Phys. Chem. B **107**, 1798 (2003).
[42] S. M. Sze, *Physics of Semiconductor Devices* (Wiley, New York, 1981).
[43] Y. Matsumoto, J. Solid State Chem. **126**, 227 (1996).
[44] A. Kudo and Y. Miseki, Chem. Soc. Rev. **38**, 253 (2009).
[45] N. Fajrina and M. Tahir, Int. J. Hydrogen Energy **44**, 540 (2019).
[46] S. Chen and L.-W. Wang, Chem. Mater. **24**, 3659 (2012).
[47] S. S. Li, *Semiconductor Physical Electronics* (Springer, New York, 2007), p. 140.

Published under license by AVS.

C

Effect of positive pulse voltage in bipolar reactive HiPIMS on crystal structure, microstructure and mechanical properties of CrN films

Š. Batková, J. Čapek, J. Rezek, R. Čerstvý, P. Zeman

Surface & Coatings Technology 393 (2020) 125773

Surface & Coatings Technology 393 (2020) 125773

Contents lists available at ScienceDirect

Surface & Coatings Technology

journal homepage: www.elsevier.com/locate/surfcoat

Effect of positive pulse voltage in bipolar reactive HiPIMS on crystal structure, microstructure and mechanical properties of CrN films

Š. Batková, J. Čapek*, J. Rezek, R. Čerstvý, P. Zeman

Department of Physics and NTIS - European Centre of Excellence, University of West Bohemia, Univerzitní 8, 306 14 Plzeň, Czech Republic

ARTICLE INFO

Keywords:
Bipolar reactive HiPIMS
Floating substrate holder
Grounded substrate holder
DC biased substrate holder
CrN films
Microstructure

ABSTRACT

CrN films were prepared using three different configurations of the HiPIMS discharge mode and the substrate holder potential. We investigate the effect of a positive pulse voltage (30–400 V) in bipolar HiPIMS on the crystal structure, microstructure and resulting mechanical properties of the films, and compare it to the effect of a standard DC bias voltage applied to the substrate holder in unipolar HiPIMS. We find that when the substrate holder is at a floating potential, its charging causes the loss of the plasma-substrate potential difference, necessary for ion acceleration, and no obvious evolution is thus observed with increasing positive pulse voltage. However, when the substrate holder is grounded, the effect of the positive pulse voltage is apparent and different from the effect of the DC bias substrate voltage. That is mainly due to differences in energies delivered into the growing film by bombarding ions. Films prepared using bipolar HiPIMS at a positive pulse voltage of 90 and 120 V exhibit the most interesting properties, namely high hardness (23.5 and 23.1 GPa, respectively) at a relatively low residual compressive stress (1.7 and 1.5 GPa, respectively). The results indicate that as long as the growing film is conductively connected with the ground, bipolar HiPIMS is a suitable method to tailor and improve the film properties.

1. Introduction

Transition metal nitrides (e.g., CrN, TiN, ZrN) are very well known for having excellent mechanical properties, such as high hardness and wear resistance, which makes them ideal as hard protective coatings for cutting and forming tools, engine parts and other mechanical components [1–4].

The mechanical properties mainly depend on the microstructure (e.g. density, grain size), crystal structure and residual stress of the film. The evolution of these characteristics is directly related to the degree of mobility of the adatoms on the surface of the growing film. In magnetron sputtering, a number of parameters can be varied to change the deposition conditions and thus the properties of the growing film. Very often, a bias voltage is applied to the substrates to induce ion bombardment, which enhances the adatoms' mobility and promotes densification of the film [5–8]. The induced changes in the structure of the film are then governed by the energy and flux of the particles bombarding the film surface during the growth.

The introduction of high-power impulse magnetron sputtering (HiPIMS) has brought further possibilities of controlling the deposition process. In HiPIMS, the power density in a pulse exceeds the average power density in a period usually by two orders of magnitude, resulting in high fraction of ionized species of both the working gas and the target material, and broadened ion energy distribution function [9–12]. This leads to an enhanced ion bombardment of the growing film even without the application of a substrate bias voltage. However, a substrate bias voltage might still be necessary to control the energy of the high amount of low-energy thermalized ions [13].

Recently, bipolar HiPIMS, where the main negative voltage pulse is followed by a positive one, has been suggested to be used instead of a substrate bias voltage, particularly when a DC substrate bias voltage is ineffective. The idea is based on “plasma biasing”, where instead of decreasing the substrate potential, the plasma potential is increased to create the plasma-substrate potential difference necessary for ion acceleration towards the substrate [14]. In a number of works, energy-resolved mass spectrometry has been employed to investigate ion energy distribution functions (IEDFs). These works reveal a high-energy ion peak corresponding to the applied positive pulse voltage and suggest that by changing the positive pulse voltage, great control over the ion energies can be achieved [15–20]. However, it is important to take into consideration that all these data are acquired using a mass spectrometer with a grounded orifice and one needs to be careful in generalizing the results.

In this work, we investigate the possibility of using bipolar reactive

* Corresponding author.
E-mail address: jcapek@kfy.zcu.cz (J. Čapek).

https://doi.org/10.1016/j.surfcoat.2020.125773
Received 15 January 2020; Received in revised form 27 March 2020; Accepted 11 April 2020
Available online 13 April 2020
0257-8972/ © 2020 Elsevier B.V. All rights reserved.

HiPIMS to control the crystal structure, microstructure and mechanical properties of CrN films, representative of fcc transition metal nitrides, with focus on the effect of the substrate holder potential during the deposition. We compare three different configurations of the discharge mode and the substrate holder potential: bipolar HiPIMS with a floating substrate holder, bipolar HiPIMS with a grounded substrate holder and unipolar HiPIMS with a DC biased substrate holder.

2. Experimental details

The CrN films were deposited by reactive HiPIMS in a cylindrical vacuum chamber (506 mm in diameter and 522 mm in height), pumped by a diffusion pump to a base pressure of 2×10^{-3} Pa. The unbalanced magnetron was equipped with a circular Cr target (99.95% purity, 100 mm in diameter, 6 mm in thickness).

Argon was introduced into the chamber at a flow rate of 14 sccm and the pressure was set to 0.8 Pa using a throttle valve between the chamber and the diffusion pump. Nitrogen was then admitted into the chamber and the flow rate was regulated by a PID unit (647C, MKS Instruments) to keep the total pressure constant at 1.4 Pa.

The films were deposited onto polished and ultrasonically cleaned Si (100) and glass substrates. The substrates were placed at a distance of 100 mm from the target and ohmically heated to 350 °C during deposition.

The magnetron was driven by a high-power pulsed direct current power supply (SIPP2000USB, Melec GmbH). The discharge was operated either in a unipolar HiPIMS mode or a bipolar HiPIMS mode. The negative voltage pulse length, t_{ON}, was always set to 100 μs and the repetition frequency, f, to 100 Hz. The corresponding duty cycle, t_{ON}/T, was 1%, where $T = 1/f$. In bipolar HiPIMS, the positive voltage pulse length was 60 μs with a delay of 20 μs after the negative pulse. The positive voltages ranged from 30 to 400 V. The waveforms of the target voltage, $U_t(t)$, substrate holder potential, $U_s(t)$, target current, $I_t(t)$, and substrate holder current, $I_s(t)$, were recorded using a digital oscilloscope (PicoScope 5444D, Pico Technology). The average discharge target power density in a period was calculated as:

$$\overline{P_t} = \frac{1}{TA_t} \int U_t(t) I_t(t) \mathrm{d}t, \qquad (1)$$

where A_t stands for the total target area (78.5 cm^2 in our case) and was kept at 10 W/cm^2. The average substrate holder power density in a period was calculated as:

$$\overline{P_s} = \frac{1}{T} \int P_s(t) \mathrm{d}t = \frac{1}{TA_s} \int U_{ps}(t) I_s(t) \mathrm{d}t, \qquad (2)$$

where A_s stands for the total substrate holder area facing the target (95 cm^2 in our case) and $U_{ps}(t)$ represents the plasma-substrate potential difference, $U_p(t) - U_s(t)$, where $U_p(t)$ is the plasma potential. When the substrate holder was at a floating potential, $U_f(t)$, then $I_s(t) = 0$ and $\overline{P_s}$ was thus not calculated. When a DC bias voltage was applied to the substrate holder in the unipolar HiPIMS mode, $U_p(t) \approx 0$ and thus $U_{ps}(t)$ can be approximated as: $U_{ps}(t) \approx |U_s(t)|$. In the bipolar HiPIMS mode with a grounded substrate holder during the positive voltage pulse, $U_p(t) \approx U_t(t)$, $U_s(t) = 0$ and thus $U_{ps}(t)$ can be here approximated as: $U_{ps}(t) \approx U_t(t)$. The $U_p(t) \approx U_t(t)$ approximation is based on our observation that during the positive pulse, $U_p(t)$ is lifted to values within several volts of $U_t(t)$. To support this, we present $U_p(t)$ and $U_f(t)$ during the positive pulse in Fig. 1. Both potentials were measured using a Langmuir probe in a similar deposition system at similar discharge conditions, namely at a positive voltage pulse of 50 μs (following a negative pulse of 100 μs and a delay of 20 μs) and at a distance of 100 mm from the target. Therefore, we expect a similar behavior of both potentials in this work.

The estimated energy delivered into the growing film by bombarding ions (assuming a negligible contribution of the secondary electrons to the measured current) per cm^3 was calculated as [21]:

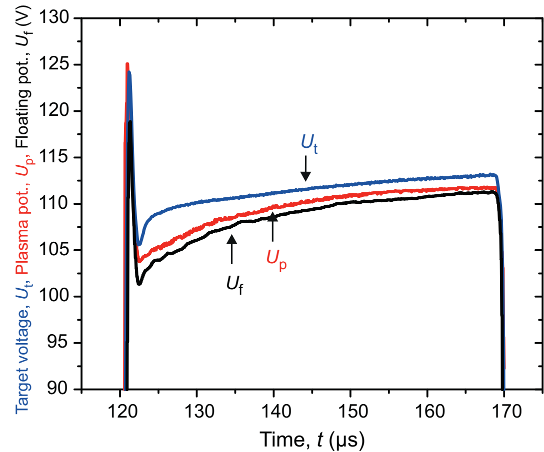

Fig. 1. Example of a measurement of the target voltage, $U_t(t)$, plasma potential, $U_p(t)$, and floating potential, $U_f(t)$, during a positive pulse. The potentials were measured using a Langmuir probe in a similar deposition system at similar discharge conditions as in this work, namely at a positive voltage pulse of 50 μs (following a negative pulse of 100 μs and a delay of 20 μs) and at a distance of 100 mm from the target.

$$E_{bi} = \frac{\overline{P_s}}{a_D}, \qquad (3)$$

where a_D stands for the deposition rate (calculated as the film thickness divided by the deposition time). The deposition time was varied depending on the deposition rate, in order to keep the thickness of all films at approx. 1 μm.

The elemental composition was measured using energy dispersive X-ray spectroscopy (UltraDry, Thermo Scientific) performed in a scanning electron microscope (SU-70, Hitachi). The same instrument was used to obtain cross-sectional and top-view images of the films.

The crystal structure was studied by X-ray diffraction using a diffractometer (Xpert PRO, PANalytical) in the Bragg-Brentano configuration with CuKα (40 kV, 40 mA) radiation. PDF Card No. 04-004-6868 was used to identify the diffraction peaks.

The residual stress was evaluated from the curvature of a Si substrate measured by a profilometer (DEKTAK 8 Stylus Profiler, Veeco) and using a modified Stoney's formula. The hardness was measured by a nanoindenter (TI 950 Triboindenter, Hysitron) equipped with a Berkovich-type diamond tip. For each film, 16 indents were made at a load of 5 mN and the obtained data were averaged. The surface roughness and morphology were determined by atomic force microscopy using a microscope (SmartSPM, AIST-NT) with a silicon tip (nominal radius below 10 nm) operating in the semicontact mode. The average roughness of the surface, R_a, was computed from a randomly selected square area of 5×5 μm^2.

3. Results and discussion

3.1. Discharge conditions

The CrN films in this work were prepared so that they could be divided into three series based on the configuration of the discharge mode and the substrate holder potential: bipolar HiPIMS with a floating substrate holder, bipolar HiPIMS with a grounded substrate holder and unipolar HiPIMS with a DC biased substrate holder. Fig. 2 shows an example of the recorded waveforms of the target voltage, $U_t(t)$, target current density, $J_t(t) = I_t(t)/A_t$, substrate holder potential, $U_s(t)$, and the calculated waveforms of the substrate holder power density, $P_s(t)$, for comparable conditions (i.e., for both a positive pulse voltage and a negative DC substrate bias voltage of 400 V). Values of the average substrate holder power density, the deposition rate and the estimated

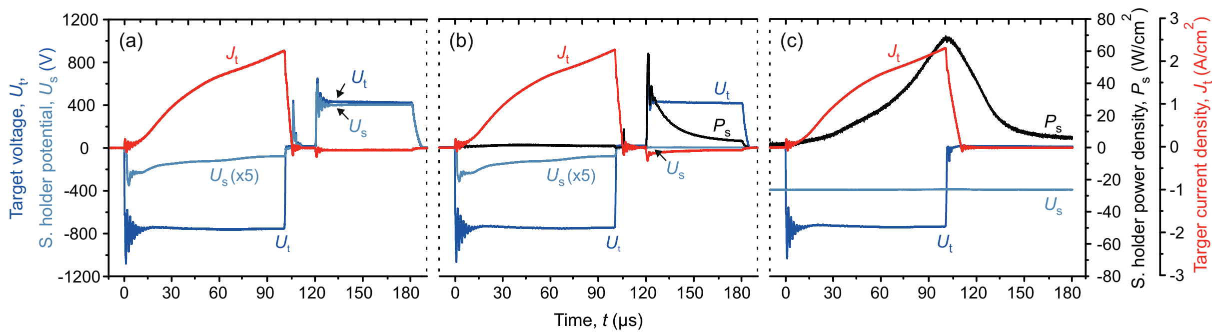

Fig. 2. Waveforms of the target voltage, $U_t(t)$, target current density, $J_t(t)$, substrate holder potential, $U_s(t)$, and substrate holder power density, $P_s(t)$, for: bipolar HiPIMS (positive pulse voltage of 400 V) with the substrate holder at a floating potential (a), bipolar HiPIMS (positive pulse voltage of 400 V) with the substrate holder grounded with a diode (b) and unipolar HiPIMS with the substrate holder biased (DC bias voltage of −400 V) (c). The substrate holder potential signal is multiplied 5 times for the duration of the negative pulse of the bipolar HiPIMS discharge.

Table 1
The average substrate holder power density, $\overline{P_s}$, the deposition rate, a_D, and the estimated energy delivered into the growing film by bombarding ions per cm^3, $E_{bi} = \overline{P_s}/a_D$, for different applied voltage values.

U_t (V) or $-U_s$ (V)		30	60	90	120	200	400
$\overline{P_s}$ (mW/cm^2)	Bipolar HiPIMS (grounded substrate holder)	4	9	13	19	33	73
	Unipolar HiPIMS (DC biased substrate holder)	22	63	96	129	227	456
a_D (nm/min)	Bipolar HiPIMS (grounded substrate holder)	55	55	55	55	53	49
	Unipolar HiPIMS (DC biased substrate holder)	52	53	49	47	37	24
E_{bi} (kJ/cm^3)	Bipolar HiPIMS (grounded substrate holder)	44	99	143	207	374	903
	Unipolar HiPIMS (DC biased substrate holder)	254	720	1170	1659	3671	11643

energy delivered into the growing film by bombarding ions per cm^3 are summarized in Table 1 for further discussion.

The characteristics of the main HiPIMS negative voltage pulse were the same in all three cases, with the applied target voltage constant after the initial oscillation and the target current continuously rising and not reaching saturation before the end of the pulse. In the bipolar HiPIMS mode, a positive voltage pulse was applied to the target as soon as possible after the negative pulse. However, due to the construction of the HiPIMS power supply, there is a minimum required delay of 20 μs. This delay contains a short positive voltage overshoot, preceding the onset of the positive voltage pulse. When the substrate holder is floating, the overshoot is more pronounced because the substrate holder represents a smaller load for the power supply. However, the overshoot never exceeds the value of the positive pulse voltage.

In the first series of the films, the discharge was sustained in the bipolar HiPIMS mode with the substrate holder at a floating potential, $U_f(t)$, simulating a deposition of non-conductive materials or a deposition onto non-conductive substrates. As can be seen in Fig. 2a, during the positive pulse, $U_s(t) \equiv U_f(t)$ approaches $U_t(t)$. This is a consequence of charging of the substrate holder by the impacting ions due to a lifted plasma potential, $U_p(t)$. As shown in Fig. 1 and also reported by Karkari et al. [22], $U_p(t)$ remains within several volts of the potential of the most positive electrode (the target cathode in this case) and $U_s(t) \equiv U_f(t)$ thus quickly rises up to a similar level. As a result, the plasma-substrate potential difference, $U_{ps}(t)$, is lost.

The second series of the films was prepared in the bipolar HiPIMS mode with a diode placed between the substrate holder and the ground. The use of a diode results in a grounded substrate holder (and $U_{ps}(t)$ almost equal to $U_t(t)$) only during the positive pulse and a floating substrate holder during the negative pulse (see Fig. 2b). In this way, the conditions remain the same during the negative pulse (high electron currents and their possible effects are thus eliminated) and the effect of the positive pulse only can be investigated.

The third series of the films was prepared in the unipolar HiPIMS mode with a negative DC bias voltage applied to the substrate holder (see Fig. 2c). It is worth noting that the substrate bias voltage does not decrease in absolute value with the incoming ion current during the negative voltage pulse and remains constant. That is thanks to a very low internal resistance of the used DC power supply.

3.2. Elemental composition

The chromium and nitrogen contents in all prepared films were measured to be 50 ± 2 at.% and are summarized in Table 2. All films can therefore be considered stoichiometric and the elemental composition does not enter into further discussion.

3.3. Crystal structure and microstructure

The evolution of the crystal structure, represented by XRD patterns

Table 2
Chromium and nitrogen contents in all prepared films.

U_t (V)		0	130	260	400
Bipolar HiPIMS (floating substrate holder)	Cr (at.%)	49	51	51	50
	N (at.%)	51	49	49	50

U_t (V) or $-U_s$ (V)		0	30	60	90	120	200	400
Bipolar HiPIMS (grounded substrate holder)	Cr (at.%)	52	50	50	48	48	51	52
	N (at.%)	48	50	50	52	52	49	48
Unipolar HiPIMS (DC biased substrate holder)	Cr (at.%)	52	49	51	51	50	52	52
	N (at.%)	48	51	49	49	50	48	48

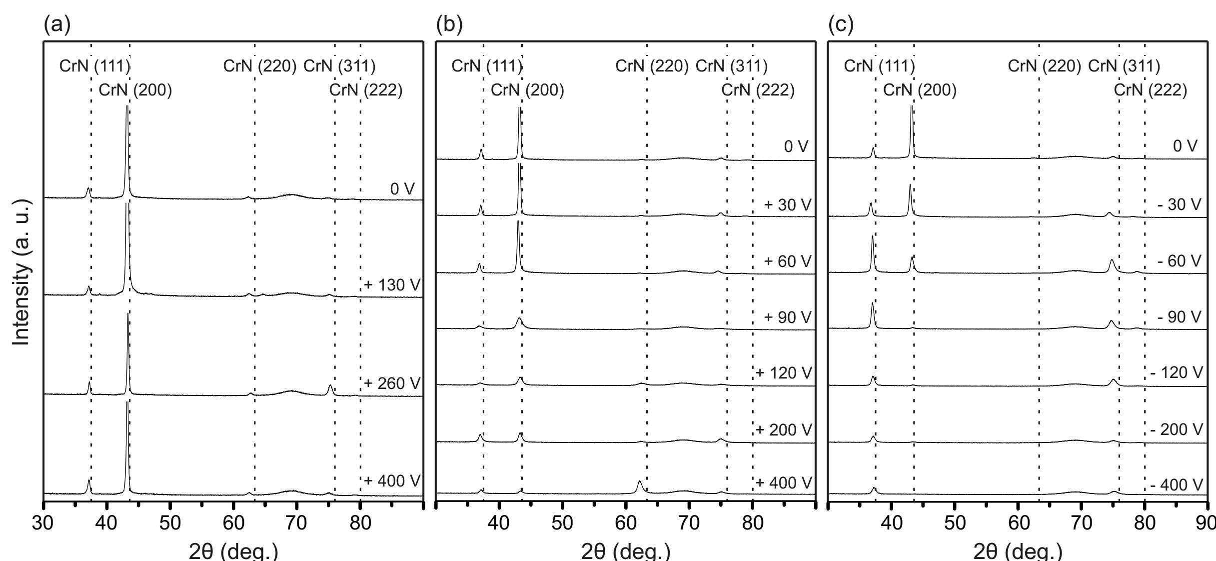

Fig. 3. XRD patterns of the CrN films prepared by bipolar HiPIMS with a floating substrate holder (a), bipolar HiPIMS with a grounded substrate holder (b) and unipolar HiPIMS with a DC biased substrate holder (c) at different applied voltage values. The film prepared at 0 V is shared for (b) and (c). The vertical lines correspond to the XRD standard (PDF Card No. 04-004-6868).

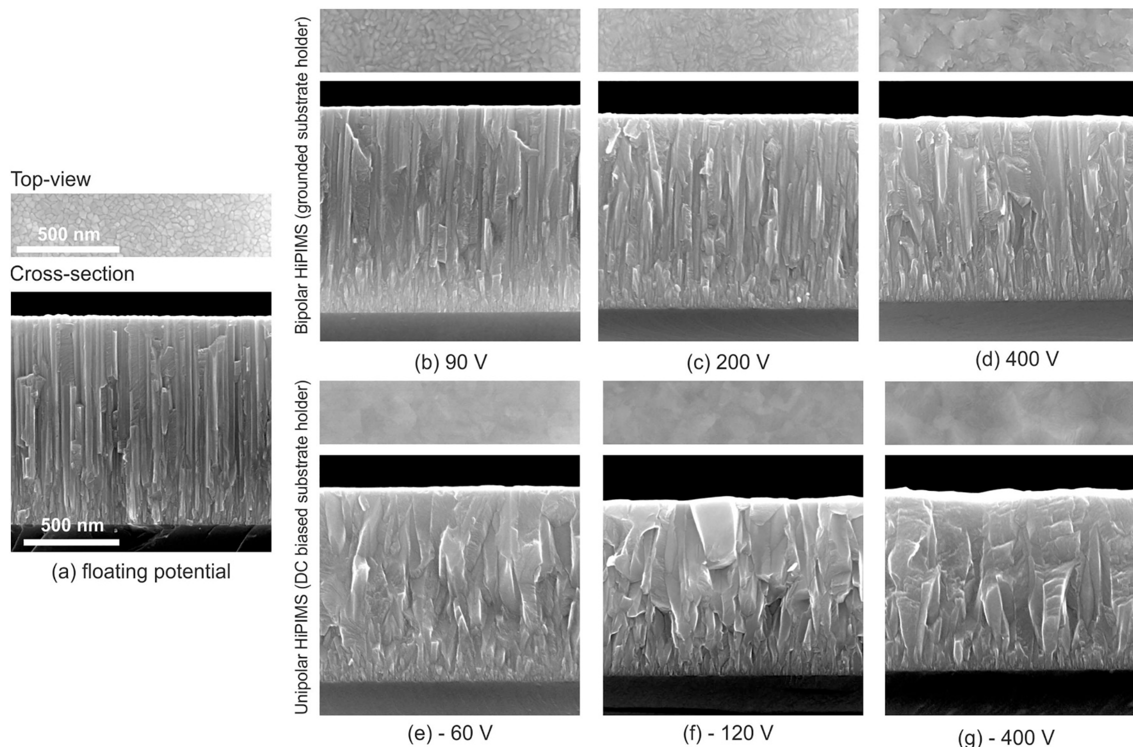

Fig. 4. Selected top-view and cross-sectional images of the CrN films prepared by unipolar HiPIMS with a floating substrate holder (a), bipolar HiPIMS with a grounded substrate holder (b)–(d) and unipolar HiPIMS with a DC biased substrate holder (e)–(g) at different applied voltage values.

of the CrN films deposited onto Si substrates, is shown in Fig. 3. All prepared films exhibit a crystalline structure with diffraction peaks corresponding to the fcc CrN phase only. This is in accordance with the measured composition stoichiometry. The diffraction peaks are shifted to lower 2Θ angles with respect to the XRD standard (PDF Card No. 04-004-6868) due to a compressive residual stress generated in the films during their growth (discussed in more detail below). The microstructural evolution, represented by top-view and cross-sectional SEM images of selected CrN films, is shown in Fig. 4.

3.3.1. Bipolar HiPIMS with a floating substrate holder

XRD patterns in Fig. 3a correspond to the CrN films prepared in the bipolar HiPIMS mode at different positive pulse voltages, with the substrate holder at a floating potential. All of the films exhibit a strong preferential (200) orientation. The microstructure of all of these films (see a representative SEM image in Fig. 4a) is highly columnar throughout the whole thickness. The top-view image shows easily distinguishable domed column tops with boundaries of lower density. In this case, we observed no obvious evolution with increasing positive pulse voltage.

It has been suggested in Ref. [19] that bipolar HiPIMS can be used for ion bombardment of the growing film, irrespective of whether depositing a non-conductive material or depositing onto non-conductive substrates. Hence, we simulated this condition using a substrate holder at a floating potential. In order for the bombarding ions to have a significant effect on the growing film, they need to be accelerated towards the substrate holder by a potential difference. Although there might be a non-negligible $U_{ps}(t)$ at the very beginning of the positive pulse, $U_{ps}(t)$ quickly decreases due to the charging effect (described in Section 3.1). The rate of this decrease depends on the ion flux and the capacitance of the film, substrate or substrate holder. In our case, $U_{ps}(t)$ during the positive pulse is very low and insufficient to cause any significant ion bombardment and consequently any changes in the crystal structure and microstructure of the films.

3.3.2. Bipolar HiPIMS with a grounded substrate holder

In order to have a considerable $U_{ps}(t)$ during the positive pulse and thus to be able to investigate the effect of the positive pulse voltage, we grounded the substrate holder during the positive pulse for further experiments, as described in Section 3.1.

In this case, the evolution of the crystal structure and microstructure with increasing positive voltage is apparent (see Fig. 3b for XRD patterns and Fig. 4b–d for SEM images). Up to 60 V, the XRD patterns remain almost unchanged, with a strong (200) preferential orientation. The microstructure in this case corresponds to that described in Section 3.3.1 and only a minor enlarging of the column tops can be seen with increasing positive voltage (not shown). From 90 V to 200 V, the intensities of the diffraction peaks decrease, as the energy delivered into the growing film increases and more lattice defects are generated. While the cross-sectional images (Fig. 4b and c) still show columnar structure, the column boundaries are not as pronounced. The top view images also indicate a gradual loss of surface features and densification (corresponding to zone Ib in a structure zone model as defined by Mahieu et al. in Ref. [23]). At 400 V, a new preferential (220) orientation emerges. The (220) lattice planes are of a lower atomic density than the (111) and (200) planes and are thus less prone to resputtering and damage by high-energy ions [24]. The columns become slightly larger and denser at a higher film thickness and the film exhibits a flaked surface (Fig. 4d).

3.3.3. Unipolar HiPIMS with a DC biased substrate holder

In order to evaluate and assess the effect of the positive pulse voltage in bipolar HiPIMS, another series of films was prepared by unipolar HiPIMS with a standard DC bias voltage applied to the substrate holder for comparison.

From Figs. 3c and 4e–g, it is apparent that the effect of a DC substrate bias voltage on the crystal structure and microstructure of the films is different from that of the positive pulse voltage. Already at −60 V, the preferential (200) orientation switches to (111), while the (311) peak also gains on intensity. From the cross-sectional SEM images (Fig. 4e), it can be seen that initially small grains grow near the substrate and start to become larger towards the surface (also evident from the top-view image), which is indicative of competitive growth (zone T in Ref. [23]) and explains the prevalence of the (111) orientation, the kinetically favored orientation with the highest growth rate under these conditions. From −60 V on, the XRD intensities decrease, even though the enlarging of the grains towards the surface becomes more pronounced. That is due to lattice damage introduced by high-energy ion bombardment. The surface seems to be quite flat, smooth and dense, with vaguely distinguishable large grains (Fig. 4f). At −400 V, however, the surface roughens, possibly due to resputtering effects. This can be seen in AFM images in Fig. 5 comparing the surface morphology of the films prepared at the positive voltage of 400 V in bipolar HiPIMS and the DC substrate bias voltage of −400 V in unipolar HiPIMS. The value of the average surface roughness of the film prepared in unipolar HiPIMS (R_a = 15.0 nm) is almost four times higher than that of the film prepared in bipolar HiPIMS (R_a = 3.9 nm).

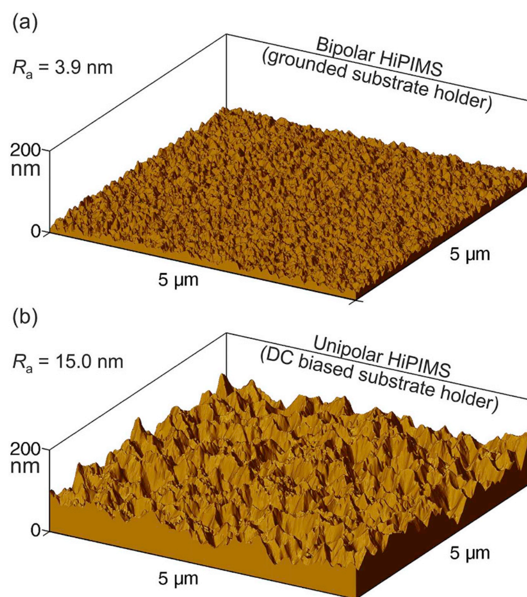

Fig. 5. Surface morphology and roughness of the CrN films prepared by bipolar HiPIMS with a grounded substrate holder (a) and unipolar HiPIMS with a DC biased substrate holder (b) at an applied voltage of 400 V and −400 V, respectively.

The differences in the effect of a positive pulse voltage in the bipolar HiPIMS discharge and a DC substrate bias voltage in the unipolar HiPIMS discharge stem from the differences in the energy delivered into the growing film by bombarding ions (see Table 1). Comparing the films from the two series where the energies are more or less equivalent (i.e. 903 kJ/cm^3 for a positive voltage of 400 V and 720 kJ/cm^3 for a DC substrate bias voltage of −60 V), we can clearly see differences in both the crystal structure and microstructure. Since the ion fluxes towards the substrate are much lower in bipolar HiPIMS, the voltage necessary for achieving the same energy must be much higher. While the high fluxes at relatively low energies promote adatom mobility and continuous crystal growth, the low fluxes at high energies cause growth disruption, renucleation and structure damages.

It is worth noting that similar sets of results were also obtained for all three series of the CrN films grown on glass substrates (not shown here). Despite the substrates being non-conductive, the films grew at the same potential as on the Si substrates. The reason is that the substrates were held in place with a small steel strip, creating an electrical contact between the grounded substrate holder and the conductive CrN film.

3.4. Mechanical properties

The hardness of the prepared CrN films is displayed in Fig. 6 together with the residual stress in order to better understand its evolution with increasing energy delivered into the growing film. Before discussing this evolution, it is important to realize that the initial value of 22.2 GPa (for the film prepared by HiPIMS without any positive pulse or substrate bias voltage) is comparable with the values presented in Refs. [8, 25]. Therefore any further enhancement in the hardness cannot be expected to be very pronounced.

To demonstrate the supremacy of the initial value, three films prepared by standard DC magnetron sputtering at the same average power density as in the HiPIMS discharge are included in Fig. 6. It can be seen that the first two films prepared at a DC substrate voltage of 0 and −60 V are in a tensile stress and exhibit a very low hardness due to their presumably underdense microstructure. It takes a DC substrate bias voltage of −90 V to reach the values of the HiPIMS films, where

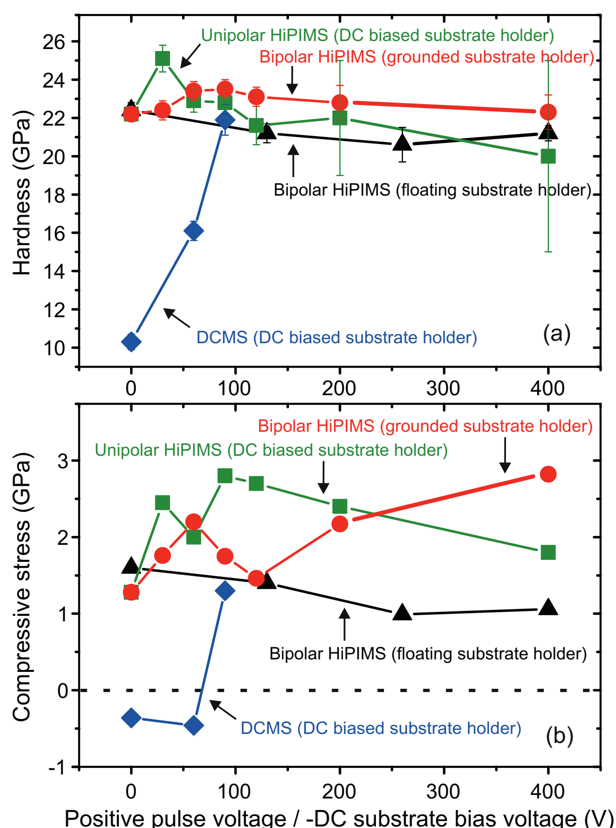

Fig. 6. Hardness (a) and residual stress (b) of the CrN films prepared by bipolar HiPIMS with a floating substrate holder (black triangles), bipolar HiPIMS with a grounded substrate holder (red circles) and unipolar HiPIMS with a DC biased substrate holder (green squares) at different applied voltage values. Three films prepared by standard DCMS at the same average power density are included for comparison (blue diamonds). (For interpretation of the references to color in this figure legend, the reader is referred to the web version of this article.)

the ion bombardment is significant even without the application of a substrate bias voltage.

Even though no obvious evolution was observed in the crystal structure and microstructure of the series of the films prepared with the substrate holder at a floating potential, small changes in the hardness can be observed, corresponding to changes in the residual stress. However, because the energy delivered into the films during their growth is negligible due to only very small $U_{ps}(t)$ during the positive pulse, the application of the positive voltage pulses does not lead to a hardness enhancement.

In the case of the films prepared using bipolar HiPIMS with the substrate holder grounded, we can, however, see a hardness enhancement. A slight increase in the hardness from 22.2 to 23.4 GPa is observed for the positive pulse voltages ranging from 0 to 60 V, which corresponds to an increase in the residual compressive stress from 1.3 to 2.2 GPa. Further increase in the positive pulse voltage (90 and 120 V) leads to a decrease in the residual compressive stress (1.7 and 1.5 GPa, respectively) while the hardness is nearly the same (23.5 and 23.1 GPa, respectively). This can be related to changes in the crystal structure and microstructure, as described above. At even higher voltages (200 and 400 V), the residual stress rises significantly while the hardness remains almost constant, which can probably be explained by increasing incorporation of argon atoms.

In the case of unipolar HiPIMS with a DC bias voltage applied to the substrate holder, the hardness is higher (25.1 GPa) only for −30 V compared to the previous series. This rise is probably connected with a significant increase in the compressive stress, which reaches, however, a value (2.5 GPa) that is too high with respect to good adhesion. The application of −60 V leads to a decrease in both the hardness and stress, possibly owing to the switch in the preferred crystallographic orientation from (200) to (111) as described in Section 3.3.3. With further increase in the substrate bias voltage, the evolution of the stress follows a trend described in Ref. [26]. In this case, unlike the case of bipolar HiPIMS, the energies delivered into the growing film at high applied voltages are high enough (thanks to higher fluxes) to introduce thermal spikes that allow atomic rearrangement and stress relief. The stress therefore goes down and thus the hardness decreases along with it. Moreover, the films exhibit a very rough surface (Fig. 5b) due to resputtering effects, contributing to very high hardness measurement errors.

3.5. Applicability of bipolar HiPIMS

Bipolar HiPIMS has been suggested to be used in cases where a DC bias voltage applied to the substrates cannot be used, i.e., in the case of a deposition of non-conductive materials or a deposition onto non-conductive substrates [19]. From this point of view, we have shown, using a substrate holder at a floating potential, that bipolar HiPIMS cannot be used instead of a DC substrate bias voltage for film deposition where charging of the film or substrate is as rapid as in this work and thus the plasma and floating potentials are close to each other. However, there are advantages to bipolar HiPIMS over a DC substrate bias voltage, discussed in the following paragraphs.

All aspects taken into consideration, the CrN films prepared by bipolar HiPIMS (with a grounded substrate holder) at a positive pulse voltage of 90 and 120 V exhibit the most interesting properties, namely high hardness at a relatively low residual stress and smooth surface.

For cases where higher voltages might be necessary, it is important to note that the discharge was stable with minimum arcing for all positive pulse voltages investigated when bipolar HiPIMS was utilized. This was not the case for the discharge with a DC substrate bias voltage, which exhibited a tendency towards severe arcing at the substrate holder and thus discharge instabilities at applied voltages higher than −120 V. In addition, the deposition rate remained relatively high even when 400 V was applied in bipolar HiPIMS, whereas it decreased significantly for higher DC substrate bias voltages due to resputtering effects.

It can be concluded that while the primary motivation for bipolar HiPIMS, to be used irrespective of whether depositing a non-conductive material or depositing onto non-conductive substrate, cannot be applied, bipolar HiPIMS still holds several advantages over a substrate bias voltage when the substrates are grounded, and can be expected to rise in popularity.

4. Conclusions

In this work, we investigated the possibility of using bipolar HiPIMS to control the crystal structure, microstructure and resulting mechanical properties of CrN films. Special attention was paid to the potential at which the substrate holder was held during the deposition. A comparison was made between bipolar HiPIMS and unipolar HiPIMS with a DC bias voltage applied to the substrate holder.

Using a substrate holder at a floating potential, we have shown that bipolar HiPIMS cannot be used instead of a DC substrate bias voltage for a deposition of non-conductive films or onto non-conductive substrates when the plasma-substrate potential difference necessary for ion acceleration is lost already at the beginning of the positive pulse due to rapid charging of the non-conductive material. Changes in the positive pulse voltage then do not lead to any significant changes in the crystal structure, microstructure and mechanical properties. However, when the substrate holder is grounded, an evolution is apparent with increasing positive pulse voltage, even on non-conductive substrates if the growing film is conductively connected with the ground.

After comparing the effect of a positive pulse voltage to the effect of

a DC bias voltage applied to the substrate holder, it was found that the effects are different and that the most interesting properties (high hardness at a relatively low residual stress) are achieved for the films prepared using bipolar HiPIMS with a grounded substrate holder at positive pulse voltages of 90 and 120 V. Additional advantages over a DC substrate bias voltage are a stable discharge and a negligible deposition rate reduction. Bipolar HiPIMS can therefore be expected to gain in popularity, presuming that the growing film is conductive and can thus be grounded.

CRediT authorship contribution statement

Š. Batková: Investigation, Data curation, Validation, Visualization, Writing - original draft, Writing - review & editing. **J. Čapek:** Conceptualization, Methodology, Validation, Writing - review & editing, Supervision, Funding acquisition. **J. Rezek:** Investigation, Writing - review & editing. **R. Čerstvý:** Investigation, Data curation. **P. Zeman:** Conceptualization, Methodology, Validation, Writing - review & editing, Supervision.

Declaration of competing interest

The authors declare that they have no known competing financial interests or personal relationships that could have appeared to influence the work reported in this paper.

Acknowledgments

This work was supported by the project no. FV30177 of the Ministry of Industry and Trade of the Czech Republic. The authors wish to thank Dr. Šimon Kos for valuable discussion of the results.

Appendix A. Supplementary data

Supplementary data to this article can be found online at https://doi.org/10.1016/j.surfcoat.2020.125773.

References

[1] A. Schröer, W. Ensinger, G.K. Wolf, A comparison of the corrosion behaviour and hardness of steel samples (100Cr6) coated with titanium nitride and chromium nitride by different institutions using different deposition techniques, Mater. Sci. Eng. A 140 (1991) 625–630, https://doi.org/10.1016/0921-5093(91)90487-8.

[2] S.T. Oyama, The Chemistry of Transition Metal Carbides and Nitrides, Blackie Academic & Professional, 1996, https://doi.org/10.1007/978-94-009-1565-7.

[3] B. Navinšek, P. Panjan, I. Milošev, Industrial applications of CrN (PVD) coatings, deposited at high and low temperatures, Surf. Coat. Technol. 97 (1997) 182–191, https://doi.org/10.1016/S0257-8972(97)00393-9.

[4] W. Lengauer, Transition Metal Carbides, Nitrides, and Carbonitrides, Wiley-VCH, 2000, https://doi.org/10.1002/9783527618217.ch7.

[5] T. Hurkmans, D.B. Lewis, H. Paritong, J.S. Brooks, W.D. Münz, Influence of ion bombardment on structure and properties of unbalanced magnetron grown CrNx coatings, Surf. Coat. Technol. 114 (1999) 52–59, https://doi.org/10.1016/S0257-8972(99)00031-6.

[6] J. Musil, H. Poláková, J. Šuna, J. Vlček, Effect of ion bombardment on properties of hard reactively sputtered Ti(Fe)Nx films, Surf. Coat. Technol. 177–178 (2004) 289–298, https://doi.org/10.1016/J.SURFCOAT.2003.09.007.

[7] R. Daniel, K.J. Martinschitz, J. Keckes, C. Mitterer, Texture development in polycrystalline CrN coatings: the role of growth conditions and a Cr interlayer, J. Phys. D. Appl. Phys. 42 (2009) 075401, , https://doi.org/10.1088/0022-3727/42/7/075401.

[8] Q. Xie, Z. Fu, X. Wei, X. Li, W. Yue, J. Kang, L. Zhu, C. Wang, J. Meng, Effect of substrate bias current on structure and properties of CrNx films deposited by plasma enhanced magnetron sputtering, Surf. Coat. Technol. 365 (2019) 134–142, https://doi.org/10.1016/J.SURFCOAT.2018.06.090.

[9] J. Vlček, P. Kudláček, K. Burcalová, J. Musil, Ion flux characteristics in high-power pulsed magnetron sputtering discharges, Epl. 77 (2007) 45002, https://doi.org/10.1209/0295-5075/77/45002.

[10] A. Hecimovic, K. Burcalova, A.P. Ehiasarian, Origins of ion energy distribution function (IEDF) in high power impulse magnetron sputtering (HIPIMS) plasma discharge, J. Phys. D. Appl. Phys. 41 (2008) 095203, https://doi.org/10.1088/0022-3727/41/9/095203.

[11] J. Lazar, J. Vlček, J. Rezek, Ion flux characteristics and efficiency of the deposition processes in high power impulse magnetron sputtering of zirconium, J. Appl. Phys. 108 (2010) 1–9, https://doi.org/10.1063/1.3481428.

[12] C. Maszl, W. Breilmann, J. Benedikt, A. Von Keudell, Origin of the energetic ions at the substrate generated during high power pulsed magnetron sputtering of titanium, J. Phys. D. Appl. Phys. 47 (2014) 224002, https://doi.org/10.1088/0022-3727/47/22/224002.

[13] J. Lin, J.J. Moore, W.D. Sproul, B. Mishra, Z. Wu, J. Wang, The structure and properties of chromium nitride coatings deposited using dc, pulsed dc and modulated pulse power magnetron sputtering, Surf. Coat. Technol. 204 (2010) 2230–2239, https://doi.org/10.1016/J.SURFCOAT.2009.12.013.

[14] A. Anders, N. Pasaja, S.H.N. Lim, T.C. Petersen, V.J. Keast, Plasma biasing to control the growth conditions of diamond-like carbon, Surf. Coat. Technol. 201 (2007) 4628–4632, https://doi.org/10.1016/J.SURFCOAT.2006.09.313.

[15] J. Keraudy, R.P.B. Viloan, M.A. Raadu, N. Brenning, D. Lundin, U. Helmersson, Bipolar HiPIMS for tailoring ion energies in thin film deposition, Surf. Coat. Technol. 359 (2019) 433–437, https://doi.org/10.1016/J.SURFCOAT.2018.12.090.

[16] R.P.B. Viloan, J. Gu, R. Boyd, J. Keraudy, L. Li, U. Helmersson, Bipolar high power impulse magnetron sputtering for energetic ion bombardment during TiN thin film growth without the use of a substrate bias, Thin Solid Films 688 (2019) 137350, https://doi.org/10.1016/J.TSF.2019.05.069.

[17] I.-L. Velicu, G.-T. Ianoş, C. Porosnicu, I. Mihăilă, I. Burducea, A. Velea, D. Cristea, D. Munteanu, V. Tiron, Energy-enhanced deposition of copper thin films by bipolar high power impulse magnetron sputtering, Surf. Coat. Technol. 359 (2019) 97–107, https://doi.org/10.1016/J.SURFCOAT.2018.12.079.

[18] J.A. Santiago, I. Fernández-Martínez, T. Kozák, J. Capek, A. Wennberg, J.M. Molina-Aldareguia, V. Bellido-González, R. González-Arrabal, M.A. Monclús, The influence of positive pulses on HiPIMS deposition of hard DLC coatings, Surf. Coat. Technol. 358 (2019) 43–49, https://doi.org/10.1016/J.SURFCOAT.2018.11.001.

[19] V. Tiron, E.-L. Ursu, D. Cristea, D. Munteanu, G. Bulai, A. Ceban, I.-L. Velicu, Overcoming the insulating materials limitation in HiPIMS: ion-assisted deposition of DLC coatings using bipolar HiPIMS, Appl. Surf. Sci. 494 (2019) 871–879, https://doi.org/10.1016/J.APSUSC.2019.07.239.

[20] R. Hippler, M. Cada, V. Stranak, Z. Hubicka, Time-resolved optical emission spectroscopy of a unipolar and a bipolar pulsed magnetron sputtering discharge in an argon/oxygen gas mixture with a cobalt target, Plasma Sources Sci. Technol. 28 (2019) 115020, , https://doi.org/10.1088/1361-6595/ab54e8.

[21] J. Musil, Flexible hard nanocomposite coatings, RSC Adv. 5 (2015) 60482–60495, https://doi.org/10.1039/c5ra09586g.

[22] S.K. Karkari, A. Vetushka, J.W. Bradley, Measurement of the plasma potential adjacent to the substrate in a midfrequency bipolar pulsed magnetron, J. Vac. Sci. Technol. A 21 (2003) L28–L32, https://doi.org/10.1116/1.1622673.

[23] S. Mahieu, P. Ghekiere, D. Depla, R. De Gryse, Biaxial alignment in sputter deposited thin films, Thin Solid Films 515 (2006) 1229–1249, https://doi.org/10.1016/j.tsf.2006.06.027.

[24] C. Gautier, H. Moussaoui, F. Elstner, J. Machet, Comparative study of mechanical and structural properties of CrN films deposited by d.c. magnetron sputtering and vacuum arc evaporation, Surf. Coat. Technol. 86–87 (1996) 254–262, https://doi.org/10.1016/S0257-8972(96)02951-9.

[25] J.-W. Lee, S.-K. Tien, Y.-C. Kuo, The effects of pulse frequency and substrate bias to the mechanical properties of CrN coatings deposited by pulsed DC magnetron sputtering, Thin Solid Films 494 (2006) 161–167, https://doi.org/10.1016/J.TSF.2005.07.190.

[26] M.M.M. Bilek, D.R. McKenzie, A comprehensive model of stress generation and relief processes in thin films deposited with energetic ions, Surf. Coat. Technol. 200 (2006) 4345–4354, https://doi.org/10.1016/j.surfcoat.2005.02.161.

D

Effect of exit-orifice diameter on Cu nanoparticles produced by gas-aggregation source

Š. Batková, T. Kozák, S. Haviar, P. Mareš, J. Čapek

Surface & Coatings Technology 417 (2021) 127196

Surface & Coatings Technology 417 (2021) 127196

Contents lists available at ScienceDirect

Surface & Coatings Technology

journal homepage: www.elsevier.com/locate/surfcoat

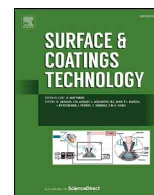

Effect of exit-orifice diameter on Cu nanoparticles produced by gas-aggregation source

Š. Batková [a], T. Kozák [a], S. Haviar [a], P. Mareš [b], J. Čapek [a,*]

[a] Department of Physics and NTIS - European Centre of Excellence, University of West Bohemia, Univerzitní 8, 306 14 Plzeň, Czech Republic
[b] HVM Plasma, Na Hutmance 2, 158 00 Praha, Czech Republic

ARTICLE INFO

Keywords:
Gas-aggregation source
Cu nanoparticles
Exit-orifice diameter
Pressure to flow rate ratio
Size distribution

ABSTRACT

Gas-aggregation source (GAS) was used to prepare Cu nanoparticles. By changing the diameter of the exit orifice of the aggregation chamber, we were able to isolate and investigate the effect of the flow rate of the working gas at a constant pressure inside the aggregation chamber. We show that the conventional approach of changing pressure by adjusting the flow rate (at a constant orifice diameter) does not significantly influence the nanoparticle size. However, when the pressure is held constant, changing the flow rate has a notable effect. Based on a theoretical study, we suggest that the determining parameter which needs to be considered is the pressure to flow rate ratio. This ratio determines the residence time of the nanoparticles inside the aggregation chamber (and therefore the time available for them to grow) and is constant for a constant orifice diameter. Decreasing the orifice diameter, however, increases the pressure to flow rate ratio, which gives the nanoparticles longer time inside the aggregation chamber and allows them to grow larger. Apart from their size, the orifice diameter also influences the mass flux and its angular distribution.

1. Introduction

Nanoparticles (also referred to as nanoclusters or simply clusters) are very well known to have unique physical and chemical properties due to their nanoscale size [1]. The properties make them interesting for numerous applications, for example, in medicine [2], energy harvesting and storage [3,4], and electronics [5].

There are many types of sources of nanoparticles [6]. The one utilizing gas condensation has become very popular in recent years due to its enhanced control of nanoparticles' properties [7–10]. This source (the so-called gas-aggregation source, GAS) is based on aggregation of the nanoparticles from a gas phase of a base material, which is supersaturated in an aggregation chamber by a high-pressure working gas (i.e., Ar gas or Ar gas with an admixture of reactive gases). The formed nanoparticles are then carried by the working gas out of the aggregation chamber through an exit orifice. The aggregating gas phase can be produced by various techniques (e.g., hollow cathode sputtering [11], thermal evaporation [12]), but is most often produced by magnetron sputtering as it is also in this work.

Size control of the nanoparticles is very important in nanoparticle preparation, as their properties are size-dependent [13,14]. The process of nanoparticle formation in GAS has been investigated both experimentally [15,16] and theoretically [17–20] and the resulting nanoparticle beam leaving the source has also been characterized [21]. Several key parameters have been reported to influence the formation process: the working-gas pressure [22–27], aggregation length (i.e., target-to-orifice distance) [24,27], discharge power [24,27,28], discharge regime (DC, mid-frequence or HiPIMS) [29,30], degree of target erosion [31] and oxygen admixture into the working gas [32–34]. The first one is possibly the most frequently discussed parameter. However, conventionally, the control of the pressure is managed by adjusting the flow rate of the working gas, which leads to an undesirable simultaneous change of two important parameters, both influencing the formation of nanoparticles.

In this work, we introduce an additional parameter influencing the working-gas pressure, namely the exit-orifice diameter. This approach allows us to isolate and investigate, both experimentally and theoretically, the effect of the working-gas flow rate on the generation of nanoparticles at a given constant working-gas pressure.

The choice of Cu as a model target material in this study was made in accordance with previous works of other authors [7,29,35,36]. However, it is highly expected that the here-presented findings and

* Corresponding author.
E-mail address: jcapek@kfy.zcu.cz (J. Čapek).

https://doi.org/10.1016/j.surfcoat.2021.127196
Received 25 February 2021; Received in revised form 15 April 2021; Accepted 16 April 2021
Available online 21 April 2021
0257-8972/© 2021 Elsevier B.V. All rights reserved.

conclusions may be valid for any material in general.

2. Experimental details

The nanoparticles were prepared using a custom-built gas-aggregation source (GAS) (HVM Plasma) mounted onto a cylindrical vacuum deposition chamber (500 mm in diameter and 414 mm in height) at an angle of 30° from the vertical axis of the chamber (see Fig. 1a). The GAS consists of a cylindrical magnetron (equipped with an in-situ axial movement) placed inside a grounded cylindrical aggregation chamber of a diameter of 100 mm terminated by a conical ending with a replaceable exit orifice (cylindrically-shaped orifices with a diameter, *d*, of 1.5, 2, 3 and 4 mm and a height of 3 mm were used in this work).

The whole deposition system (including the aggregation chamber of the GAS) was pumped by a turbomolecular pump (1250 l/s for N_2, HiPace 1200, Pfeiffer Vacuum) backed up with a scroll pump (35 m^3/h for N_2, XDS35i, Edwards). A vacuum bypass made of a DN40ISO-CF corrugated hose connecting the main chamber with the aggregation chamber was used during the pumping process before the experiments to improve the vacuum level in the aggregation chamber. The aggregation chamber was baked out up to ~100 °C prior to each deposition series and during the experiments the chamber was water cooled. The base pressure before each experiment in the main chamber and the aggregation chamber was 8×10^{-6} Pa and 2×10^{-5} Pa, respectively.

Argon 6.0, at a flow rate ϕ, was introduced into the aggregation chamber from in between the target and its shielding (see Fig. 1b). The flow rate of the Ar gas was controlled by a mass-flow controller (MF1, MKS Instruments). The resulting Ar pressure in the aggregation chamber, *p*, was measured by a full-range gauge (PKR 251, Pfeiffer Vacuum), which was located behind the magnetron, as illustrated in Fig. 1b. It is important to note that a capacitance gauge placed in the same location gave values that were higher by a factor of approximately two.

The magnetron was equipped with a circular Cu target (50 mm in diameter, 3.2 mm in thickness). The magnetron shielding was at a floating potential and the grounded walls of the aggregation chamber worked as a discharge anode. The target-to-orifice distance (i.e., the aggregation length) was set to 150 mm. The magnetron was driven by a DC power supply (Genesys 750 W, TDK-Lambda) at a constant average target power density of 5 W/cm^2.

The rotating (40 rpm) substrate holder was at a distance of 400 mm from the exit orifice. The nanoparticles were deposited onto polished and ultrasonically cleaned Si (100) substrates spanning the whole radius of the substrate holder (45 mm). The deposition times were varied according to the mass flux of the nanoparticles, Γ, to obtain a comparable nanoparticle density at the substrate surface.

The value of Γ was measured by a quartz crystal microbalance (QCM) (STM-2, Inficon) with a measurement area of 0.5 cm^2. It was possible to rotate the crystal around an axis parallel to the axis of the beam of nanoparticles, enabling measurements in a plane perpendicular to the beam (QCM plane). The distance of the crystal from the exit orifice when positioned in the beam center was 23.5 cm. The values that were measured in the QCM plane were subsequently recalculated onto a sphere with a radius $r = 23.5$ cm (see Fig. 1b).

The nanoparticle images were obtained using a scanning electron microscope (SU-70, Hitachi). The images were analyzed using the Gwyddion software to obtain sizes of individual nanoparticles. For non-spherical particles, the projected area on the SEM micrograph for each particle was measured and the radius of an equivalent circle with the same area was computed. The size distribution was then plotted (see an example for $d = 4$ mm at $p = 86$ Pa in Fig. 2). The number of bins was chosen based on the number of observed particles (both the Scott's or the Rice rule give 24 bins for about 2000 particles). In plots where a high radii tail exceeds a uni-modal distribution or distinct peaks are observed, each peak corresponding to a nanoparticle family was fitted with an individual log-normal distribution. The presented radius is the median of the fitted distribution.

The computational fluid dynamics (CFD) models of the argon flow in the nanoparticle source were calculated using the ANSYS Fluent 2020 R2 software. The argon was simulated as an ideal gas with a specific heat, thermal conductivity and viscosity calculated using the kinetic

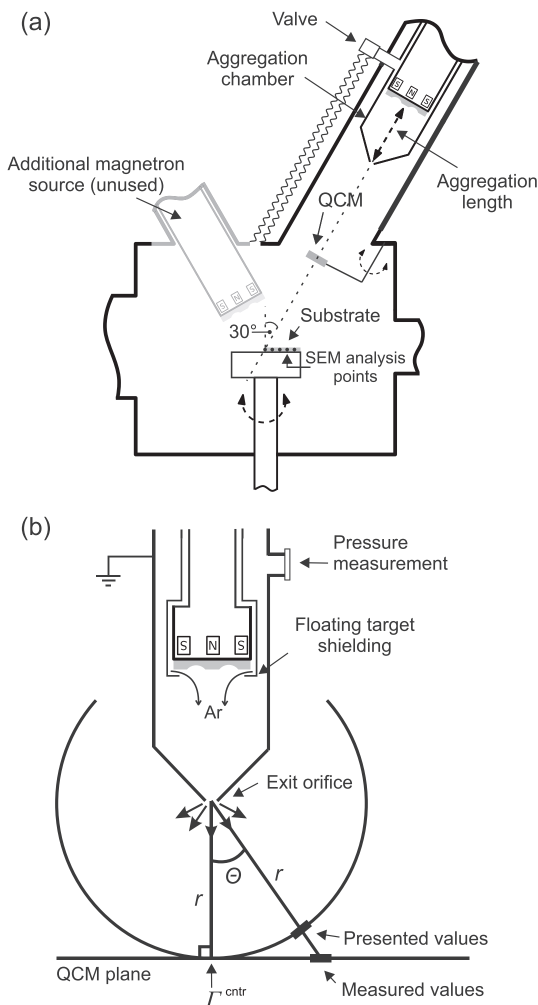

Fig. 1. Schematic diagram of the whole deposition system (a) and detailed illustration of the aggregation chamber and the measurement of the mass flux of the nanoparticles (b).

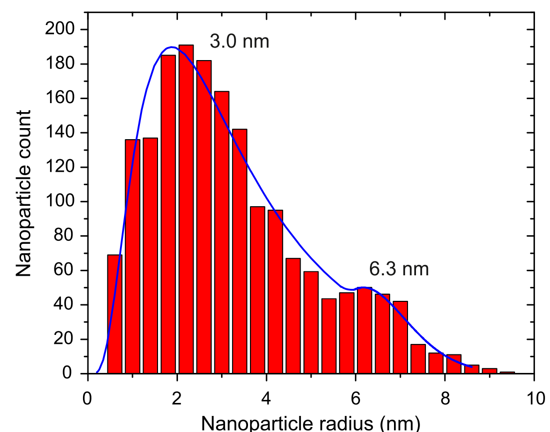

Fig. 2. Example of a nanoparticle-size evaluation corresponding to the exit-orifice diameter, *d*, of 4 mm and the argon pressure inside the aggregation chamber, *p*, of 86 Pa. Each of the peaks was fitted with a log-normal distribution and its median was used as the presented radius.

theory. The simulation considered turbulences of the gas using the generalized k-ω model and the energy equation. The three-dimensional poly-hexcore mesh with about 5 million cells was created in ANSYS Fluent Meshing with the maximum inverse orthogonal quality of the cells bellow 0.7. The mesh consisted of eight inflation cells at the walls, followed by two polyhedral transition cells. The volume of the model was filled by a hexcore mesh. The experimental value of ϕ was used as the input flow rate of the model. The pressure outlet of 0.07 Pa was positioned 300 mm from the orifice, in order to not influence the creation and the development of the high-velocity jet of the argon gas in the deposition chamber. The simulations were solved by a coupled scheme with the pseudo-transient formulation. To calculate residence times, 40 streamlines, starting just above the target, ending at the orifice and distributed evenly across the flow field, were selected. The mean value of time spent on these streamlines was taken as the residence time of the nanoparticles.

3. Experimental results

In this section, we first present the conditions that were chosen for nanoparticle deposition and for further experiments (Fig. 3). We then report on the size distribution of the prepared nanoparticles (Figs. 4 and 5), the angular distribution of the mass flux of the nanoparticles (Fig. 6), the mass flux of the nanoparticles at the center of the nanoparticle beam (Fig. 7a) and the total (i.e., integrated over the whole sphere) mass flow rate of the nanoparticles (Fig. 7b).

3.1. Experimental conditions

First, Ar gas pressure inside the aggregation chamber, p, as a function of the Ar gas flow rate, ϕ, was investigated for exit orifices with a diameter, d, of 1.5, 2, 3 and 4 mm as presented in Fig. 3. As might be expected, the measured dependencies are linear in the working range. Let us note that an orifice with $d = 1$ mm was not used in this study due to a very low flux of nanoparticles at the substrate hindering a correct evaluation of the nanoparticles' characteristics discussed further.

The presented data demonstrate that with the used orifice diameters, it is not possible to obtain conditions where we could keep a constant ϕ and set p to more than two different values. The control of d does, however, allow us to investigate the formation of nanoparticles at selected pressures, but at significantly different flow rates. For further experiments, five values of p (60, 70, 86, 100 and 120 Pa) were thus selected, as indicated by horizontal lines in Fig. 3.

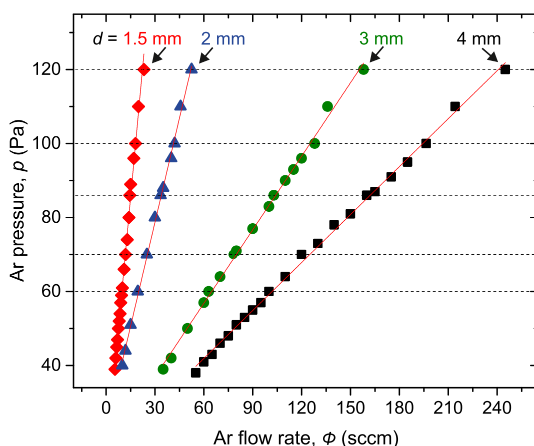

Fig. 3. Argon pressure inside the aggregation chamber, p, as a function of Ar flow rate, ϕ, for the exit-orifice diameter, d, of 1.5, 2, 3 and 4 mm. Horizontal lines denote values of p chosen for further experiments (60, 70, 86, 100 and 120 Pa). Red lines denote a linear fit of the measured data.

3.2. Size distribution of nanoparticles

Fig. 4 shows SEM images of the nanoparticles prepared at the conditions described above. Columns show the conventional approach of increasing p by increasing ϕ. In rows, however, we were able to keep a constant p value while significantly changing ϕ (refer to the bottom-left corner of each slot) by using orifices with different d.

Images were taken at 5 different positions on the substrate. The first image was taken in the center of the substrate holder, e.g., center of the nanoparticles beam. The next images were then taken with a step of 10 mm in the radial range (see Fig. 1a). No obvious spatial variation in nanoparticle size was observed and a place with nanoparticle density appropriate for further analysis was chosen for each specimen.

The evaluated nanoparticle sizes are plotted in Fig. 5. At some conditions, more than one size family can be distinguished. In such a case, the height of each subcolumn (marked by different colors) represents the nanoparticle radius, while the width of each subcolumn (the total width of the columns is conserved) indicates the relative amount of nanoparticles of the respective size. The dominant family is always denoted black. It can be seen that at $p = 60$ Pa all distributions exhibit a single size family. With increasing p, two size families start appearing for $d = 4$ mm and eventually all distributions exhibit two size families at the highest pressures ($p = 100$ and 120 Pa). This indicates that the size distribution becomes narrower with decreasing d and p.

One can see a trend where the nanoparticle size decreases with increasing d at constant p (rows in Fig. 4). On the other hand, there is only a weak dependence on increasing p at constant d (columns in Fig. 4). In this case, the dependence is not monotonous for lower p values and very small amounts of larger particles only start appearing at $p =$ 100 Pa and higher for each orifice.

3.3. Mass flux of nanoparticles

The mass flux of the nanoparticles, Γ, was measured by a quartz crystal microbalance (QCM). In order to measure the spatial distribution of the nanoparticles coming out of the exit orifice of the nanoparticle source, the QCM was motorized. The measured angular distribution of Γ was then recalculated onto a sphere as described in Section 2 and shown in Fig. 1b, and subsequently normalized with respect to the mass flux at the center of the nanoparticle beam, Γ^{cntr}. Fig. 6 shows this normalized mass flux, $\Gamma^* = \Gamma / \Gamma^{cntr}$, as a function of the angle between the axis of the nanoparticle beam and the measurement position, Θ, for two chosen values of $p = 70$ Pa (Fig. 6a) and $p = 100$ Pa (Fig. 6b). The measured data were fitted by a normal distribution with a fixed amplitude of 1 and center at 0. It can be clearly seen that the nanoparticle beam gets wider for smaller d (i.e., lower ϕ). Fig. 6 also shows an interesting phenomenon (more pronounced at smaller d), where some of the measured data exhibit a deviation from the normal distribution in a form of a rise in Γ^* at certain values of Θ.

The measured values of Γ^{cntr}, together with standard deviations as error bars are plotted in Fig. 7a. The normalized curves from Fig. 6 were then multiplied by the corresponding Γ^{cntr} value, interpolated and integrated over the whole sphere to obtain the total mass flow rate, R, as:

$$R(dp) = \int \Gamma^*(d, p, \theta) \Gamma^{cntr}(dp) 2\pi r^2 sin\theta d\theta. \quad (1)$$

The values of R for each pressure are plotted in Fig. 7b. The two missing data points for $p = 86$ and $p = 120$ Pa at $d = 1.5$ mm are due to Γ being too low for a valid measurement of the angular distribution.

The Γ^{cntr} values in Fig. 7a would indicate that the mass flux of nanoparticles increases significantly with increasing d, where the values span over multiple orders of magnitude. While the R values indicate a similar trend, the differences are, however, not as large anymore, and it is not the case for all pressures.

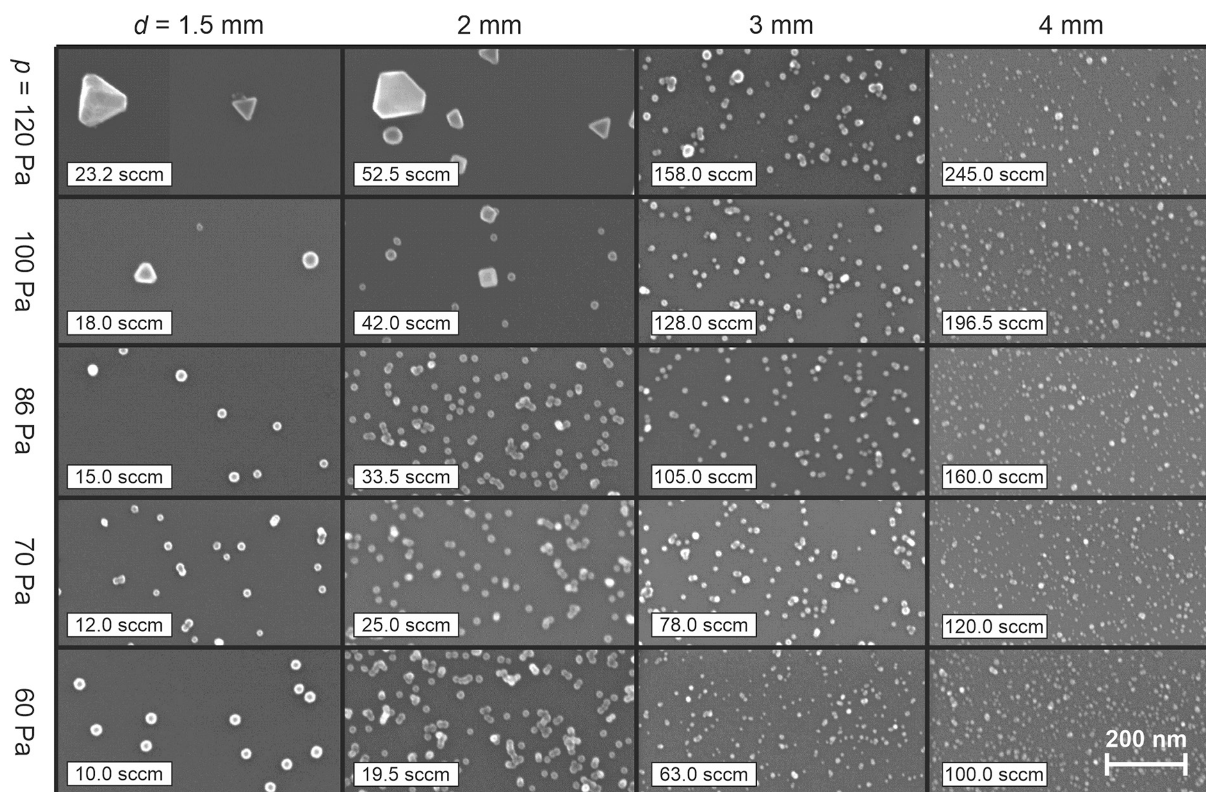

Fig. 4. SEM images of nanoparticles prepared at the exit-orifice diameter, *d*, of 1.5, 2, 3 and 4 mm (horizontal axis) and the argon pressure inside the aggregation chamber, *p*, of 60, 70, 86, 100 and 120 Pa (vertical axis). In columns, *p* was increased by increase in Ar flow rate, ϕ (conventional approach), while rows show the effect of changing ϕ at a constant value of *p*. The corresponding flow rates are displayed in bottom-left corner of each slot.

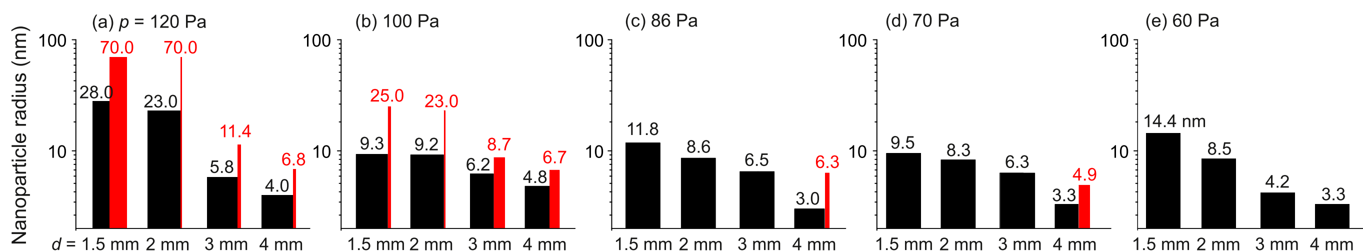

Fig. 5. Size of nanoparticles as a function of the exit-orifice diameter, *d*, prepared at the argon pressure inside the aggregation chamber, *p*, of 120 Pa (a), 100 Pa (b), 86 Pa (c), 70 Pa (d) and 60 Pa (e). The height of each subcolumn (marked by different colors) represents the nanoparticle radius, while the width of each individual subcolumn (the total width is conserved) represents the relative amount of nanoparticles of the respective size. The dominant nanoparticle family is denoted black.

4. Discussion

4.1. Size distribution of nanoparticles

Here, we base our discussion on the work of K. Fujioka [37] and further expand it. From the balance of the incoming gas flow rate and that passing through the aggregation chamber (see Section A.1 in Appendix A) we can calculate the mean drift velocity of Ar gas in cm/s as:

$$v_g = 7.87\frac{T}{D^2}\frac{\phi}{p}, \tag{2}$$

where ϕ and p are in sccm and Pa, respectively, T is the gas temperature in K and D is the chamber diameter in cm. The v_g values range from 4.25 to 46.88 cm/s for $d = 1.5$ to $d = 4$ mm, respectively.

We further assume the nanoparticles to be thermalized and in equilibrium with the working background gas and therefore have the same v_g as the gas inside the aggregation chamber. Note that the mean free path of Cu atoms in Ar gas at $p = 40$ Pa is less than 0.1 mm, and it will be even smaller for larger nanoparticles and higher pressures. The first approximation for the residence time, τ, of the nanoparticles inside the nanoparticle source in seconds can be calculated using v_g and chamber length, L, in cm as:

$$\tau = \frac{L}{v_g} = 0.13\frac{D^2L}{T}\frac{p}{\phi} = \text{const}\ \frac{p}{\phi}. \tag{3}$$

This equation indicates an important fact that τ depends (for a given experimental setup) on the pressure to flow rate ratio only.

The Péclet number, Pe, is useful to compare the radial (diffusive) and the axial (drift) transport rates. In Ref. [37] it is defined as:

$$\text{Pe} = \frac{v_g D}{4D_m}, \tag{4}$$

where D_m is the diffusion coefficient of metal atoms in Ar gas (see Section A.2 in Appendix A). After substitution, we obtain:

$$\text{Pe} = 0.98\frac{\phi}{T^{1/2}D}. \tag{5}$$

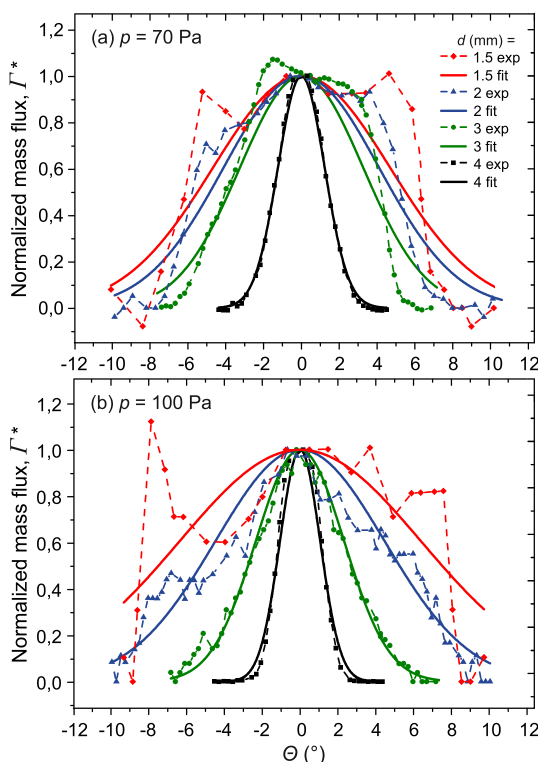

Fig. 6. Measured data (connected symbols) and fitted normal distributions (solid lines) of the angular distribution of the normalized mass flux, Γ^*, for the exit-orifice diameter, d, of 1.5, 2, 3 and 4 mm at chosen argon pressures inside the aggregation chamber, p, of 70 Pa (a) and 100 Pa (b). The legend shown in (a) applies to (b) as well.

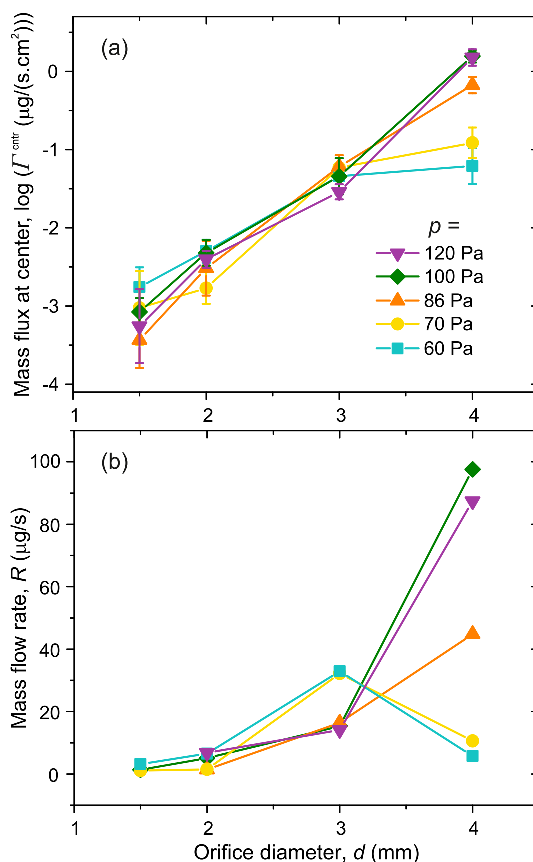

Fig. 7. Mass flux at the center of the nanoparticle beam, Γ^{cntr} (error bars indicate standard deviation) (a) and the mass flow rate, R (b), as a function of the exit-orifice diameter, d, for the argon pressure inside the aggregation chamber, p, of 60, 70, 86, 100 and 120 Pa. The legend shown in (a) applies to (b) as well.

For large values of Pe the axial drift dominates and the metal atoms are expected to be more concentrated along the chamber axis. Conversely, when Pe is small, the metal atom density is more evenly distributed in the radial direction.

Nanoparticle formation is a complex matter, where a lot of different mechanisms contribute to the process (e.g., atom adsorption or coagulation processes). In this work, we focus on a first approximation, where nanoparticle size should increase linearly with τ due to the continuous attachment of metal atoms to the already formed nanoparticles. This is also confirmed by the results of Fujioka's detailed simulation [37]. Eq. (3) indicates that for a constant d, which leads to a constant p to ϕ ratio (see linear dependence in Fig. 3), τ is constant. Therefore, no significant increase in size can be expected when increasing p by the conventional way of increasing ϕ (columns in Fig. 4). Only a slight increase in size with increasing ϕ, when τ remains constant, can be observed. This weak dependence might be connected with the dependence of the Pe number on ϕ (Eq. (5)), which affects the distribution of the metal atom density and, consequently, the nucleation rate of nanoparticles in the aggregation chamber as discussed above.

On the other hand, when p is kept constant and ϕ changes due to the control of d (rows in Fig. 4), the p to ϕ ratio and therefore also τ are no longer constant (Eq. (3)). Given longer τ inside the aggregation chamber at smaller d, the nanoparticles can grow significantly larger.

If we then further consider the balance of the incoming Ar gas flow and the outgoing gas flow through the exit orifice of diameter d (in mm) (see Section A.3 in Appendix A), we get:

$$\frac{p}{\phi} = 1.37\frac{\sqrt{T}}{d^2}, \quad (6)$$

and therefore

$$v_g = 5.74\frac{d^2\sqrt{T}}{D^2}. \quad (7)$$

For τ we then get:

$$\tau = \frac{1}{5.74}\frac{D^2 L}{d^2\sqrt{T}}. \quad (8)$$

This equation allows us to express τ using a single controllable variable d. It clearly shows that decreasing the d value lengthens τ.

To support these results, computer simulations of argon flow in the aggregation chamber were carried out (see below for more details). The obtained residence times are 2.11, 0.87, 0.27 and 0.17 s for orifice diameters 1.5, 2, 3 and 4 mm, respectively. For comparison, the residence times calculated from Eq. (3) for the respective conditions (pressure of 100 Pa) are 3.53, 1.51, 0.50 and 0.32 s, respectively. Fig. 8 shows the velocity streamlines and it can be seen that the effective diameter of the flow channel is less than the diameter of the aggregation chamber, which explains why the simulation results are systematically lower than calculations based on Eq. (3) (see the assumptions used for its derivation). The ratio of both results increases monotonously with increasing orifice diameter and ranges from 1.68 to 1.92. Therefore, we conclude that there is a close correlation, though not exact agreement, between the simulated (more accurate) residence time and the one calculated from Eq. (3). By that we verify that Eq. (3) can be used to qualitatively assess the effect of residence time on the size of nanoparticles.

Let us note that the exceptionally large nanoparticles that appear at p = 120 Pa for d = 1.5 and 2 mm orifices can probably not be explained by the provided discussion. It is highly probable that at conditions such

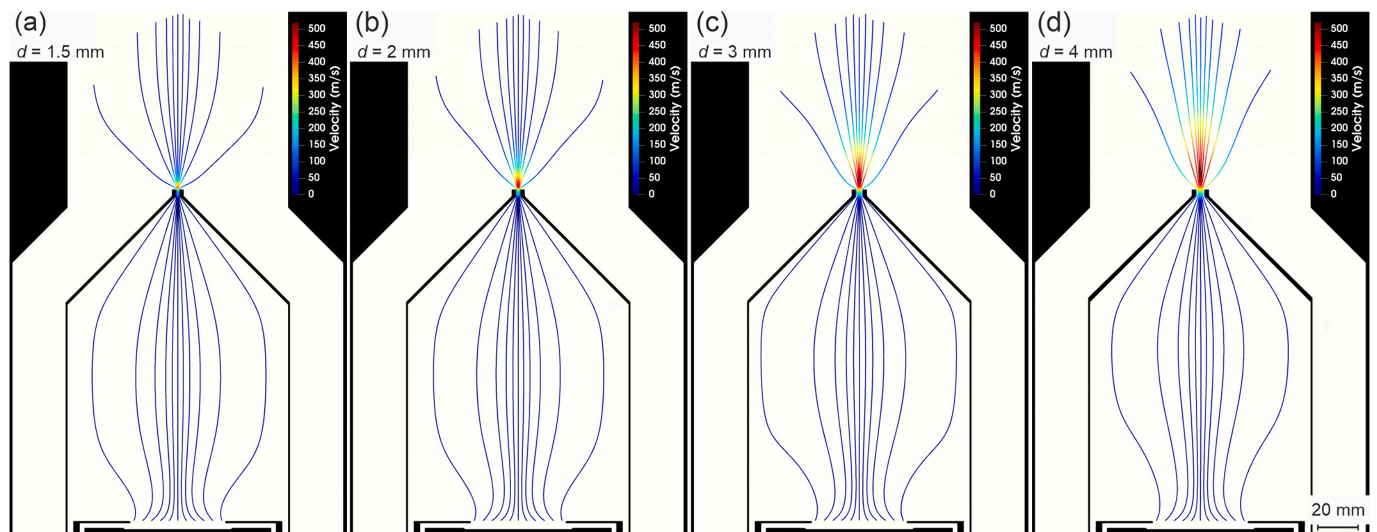

Fig. 8. Velocity streamlines of the argon working gas for the exit-orifice diameter, *d*, of 1.5 mm (a), 2 mm (b), 3 mm (c) and 4 mm (d) and the argon pressure inside the aggregation chamber, *p*, of 100 Pa.

as these (very high p at low ϕ), some other influence is involved. A more detailed study of the process is necessary.

4.2. Mass flux of nanoparticles

Next, let's focus on the total (i.e., integrated over the whole sphere) mass flow rate, R (as presented in Fig. 7b). The metal dimers (two-atom seeds necessary for further nanoparticle growth) are created by the nucleation process (three-body collision) with the rate $R_{\mathrm{nucl}} = K_{\mathrm{nucl}}\, n_{\mathrm{m}}^2\, n_{\mathrm{g}}$, where K_{nucl} is the nucleation rate constant. We assume that the metal density, $n_{\mathrm{m}} \propto 1/v_{\mathrm{g}}$ and the working gas (Ar) density, $n_{\mathrm{g}} \propto p/T$. If we further assume that dimers are lost only by exiting the aggregation chamber, we can estimate the upper bound for the dimer density, $n_2^{\max}$, as:

$$n_2^{\max} = \frac{K_{\mathrm{nucl}} n_{\mathrm{m}}^2 n_{\mathrm{g}} L}{2 v_{\mathrm{g}}} \propto \frac{p}{T^{5/2} d^6}, \tag{9}$$

where the proportionality was derived using the scalings given above. This equation indicates that the dimer density strongly depends on *d*. A smaller *d* should thus yield significantly more dimers and therefore more nanoparticles than a larger one. However, Fig. 7 suggests otherwise. We believe that at a larger *d*, both the increased v_{g} and *d* values allow more nanoparticles to actually leave the aggregation chamber and hit the QCM per given time and the differences in the nucleation rate are insignificant in comparison.

Fig. 6 shows that the nanoparticle beam becomes narrower at larger *d* values. To better understand this phenomenon, computer simulations of argon flow in the aggregation chamber (mentioned above) were carried out. In Fig. 8 we show the velocity streamlines of the argon gas, starting at the target, at $p = 100$ Pa inside the aggregation chamber. It can be seen that as the gas exits the aggregation chamber through the orifice, the streamlines form a kind of a narrow high-velocity jet. As ϕ increases with increasing *d* to maintain constant *p*, the maximum velocity inside the jet increases (397, 465, 503 and 519 m/s for 1.5, 2, 3 and 4 mm orifice, respectively), the streamlines diverge less and the stream becomes narrower. The nanoparticles coming out of the exit orifice are swept along and accelerated by the exiting gas, which limits their radial diffusion and results in a narrower nanoparticle beam at larger *d*.

4.3. Deviation in angular distribution of the mass flux

The unexpectedly high values of Γ^* (the normalized mass flux) at certain angles Θ described and shown above in Fig. 6 were measured to be relatively symmetric around the nanoparticle beam axis. Fig. 9 shows the measured Γ^* values for $d = 2$ mm at $p = 30$ Pa, where this deviation was most obvious. These conditions were not included in the above experiments, because at such low *p*, the nanoparticle beam was not formed for all orifice diameters. The figure shows the angular mass flux distribution for three different targets, each with a different degree of erosion. It can be seen that when the target is new and flat, the maximum mass flux is in the center of the nanoparticle beam. When the target is partly eroded, the deviation starts appearing and is very pronounced for a target with a high degree of erosion.

As the target becomes more eroded, the spatial distribution of the sputtered atoms changes. Assuming that most atoms are ejected along the surface normal, there is a local increase in the metal atom density above the race track of the eroded target and the probability of a nanoparticle being created in this area rises. The nanoparticle then follows the gas velocity streamline from the target (Fig. 8) and since the streamlines do not cross, the location of the nanoparticle origin is projected into the spatial distribution of Γ^*. For higher *p* and larger *d*, this distribution is no longer observable. The reason is that the above

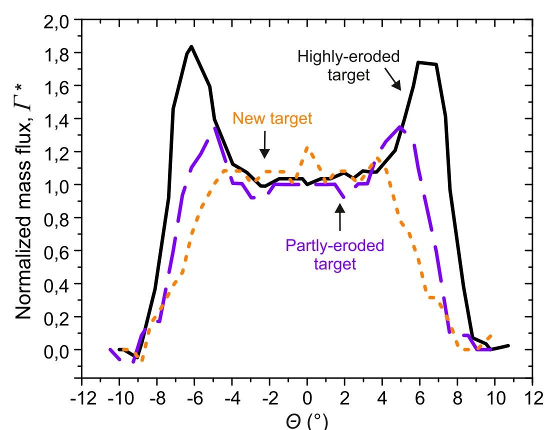

Fig. 9. Angular distribution of the normalized mass flux, Γ^*, for the exit-orifice diameter, *d*, of 2 mm and the argon pressure inside the aggregation chamber, *p*, of 30 Pa for three targets with a different degree of erosion.

described high-velocity jet sweeps and accelerates the nanoparticles along and it no longer matters where they were created.

5. Conclusions

In this work, we investigated the effect of an exit-orifice diameter of a gas-aggregation source on the size of the prepared nanoparticles, the mass flux of the nanoparticles and its angular distribution. By changing the orifice diameter, we were able to independently control the flow rate of the argon working gas at a constant Ar pressure and investigate its effect.

We have shown that the conventional approach of increasing the working-gas pressure by increasing its flow rate does not significantly influence the nanoparticle size. However, when the pressure is kept constant and the flow rate changes due to the utilization of various orifice diameters, the nanoparticle size increases significantly with decreasing orifice diameter. Furthermore, the mass flux increases and the nanoparticle beam becomes narrower with increasing orifice diameter.

The results suggest that the important parameter to consider is the pressure to flow rate ratio, which is constant for a constant orifice diameter, but changes together with the orifice diameter. This ratio determines the drift velocity and the residence time of the nanoparticles inside the aggregation chamber. These two parameters in turn affect the size, the mass flux and its angular distribution.

CRediT authorship contribution statement

Š. Batková: Investigation, Data curation, Validation, Visualization, Writing – original draft, Writing – review & editing. **T. Kozák:** Investigation, Data curation, Formal analysis, Writing – review & editing. **S. Haviar:** Methodology, Writing – review & editing. **P. Mareš:** Investigation, Data curation. **J. Čapek:** Conceptualization, Methodology, Validation, Supervision, Funding acquisition, Writing – review & editing.

Declaration of competing interest

The authors declare that they have no known competing financial interests or personal relationships that could have appeared to influence the work reported in this paper.

Acknowledgments

The work was supported by the Czech Science Foundation under Project No. 19-13174S.

Appendix A

A.1. Balance of incoming and passing-through Ar gas flow rate

The Ar gas density in the aggregation chamber, n_g, is proportional to its pressure, p, as:

$$n_g = \frac{p}{k_B T}, \tag{A1}$$

where k_B is the Boltzmann constant and T is the gas temperature. We assume a homogeneous flow of ideal gas across the cross-section of the aggregation chamber and, thus, a constant gas velocity from the gas inlet to the exit orifice. We consider a balance of the incoming gas flow rate, F_{in}, in particles/s and the flow rate through the chamber cross-section:

$$F_{in} = \phi \times 4.48 \times 10^{17} = n_g v_g A_c, \tag{A2}$$

where ϕ is the flow rate of Ar in sccm (using 101.325 kPa and 273.15 K as standard pressure and temperature, respectively), v_g is the mean drift velocity of Ar and A_c is the cross-section area. After substitution we obtain:

$$v_g = \frac{4F_{in} k_B T}{p \pi D^2}, \tag{A3}$$

where D is the chamber diameter. After combining the constants, we can calculate the drift velocity in cm/s as:

$$v_g = 7.87 \frac{T}{D^2} \frac{\phi}{p}, \tag{A4}$$

where T is in K, D is in cm and p is in Pa.

A.2. Diffusion coefficient

The Chapman-Enskog first approximation for a hard-sphere model gives the diffusion coefficient of metal atoms in a gas as (see Eq. (3.69) in [38]):

$$D_m = \frac{3}{16} \left(\frac{2\pi k_B T}{m_{red}} \right)^{1/2} \frac{1}{n_g \sigma_T}, \tag{A5}$$

where $m_{red} = m_g m_m / (m_g + m_m)$ is the reduced mass (m_g and m_m are the masses of gas and metal atoms, respectively) and $\sigma_T = \pi(r_g + r_m)^2$ is the collision cross-section in terms of the hard-sphere model (r_g and r_m are the radii of gas and metal atoms, respectively). After substitution, we obtain:

$$D_m = \frac{3}{16(r_g + r_m)^2} \left(\frac{2k_B^3}{\pi m_{red}} \right)^{1/2} \frac{T^{3/2}}{p}. \tag{A6}$$

Using 0.21 and 0.23 nm for Ar [38] and Cu atom radii, respectively, we can evaluate the diffusion coefficient as:

$$D_m = \frac{2T^{3/2}}{p}. \tag{A7}$$

A.3. Balance of incoming and outgoing Ar gas flow rate

We estimate the flow rate through the exit orifice of diameter d as:

$$F_{out} = \frac{1}{4}n_g v_{g,th} A_o = \frac{1}{4}\frac{p}{k_B T}\sqrt{\frac{8k_B T}{\pi m_g}}\frac{1}{4}\pi d^2 = \frac{pd^2}{4}\sqrt{\frac{\pi}{2m_g k_B T}}, \tag{A8}$$

where $v_{g,th}$ is the mean (thermal) velocity of Ar and A_o is the orifice area. After setting this equal to F_{in}, we have:

$$\frac{p}{\phi} = \frac{4 \times 4.48 \times 10^{17}}{d^2}\sqrt{\frac{2m_g k_B T}{\pi}}. \tag{A9}$$

We can evaluate the p to ϕ ratio in Pa/sccm as:

$$\frac{p}{\phi} = 1.37\frac{\sqrt{T}}{d^2} \tag{A10}$$

where T is in K and d is in mm.

References

[1] I. Khan, K. Saeed, I. Khan, Nanoparticles: properties, applications and toxicities, Arab. J. Chem. 12 (2019) 908–931, https://doi.org/10.1016/j.arabjc.2017.05.011.
[2] A.P. Nikalje, Nanotechnology and its applications in medicine, Med. Chem. (Los. Angeles) 5 (2015) 81–89, https://doi.org/10.4172/2161-0444.1000247.
[3] K. Ranganathan, A. Morais, I. Nongwe, C. Longo, A.F. Nogueira, N.J. Coville, Study of photoelectrochemical water splitting using composite films based on TiO_2 nanoparticles and nitrogen or boron doped hollow carbon spheres as photoanodes, J. Mol. Catal. A Chem. 422 (2016) 165–174, https://doi.org/10.1016/j.molcata.2015.10.024.
[4] S. Haviar, J. Čapek, Š. Batková, N. Kumar, F. Dvořák, T. Duchoň, M. Fialová, P. Zeman, Hydrogen gas sensing properties of WO_3 sputter-deposited thin films enhanced by on-top deposited CuO nanoclusters, Int. J. Hydrog. Energy 43 (2018) 22756–22764, https://doi.org/10.1016/j.ijhydene.2018.10.127.
[5] A. Kosmala, R. Wright, Q. Zhang, P. Kirby, Synthesis of silver nano particles and fabrication of aqueous Ag inks for inkjet printing, Mater. Chem. Phys. 129 (2011) 1075–1080, https://doi.org/10.1016/j.matchemphys.2011.05.064.
[6] A.V. Rane, K. Kanny, V.K. Abitha, S. Thomas, Methods for synthesis of nanoparticles and fabrication of nanocomposites, in: Synth. Inorg. Nanomater, Elsevier, 2018, pp. 121–139, https://doi.org/10.1016/b978-0-08-101975-7.00005-1.
[7] H. Haberland, Filling of micron-sized contact holes with copper by energetic cluster impact, J. Vac. Sci. Technol. A 12 (1994) 2925, https://doi.org/10.1116/1.578967.
[8] P.V. Kashtanov, B.M. Smirnov, R. Hippler, Magnetron plasma and nanotechnology, Physics-Uspekhi. 50 (2007) 455–488, https://doi.org/10.1070/PU2007v050n05ABEH006138.
[9] Y. Huttel, L. Martínez, A. Mayoral, I. Fernández, Gas-phase synthesis of nanoparticles: present status and perspectives, MRS Commun. 8 (2018) 947–954, https://doi.org/10.1557/mrc.2018.169.
[10] V.N. Popok, O. Kylián, Gas-phase synthesis of functional Nanomaterials, Appl, Nano. 1 (2020) 25–58, https://doi.org/10.3390/applnano1010004.
[11] S. Ekeroth, S. Ikeda, R.D. Boyd, T. Shimizu, U. Helmersson, Growth of semi-coherent Ni and NiO dual-phase nanoparticles using hollow cathode sputtering, J. Nanopart. Res. 21 (2019) 1–8, https://doi.org/10.1007/s11051-019-4479-4.
[12] M. Melzer, J. Urban, H. Sack-Kongehl, K. Weiss, H.J. Freund, R. Schlögl, Preparation of vanadium and vanadium oxide clusters by means of inert gas aggregation, Catal. Lett. 81 (2002) 219–221, https://doi.org/10.1023/A:1016585208341.
[13] S. Xiong, W. Qi, B. Huang, M. Wang, Size-, shape- and composition-dependent alloying ability of bimetallic nanoparticles, ChemPhysChem. 12 (2011) 1317–1324, https://doi.org/10.1002/cphc.201100001.
[14] D. Guo, G. Xie, J. Luo, Mechanical properties of nanoparticles: basics and applications, J. Phys. D. Appl. Phys. 47 (2014), 013001, https://doi.org/10.1088/0022-3727/47/1/013001.
[15] D. Nikitin, J. Hanuš, S. Ali-Ogly, O. Polonskyi, J. Drewes, F. Faupel, H. Biederman, A. Choukourov, The evolution of Ag nanoparticles inside a gas aggregation cluster source, Plasma Process. Polym. 16 (2019) 1–7, https://doi.org/10.1002/ppap.201900079.
[16] A. Shelemin, P. Pleskunov, J. Kousal, J. Drewes, J. Hanuš, S. Ali-Ogly, D. Nikitin, P. Solař, J. Kratochvíl, M. Vaidulych, M. Schwartzkopf, O. Kylián, O. Polonskyi, T. Strunskus, F. Faupel, S.V. Roth, H. Biederman, A. Choukourov, Nucleation and growth of magnetron-sputtered Ag nanoparticles as witnessed by time-resolved small angle X-ray scattering, Part. Part. Syst. Charact. 37 (2020) 1–11, https://doi.org/10.1002/ppsc.201900436.
[17] B. Briehl, H.M. Urbassek, Monte Carlo simulation of growth and decay processes in a cluster aggregation source, J. Vac. Sci. Technol. A 17 (1999) 256–265, https://doi.org/10.1116/1.581580.
[18] B.M. Smirnov, Processes involving clusters and small particles in a buffer gas, Usp. Fiziol. Nauk 181 (2011) 713, https://doi.org/10.3367/UFNr.0181.201107b.0713.
[19] A.A. Turkin, M.V. Dutka, Y.T. Pei, D.I. Vainshtein, J.T.M. De Hosson, On the evolution of nanocluster size distribution in a nanocluster aggregation source, J. Appl. Phys. 111 (2012), 124326, https://doi.org/10.1063/1.4731221.
[20] O. Polonskyi, A.M. Ahadi, T. Peter, K. Fujioka, J.W. Abraham, E. Vasiliauskaite, A. Hinz, T. Strunskus, S. Wolf, M. Bonitz, H. Kersten, F. Faupel, Plasma based formation and deposition of metal and metal oxide nanoparticles using a gas aggregation source, Eur. Phys. J. D 72 (2018) 93, https://doi.org/10.1140/epjd/e2017-80419-8.
[21] J. Kousal, O. Polonskyi, O. Kylián, A. Choukourov, A. Artemenko, J. Pešička, D. Slavínská, H. Biederman, Characterization of nanoparticle flow produced by gas aggregation source, Vacuum. 96 (2013) 32–38, https://doi.org/10.1016/j.vacuum.2013.02.015.
[22] S. Pratontep, S.J. Carroll, C. Xirouchaki, M. Streun, R.E. Palmer, Size-selected cluster beam source based on radio frequency magnetron plasma sputtering and gas condensation, Rev. Sci. Instrum. 76 (2005), 045103, https://doi.org/10.1063/1.1869332.
[23] P. Solař, O. Polonskyi, A. Choukourov, A. Artemenko, J. Hanuš, H. Biederman, D. Slavínská, Nanostructured thin films prepared from cluster beams, Surf. Coat. Technol. 205 (2011) 42–47, https://doi.org/10.1016/j.surfcoat.2011.01.059.
[24] A.I. Ayesh, H.A. Ahmed, F. Awwad, S.I. Abu-Eishah, S.T. Mahmood, Mechanisms of Ti nanocluster formation by inert gas condensation, J. Mater. Res. 28 (2013) 2622–2628, https://doi.org/10.1557/jmr.2013.246.
[25] R. Gunnarsson, I. Pilch, R.D. Boyd, N. Brenning, U. Helmersson, The influence of pressure and gas flow on size and morphology of titanium oxide nanoparticles synthesized by hollow cathode sputtering, J. Appl. Phys. 120 (2016), 044308, https://doi.org/10.1063/1.4959993.
[26] A. Vahl, J. Strobel, W. Reichstein, O. Polonskyi, T. Strunskus, L. Kienle, F. Faupel, Single target sputter deposition of alloy nanoparticles with adjustable composition via a gas aggregation cluster source, Nanotechnology. 28 (2017), 175703, https://doi.org/10.1088/1361-6528/aa66ef.
[27] M. Khojasteh, V.V. Kresin, Influence of source parameters on the growth of metal nanoparticles by sputter-gas-aggregation, Appl. Nanosci. 7 (2017) 875–883, https://doi.org/10.1007/s13204-017-0627-2.
[28] C. Liu, L. Zhang, S. Zhang, F. Liu, G. Wang, M. Han, Influence of discharge power on the size of the Pd cluster generated with a magnetron plasma gas aggregation cluster source, Vacuum. 179 (2020), 109486, https://doi.org/10.1016/j.vacuum.2020.109486.
[29] V. Straňák, S. Block, S. Drache, Z. Hubička, C.A. Helm, L. Jastrabík, M. Tichý, R. Hippler, Size-controlled formation of Cu nanoclusters in pulsed magnetron sputtering system, Surf. Coat. Technol. 205 (2011) 2755–2762, https://doi.org/10.1016/j.surfcoat.2010.10.030.
[30] R. Gunnarsson, Controlling the Growth of Nanoparticles Produced in a High Power Pulsed Plasma, Doctoral dissertation, Linköping University, 2017.

[31] M. Ganeva, A.V. Pipa, R. Hippler, The influence of target erosion on the mass spectra of clusters formed in the planar DC magnetron sputtering source, Surf. Coat. Technol. 213 (2012) 41–47, https://doi.org/10.1016/j.surfcoat.2012.10.012.

[32] T. Peter, O. Polonskyi, B. Gojdka, A. Mohammad Ahadi, T. Strunskus, V. Zaporojtchenko, H. Biederman, F. Faupel, Influence of reactive gas admixture on transition metal cluster nucleation in a gas aggregation cluster source, J. Appl. Phys. 112 (2012) 1–7, https://doi.org/10.1063/1.4768528.

[33] J. Polášek, K. Mašek, A. Marek, J. Vyskočil, Effects of oxygen addition in reactive cluster beam deposition of tungsten by magnetron sputtering with gas aggregation, Thin Solid Films 591 (2015) 194–199, https://doi.org/10.1016/j.tsf.2015.03.044.

[34] A. Shelemin, O. Kylián, J. Hanuš, A. Choukourov, I. Melnichuk, A. Serov, D. Slavínská, H. Biederman, Preparation of metal oxide nanoparticles by gas aggregation cluster source, Vacuum. 120 (2015) 162–169, https://doi.org/10.1016/j.vacuum.2015.07.008.

[35] S. Drache, V. Stranak, Z. Hubicka, F. Berg, M. Tichy, C.A. Helm, R. Hippler, Study of mass and cluster flux in a pulsed gas system with enhanced nanoparticle aggregation, J. Appl. Phys. 116 (2014), https://doi.org/10.1063/1.4897234.

[36] M. Vaidulych, J. Hanuš, J. Kousal, S. Kadlec, A. Marek, I. Khalakhan, A. Shelemin, P. Solař, A. Choukourov, O. Kylián, H. Biederman, Effect of magnetic field on the formation of Cu nanoparticles during magnetron sputtering in the gas aggregation cluster source, Plasma Process. Polym. 16 (2019) 1–10, https://doi.org/10.1002/ppap.201900133.

[37] K. Fujioka, Kinetic Monte Carlo Simulations of Cluster Growth in Magnetron Plasmas, Doctoral dissertation, Christian-Albrechts-Universität zu Kiel, 2015.

[38] G.A. Bird, Molecular Gas Dynamics and the Direct Simulation of Gas Flows, Clarendon Press, 1994.

IV Conclusions

This Ph.D. thesis reports on preparation and systematic investigation of Ta–O–N films with very finely-tuned elemental composition. Films with properties suitable for the light-induced water splitting application were looked for. Because it should be possible to even further enhance the water splitting performance in future research by tuning of the material structure and by addition of nanoparticles, advanced magnetron-based deposition techniques were also investigated: (a) bipolar HiPIMS and its effects on the structure and properties of the prepared films and (b) magnetron-based gas-aggregation source of nanoparticles and the possibility of nanoparticle size control.

The main results of the investigation can be summarized as follows:

1. Ta–O–N films were prepared by high power impulse magnetron sputtering (HiPIMS) with a finely controlled elemental composition in a wide range (from $Ta_{27}O_{73}N_0$ to $Ta_{44}O_7N_{50}$) by controlling a single deposition parameter of nitrogen fraction in the reactive gas flow rate, f_{N2}. The properties (refractive index, extinction coefficient, optical band gap width and electrical resistivity) of the as-deposited films also changed as functions of f_{N2}. However, all the as-deposited films exhibited amorphous structure, which is undesirable for the water-splitting application. When investigating the effect of annealing at 900°C in vacuum, it was found that the annealing process did not affect the elemental composition of the films, but led to their crystallization. The structure of the films gradually changed from an orthorhombic Ta_2O_5 phase via a monoclinic TaON phase to a cubic TaN phase as a function of f_{N2}. The important result is the demonstration that the used approach (HiPIMS deposition of Ta–O–N films in combination with the annealing of the films) can be utilized for a preparation of a crystalline Ta–O–N film exhibiting a single TaON phase with a monoclinic structure. This film exhibits a band gap of 2.45 eV (suitable for visible-light absorption up to 505 nm), low electrical resistivity of 0.4 Ω cm (indicating enhanced charge transport in the material as compared to the as-deposited counterpart) and appropriate position of the band gap with respect to the water splitting redox potentials.

2. After further fine-tuning of the elemental composition of the N-rich Ta–O–N films and post-annealing them, it was found that a deposition at an optimum gas mixture composition led to preparation of a Ta_2N_2O film exhibiting a dominant bixbyite structure. As far as we know, this phase has been neither experimentally nor theoretically reported yet. The film was

semitransparent with an optical band gap width of 2.0 eV as measured by spectroscopic ellipsometry. Measurements of the electrical conductivity as a function of temperature further showed a semiconducting dependence characterized by two electrical band gaps of about 0.2 and 1.0 eV. The carried out *ab initio* calculations indicated that these two band gaps are associated with a negligible probability of excitations due to a photon absorption. We also discussed the potential of this material for water splitting. Its optical band gap of 2.0 eV is suitable for utilization of a large fraction of the visible light (up to 620 nm) for generation of electron–hole pairs required for the process. Furthermore, the band gap position is quite unique with respect to the water splitting redox potentials. In addition, the possible effect of thermally excited charge carriers (due to the narrow electrical band gaps) on the recombination of the photogenerated charge carriers was thoroughly discussed.

3. The possibility of using bipolar HiPIMS to control the crystal structure, microstructure and resulting mechanical properties of CrN films was investigated. Special attention was paid to the potential at which the substrate holder was held during the deposition. A comparison was made between bipolar HiPIMS and unipolar HiPIMS with a DC bias voltage applied to the substrate holder. Using a substrate holder at a floating potential, we have shown that bipolar HiPIMS cannot be used instead of a DC substrate bias voltage for a deposition of non-conductive films or onto non-conductive substrates when the plasma-substrate potential difference necessary for ion acceleration is lost already at the beginning of the positive pulse due to rapid charging of the non-conductive material. Changes in the positive pulse voltage then do not lead to any significant changes in the crystal structure, microstructure and mechanical properties. However, when the substrate holder is grounded, an evolution is apparent with increasing positive pulse voltage, even on non-conductive substrates if the growing film is conductively connected with the ground. After comparing the effect of a positive pulse voltage to the effect of a DC bias voltage applied to the substrate holder, it was found that the effects are different and that the most interesting properties (high hardness at a relatively low residual stress) are achieved for the films prepared using bipolar HiPIMS with a grounded substrate holder at positive pulse voltages of 90 and 120 V. Additional advantages over a DC substrate bias voltage are a stable discharge and a negligible deposition rate reduction. Bipolar HiPIMS can therefore be expected to gain in popularity, presuming that the growing film is conductive and can thus be grounded.

4. The effect of an exit-orifice diameter of a gas-aggregation source on the size of the prepared nanoparticles, the mass flux of the nanoparticles and its angular distribution was investigated. By changing the orifice diameter, we were able to independently control the flow rate of the argon working gas at a constant Ar pressure and investigate its effect. We have shown that the conventional approach of increasing the working-gas pressure by increasing its flow rate does not significantly influence the nanoparticle size. However, when the pressure is kept constant and the flow rate changes due to the utilization of various orifice diameters, the nanoparticle size increases significantly with decreasing orifice diameter. Furthermore, the mass flux increases and the nanoparticle beam becomes narrower with increasing orifice diameter. The results suggest that the important parameter to consider is the pressure to flow rate ratio, which is constant for a constant orifice diameter, but changes together with the orifice diameter. This ratio determines the drift velocity and the residence time of the nanoparticles inside the aggregation chamber. These two parameters in turn affect the size, the mass flux and its angular distribution.

V Further publications of the candidate

1. Papers in impacted international journals

[1] S. Haviar, J. Čapek, Š. Batková, N. Kumar, F. Dvořák, T. Duchoň, M. Fialová, P. Zeman
"Hydrogen gas sensing properties of WO_3 sputter-deposited thin films enhanced by on-top deposited CuO nanoclusters"
Int. J. Hydrog. Energy 43 (2018) 22756–22764.

2. Oral and poster contributions at international conferences

[1] J. Čapek, Š. Batková, J. Houška
"*HiPIMS deposition of Ta–O–N coatings with modified surface by Cu nanoclusters for water splitting*", 4th International Workshop and the 3rd International Mini Workshop on Solution Plasma and Molecular Technology, 7. – 11. 6. 2016, Plzeň, Czech Republic (co-author of oral presentation).

[2] J. Čapek, Š. Batková, J. Houška
"*HiPIMS deposition of Ta–O–N coatings with modified surface by Cu nanoclusters for water splitting application*", 15th International Conference on Plasma Surface Engineering (PSE 2016), 12 – 16. 9. 2016, Garmisch-Partenkirchen, Germany (co-author of poster presentation).

[3] J. Čapek, Š. Batková, J. Houška, S. Haviar, T. Duchoň
"*HiPIMS deposition of Ta–O–N coatings with modified surface by Cu nanoclusters for water splitting application*", 15th International Conference on Reactive Sputter Deposition 2016 (RSD 2016), 1. – 2. 12. 2016, Ghent, Belgium (co-author of the oral presentation).

[4] J. Čapek, Š. Batková, S. Haviar, J. Houška
"*HiPIMS Deposition of Ta–O–N Coatings with Modified Surface by Cu Nanoclusters for Water Splitting Application*", 44th International Conference on Metallurgical Coatings and Thin Films (ICMCTF 2017), 24. – 28. 4. 2017, San Diego, USA (co-author of the oral presentation).

[5] J. Čapek, Š. Batková, S. Haviar, J. Houška, T. Duchoň,
"*HiPIMS deposition of Ta–O–N coatings for water splitting application*", E-MRS 2017 Spring Meeting, 22. – 26. 5. 2017, Strasbourg, France (co-author of the oral presentation).

[6] S. Haviar, M. Fialová, Š. Batková, F. Dvořák
"*Sputter-deposited Nanostructured Metal-Oxide Films for Hydrogen Gas Sensing*", 7th Internationl Symposium on Energy (Energy7), 13. – 17. 8. 2017, Manchester, UK (co-author of the poster presentation).

[7] S. Haviar, M. Fialová, Š. Batková, J. Čapek, R. Čerstvý, T. Duchoň "*Sputter-deposited Nanostructured Metal-Oxide Films for Hydrogen Gas Sensing*", European Congress and Exhibition on Advanced Materials and Processes (EUROMAT 2017), 17. - 22. 9. 2017, Thessaloniki, Greece (co-author of the oral presentation).

[8] Š. Batková, J. Čapek, J. Houška, S. Haviar, R. Čerstvý, T. Duchoň "*Post-annealing of Ta–O–N films prepared by reactive HiPIMS: A step towards effective water splitting*", 16th International Conference on Reactive Sputter Deposition (RSD 2017), 4. – 6. 12. 2017, Plzeň, Czech Republic (author of the poster presentation).

[9] J. Čapek, Š. Batková, J. Houška, S. Haviar, T. Duchoň "*HiPIMS Deposition of Ta–O–N Coatings for Water Splitting Application*", 45th International Conference on Metallurgical Coatings and Thin Films (ICMCTF 2018), 23. – 27. 4. 2018, San Diego, USA (co-author of the oral presentation).

[10] S. Haviar, J. Čapek, N. Kumar, Š. Batková, M. Fialová, R. Čerstvý, T. Duchoň, F. Dvořák "S*putter-deposited Nanostructured Metal-Oxide Films for Hydrogen Gas Sensing*", 45th International Conference on Metallurgical Coatings and Thin Films (ICMCTF 2018), 23. – 27. 4. 2018, San Diego, USA (co-author of the poster presentation).

[11] J. Čapek, Š. Batková, J. Houška, R. Čerstvý, S. Haviar, T. Duchoň "*HiPIMS Deposition of Ta–O–N Coatings for Water Splitting Application*", 14th International Ceramic Congress (CIMTEC 2018), 04. – 08. 6. 2018, Perugia, Italy (co-author of the oral presentation).

[12] Š. Batková, J. Čapek, J. Houška, S. Haviar, R. Čerstvý, T. Duchoň, M. Krbal "*Structure optimization of Ta–O–N films prepared by reactive HiPIMS for more effective water splitting*"**,** 17th Joint Vacuum Conference (JVC 2018), 10. – 14. 9. 2018, Olomouc, Czech Republic (author of the oral presentation).

[13] Š. Batková, J. Čapek, S. Haviar, J. Houška, R. Čerstvý, M. Krbal "*Structure optimization of Ta–O–N films prepared by reactive HiPIMS for more effective water splitting*", 16th International Conference on Plasma Surface Engineering (PSE 2018), 17. – 21. 9. 2018, Garmisch-Partenkirchen, Germany (author of the poster presentation).

[14] N. Kumar, S. Haviar, J. Čapek, Š. Batková "N*anostructured Metal-Oxide Based Hydrogen Gas Sensor Prepared by Magnetron Sputtering*", 16th International Conference on Plasma Surface Engineering (PSE 2018), 17. – 21. 9. 2018, Garmisch-Partenkirchen, Germany (co-author of the poster presentation).

[15] S. Haviar, N. Kumar, J. Čapek, Š. Batková, F. Dvořák, M. Fialová "*Nanocluster-Based Metal Oxide Films for Hydrogen Gas Sensing*", 16th International Conference on Plasma Surface Engineering (PSE 2018), 17. – 21. 9. 2018, Garmisch-Partenkirchen, Germany (co-author of the oral presentation).

[16] J. Čapek, Š. Batková, J. Houška, S. Haviar, T. Duchoň, M. Krbal "*HiPIMS deposition of Ta–O–N coatings with modified surface by metallic nanoclusters for water splitting application*", 85th IUVSTA WORKSHOP - Nanoporous materials for green energy conversion and storage, 14. – 19. 10. 2018, Schloss Seggau, Austria (co-author of the oral presentation).

[17] S. Haviar, J. Čapek, N. Kumar, Š. Batková, F. Dvořák "*Nanocluster-based Hydrogen Gas Sensors (CuO/WO_3) Prepared by Advanced Magnetron Sputtering Techniques*", 85th IUVSTA WORKSHOP - Nanoporous materials for green energy conversion and storage, 14. – 19. 10. 2018, Schloss Seggau, Austria (co-author of the oral presentation).

[18] S. Haviar, J. Čapek, Š. Batková, N. Kumar "*Nanocluster-Based Metal Oxide Films for Hydrogen Gas Sensing*", 46th International Conference on Metallurgical Coatings and Thin Films (ICMCTF 2019), 19. – 24. 5. 2019, San Diego, USA (co-author of the oral presentation).

[19] Š. Batková, J. Čapek, S. Haviar, J. Houška, R. Čerstvý, M. Krbal, T. Duchoň "*Structure optimization of Ta–O–N films prepared by reactive HiPIMS for more effective water splitting*", 46th International Conference on Metallurgical Coatings and Thin Films (ICMCTF 2019), 19. – 24. 5. 2019, San Diego, USA (author of the oral presentation).

[20] J. Čapek, Š. Batková, J. Houška, S. Haviar, T. Duchoň, M. Krbal "*HiPIMS Deposition of Ta–O–N Coatings for Water Splitting Aplication*", 37th Spring Meeting of the European Materials Research Society 2019 (E-MRS 2019), 27. – 31. 5. 2019, Nice, France (co-author of the oral presentation).

[21] N. Kumar, S. Haviar, Š. Batková, J. Čapek, P. Baroch "*Hydrogen Gas Sensor Based on WO_3 and CuO thin films and Nanoclusters*", 37th Spring Meeting of the European Materials Research Society 2019 (E-MRS 2019), 27. – 31. 5. 2019, Nice, France (co-author of the poster presentation).

[22] Š. Batková, J. Čapek, S. Haviar, J. Houška, R. Čerstvý, M. Krbal, T. Duchoň "*Photocatalytic Ta–O–N films prepared by reactive HiPIMS*", 10th International Conference on Fundamentals and Industrial Applications of HIPIMS 2019 & International Conference on Sputter Technology (HiPIMS-ST 2019), 19. – 20. 6. 2019, Braunschweig, Germany (author of the poster presentation).

[23] J. Čapek, Š. Batková, J. Houška, S. Haviar, T. Duchoň, M. Krbal
"*HiPIMS Deposition of Ta–O–N Coatings for Water Splitting Aplication*", 6th International Conference from Nanoparticles and Nanomaterials to Nanodevices and Nanosystems (IC4N 2019), 30. 6. – 3. 7. 2019, Corfu, Greece (co-author of the oral presentation).

[24] S. Haviar, Š. Batková, N. Kumar, J. Čapek
"*Nanocluster-Based Metal Oxide Films for Hydrogen Gas Sensing Prepared by Advanced Magnetron Sputtering Techniques*", 21st International Vacuum Congress 2019 (IVC 2019), 1. – 5. 7. 2019, Malmö, Sweden (co-author of the oral presentation).

[25] Š. Batková, J. Čapek, S. Haviar, J. Houška, R. Čerstvý, M. Krbal, T. Duchoň
"*Photocatalytic Ta–O–N films prepared by reactive HiPIMS*", European Congress and Exhibition on Advanced Materials and Processes 2019 (EUROMAT 2019), 1. – 5. 9. 2019, Stockholm, Sweden (author of the oral presentation).

[26] J. Čapek, Š. Batková, S. Haviar, M. Matas, J. Houška, J. Schusser, J. Minár, F. Dvořák
"*Structure and properties of bixbyite-based Ta–O–N films prepared by HiPIMS*", PSE Satellite – Workshop on Plasma-Based Synthesis of Nanomaterials, 10. – 11. 02. 2020, Prague, Czech Republic (co-author of the oral presentation).

[27] S. Haviar, J. Čapek, N. Kumar, Š. Batková
"*Nanostructured Materials Based on Thin Films and Nanoclusters for Hydrogen Gas Sensing*", 4th International conference Functional Integrated Nano Systems (Nanofis), 2. – 4. 11. 2020, on-line (co-author of the oral presentation).

[28] Š. Batková, J. Čapek, J. Rezek, R. Čerstvý, P. Zeman
"*Effect of positive pulse voltage in bipolar reactive HiPIMS on crystal structure, microstructure and mechanical properties of CrN films*", 18th International Conference on Thin Films and 18th Joint Vacuum Conference (ICTF-JVC 2020), 22. – 26. 11. 2020, on-line (author of the oral presentation).

[29] S. Haviar, J. Čapek, N. Kumar, Š. Batková
"*Nanostructured Materials Based on Thin Films and Nanoclusters for Hydrogen Gas Sensing*", 18th International Conference on Thin Films and 18th Joint Vacuum Conference (ICTF-JVC 2020), 22. – 26. 11. 2020, on-line (co-author of the oral presentation).

[30] Š. Batková, J. Čapek, T. Kozák, S. Haviar, P. Mareš
"*Effect of exit-orifice size on Cu nanoparticles produced by gas-aggregation source*", 5th German-Czech Workshop on Nanomaterials, 25. – 26. 1. 2021, on-line (author of the oral presentation).

[31] Š. Batková, J. Čapek, T. Kozák, S. Haviar, P. Mareš
"*Effect of exit-orifice size on Cu nanoparticles produced by gas-aggregation source*", Plasma Thin Film International Union Meeting (PLATHINIUM 2021), 13. – 17. 9. 2021, on-line (author of the oral presentation).